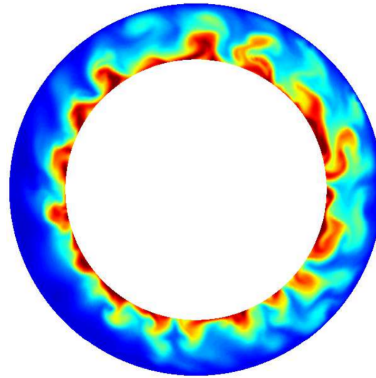




TÉCNICO
LISBOA



Simulation of Plasma Blobs in Realistic Tokamak Geometry

Rogério Manuel Cabete de Jesus Jorge

Thesis to obtain the Master of Science Degree in

Engineering Physics

Supervisors: Prof. Nuno Filipe Gomes Loureiro
Prof. Paolo Ricci

Examination Committee

Chairperson:	Prof. Luís Paulo da Mota Capitão Lemos Alves
Supervisor:	Prof. Nuno Filipe Gomes Loureiro
Member of the Committee:	Doctor Federico David Halpern
Member of the Committee:	Prof. Carlos Alberto Nogueira Garcia Silva

October 2014

Acknowledgments

This thesis embraces a collaboration between two groups at IPFN (“Instituto de Plasmas e Fusão Nuclear”), IST, Lisbon, namely the Theory and Modeling Group and the Experimental Physics Group, with the theory group at CRPP (“Centre de Recherche en Physique de Plasmas”), EPFL, Lausanne.

At IPFN, I would like to thank my supervisor Prof. Nuno Loureiro for the support since the beginning of the project and the choice of the extremely interesting topic and Dr. Carlos Silva, for supporting the project from the experimental point of view and providing valuable insight.

At CRPP I found a new and outstanding way to study and do physics. It was a lifetime opportunity to be able to work in a fulfilling environment and with such amazing people. For this and much more, I thank my co-supervisor Prof. Paolo Ricci and Doctor Frederico Halpern.

Finally I would not be able to do this work without the help of my friends and family, specially my mother and father, to whom I can not be grateful enough.

Resumo

A compreensão detalhada da turbulência na SOL (*Scrape-off Layer*) é crucial para o sucesso da fusão por confinamento magnético como um todo. Ela determina o confinamento global e a eficiência de tokamaks futuros (tal como o ITER), governando a acumulação de calor na parede sólida do dispositivo, regulando a dinâmica de impurezas e a reinserção de plasma. Aqui, o valor comum da frequência de colisão é alto e as flutuações ocorrem em escalas maiores que o raio de Larmor iônico. Isto implica que a dinâmica na SOL pode ser analisada através da descrição "drift reduced" de Braginskii. O código GBS integra numericamente estas equações, permitindo modelizar a evolução da dinâmica do plasma na SOL em 3D, não separando as perturbações do equilíbrio, e investigando de maneira auto-consistente a formação dos perfis resultantes do fluxo de plasma e calor do núcleo para a SOL e do transporte oblíquo às linhas de campo proveniente da turbulência gerada por diversas instabilidades. Neste trabalho, o código GBS foi modificado para a configuração da SOL do tokamak ISTTOK, comprovando o carácter "ballooning" da turbulência, onde o comprimento típico dos gradientes aumenta na região de má curvatura, e determinando o mecanismo de saturação não-linear através da hipótese "gradient removal". Utilizando um código linear, foi determinada a influência da torsão magnética, resistividade, fator de segurança e efeitos eletromagnéticos na taxa de crescimento linear das instabilidades presentes na SOL do ISTTOK. Uma estimativa para o comprimento característico do gradiente de pressão é obtida para os resultados experimentais.

Palavras-chave: física de plasmas, fusão por confinamento magnético, scrape-off layer, turbulência de plasma, ISTTOK, transporte turbulento

Abstract

Understanding *Scrape-off Layer* (SOL) turbulence is crucial for the success of the entire magnetic confinement fusion program. It determines the overall confinement and performance of future tokamaks (such as ITER), governs the heat load on the vessel wall, and regulates the impurity dynamics and plasma refueling. In the SOL, the collision frequency is large and the fluctuations occur on scales larger than the ion Larmor radius. This implies that plasma dynamics in the SOL can be investigated with the drift-reduced Braginskii equations. The GBS code numerically integrates these equations, allowing us to model the evolution of the SOL plasma dynamics in 3D, without separation between perturbations and equilibrium, modeling therefore the self-consistent formation of the plasma profiles resulting from the plasma and heat outflowing from the core to the SOL, the cross-field transport arising from turbulence driven by a number of instabilities and parallel losses at the sheaths. In this work the GBS code has been ported to ISTTOK's SOL configuration, asserting the ballooning character of turbulence in the SOL, where the typical gradient length increases at the bad curvature region, and determining the non-linear saturation mechanism through the gradient removal hypothesis. Through a linear code, we determined the influence of the magnetic shear, safety factor, resistivity and electromagnetic effects in the linear growth rate of the instabilities at play in ISTTOK's SOL. An estimate for the typical pressure gradient length is obtained for the experimental results.

Keywords: plasma physics, magnetic confinement fusion, scrape-off layer, plasma turbulence, ISTTOK, turbulent transport

Contents

Acknowledgments	iii
Resumo	v
Abstract	vii
List of Tables	xi
List of Figures	xv
List of Acronyms	xvii
1 Introduction	1
1.1 Quest for Energy	1
1.2 Why Fusion	2
1.3 The Dynamics of Magnetically Confined Plasmas	3
1.4 The Scrape-Off Layer, Scrape-off Layer (SOL)	6
1.5 ISTTOK Geometry and the Global Braginskii Solver (GBS) code	8
1.5.1 ISTTOK	8
1.5.2 GBS Code	9
1.6 Scope and Outline of the Thesis	10
2 Description of the Model and the GBS code	13
2.1 Braginskii Equations	13
2.2 Drift Reduced Model	16
2.3 Vorticity and Continuity equations	17
2.4 Semi-Electrostatic Limit	18
2.5 Parallel Motion	19
2.6 Temperature Equations	19
2.7 GBS Model	20
2.8 ISTTOK Geometry	22
2.9 Numerical Implementation	23
2.10 Boundary and Initial Conditions	24

3	Analysis of Turbulence Regimes in ISTTOK's SOL	27
3.1	Linearized System and Linear Solver	27
3.2	Linear SOL Instabilities	30
3.2.1	Drift Waves	30
3.2.2	Ballooning Modes	31
3.3	Linear Instability Analysis	33
3.4	Gradient Removal Mechanism	35
3.5	Non-Linear Analysis Techniques	37
3.5.1	L_p Variation	37
3.5.2	Cross-Coherence	38
3.5.3	Phase Shift	38
3.5.4	Power Spectrum	38
4	Simulation Results and Analysis	40
4.1	GBS Snapshots and Analysis	40
4.2	Typical Pressure Gradient Length	43
4.3	Non-linear Analysis	47
4.4	Comparison Against Experimental Results	48
5	Conclusions	53
	Bibliography	59
A	Derivation of the Braginskii equations	61
B	Muller's Method Algorithm	64

List of Tables

1.1	Geometrical parameters of ISTTOK around the limiter [1].	8
2.1	Code input parameters for ISTTOK in GBS units [1].	23
4.1	Experimental results for L_n , L_T , η and L_p for ISTTOK from Fig. 4.15 in GBS units (1 GBS unit = 0.91 mm in SI units).	51

List of Figures

1.1	Energy consumption in the U.S. by source as a function of time [2].	1
1.2	Proved oil reserves versus production [2].	2
1.3	Schematic representation of a tokamak and the corresponding magnetic field lines (figure taken from [3]). The plasma is depicted in blue; the red annuli are the toroidal field coils.	4
1.4	Diferent examples of poloidal and toroidal limiters [4].	7
1.5	For the limiter configuration, the last closed magnetic flux surface, LCFS, is defined by the leading edge of the limiter. A JET-size plasma is shown (figure taken from [4]).	8
1.6	General view of ISTTOK [5].	9
2.1	Representation of the magnetic field line geometry at ISTTOK with a $q = 8$, where θ is the poloidal angle and ϕ the toroidal one (in radians).	22
2.2	Schematic of the variation of plasma pressure, electric potential, plasma velocity and ion/electron densities in the plasma between two semi-infinite planes (figure taken from [4]).	25
3.1	Rosenbluth-Longmire picture of curvature driven instabilities with an initial perturbation of the density profile at the low-field side of the torus. The curvature drift shifts electrons and ions into opposite directions and the resulting space charge generates an electric field leading to an $\mathbf{E} \times \mathbf{B}$ drift that amplifies the initial perturbation (figure taken from [6]).	32
3.2	Poloidal variation of L_p for the 4 instability branches provided by the gradient removal hypothesis for ISTTOK-like parameters.	33
3.3	Representation of the branch that provides the greatest linear growth rate as a function of the poloidal angle and magnetic shear for the same input parameters inserted in the non-linear simulations.	34
3.4	Each figure shows which branch provides the greatest linear growth rate as a function of the poloidal angle and magnetic shear. With a scan on each variable τ, q, ν and β_e the inertial Drift Waves (DW) and Ballooning Modes (BM) are the major predicted branches at play at ISTTOK's SOL.	35

3.5	Experimental power-spectrum results performed at ISTTOK (figure taken from [1]). The blue line represents the first low-frequency region, the green line the transition region with a slope of -1 and the yellow one the high frequency region with a slope of -2.	39
4.1	Time trace of the electric potential from the beginning of the simulation with cold ions to a quasi-steady state at a fixed location of the High Field Side (HFS) – $(x, y, z) = (20, 1, 16)$, and Low Field Side (LFS) – $(x, y, z) = (20, 256, 16)$. The typical duration of the quasi-steady state phase at ISTTOK varies from 1 to several ms.	41
4.2	Typical snapshot of GBS simulations at a poloidal plane halfway between the limiter. ($z = N_z/2$) Plots show contours of density at a specific time slice - 20 ms (left) and averaged over the steady-state period - between 20 and 22.5 ms (right).	42
4.3	Typical snapshot of GBS simulations at a toroidal plane at $x = 20$ (out of 64 x grid points). Plots show contours of electron (left) and ion (right) parallel velocity averaged over the steady-state period - between 20 and 22.5 ms.	42
4.4	Snapshot of GBS simulations with no DW (left) and no BM (right) coupling at a poloidal plane halfway between the limiter. Plots show contours of density averaged over the steady-state period - between 20 and 22.5 ms.	42
4.5	Fit to the expression (4.1) for the resulting pressure profile toroidally and poloidally averaged. The logarithmic vertical axes allows the visual separation of the characteristic exponential decays right after the source at $x = 15$ and before the wall. The fit results in a $L_p = 1.1$ cm with a SOL width of 4.6 cm. The green crosses indicate values excluded from the fit.	43
4.6	Toroidal variation of L_p from the fit to non-linear simulations. The vertical axes shows L_p in GBS units, where 1 GBS unit = 0.91 mm.	44
4.7	Poloidal variation of L_p from the fit to non-linear simulations (blue) and from the gradient removal hypothesis (red). The vertical axes shows L_p in GBS units, where 1 GBS unit = 0.91 mm.	45
4.8	Poloidally and toroidally averaged density and electron temperature profiles fitted to an exponential behavior. The obtained value of $\eta_e = \frac{L_n}{L_{Te}}$ is $\eta_e = 0.80$	46
4.9	Poloidal variation of η_e from the fit to non-linear simulations.	46
4.10	Cross-coherence test at the HFS and LFS respectively (electric potential vs density). At the top is an ISTTOK-like simulation and at the bottom the BM coupling terms are turned off.	47
4.11	Phase-shift between ϕ and N_e at the HFS and LFS respectively.	48
4.12	Power-spectrum at the HFS and LFS respectively (floating potential V_f and density N_e).	49
4.13	Power-spectrum at the HFS and LFS for no DW and interchange coupling respectively for the electric potential.	49
4.14	$V_{E \times B} / L_p$ as a function of y	50
4.15	I_p scan at ISTTOK with different values of $r - a$ for T_e , V_f and density.	50

4.16 Exponential fit to ISTTOK experimental N_e results. The fit to $I_p = 4.0$ kA provides $L_n = 1.232$ cm with an $R^2 = 0.89$ and the fit to $I_p = 5.5$ kA provides $L_n = 0.971$ cm with an $R^2 = 0.941$	51
4.17 Exponential fit to ISTTOK experimental N_e results. The fit to $I_p = 4.0$ kA provides $L_T = 1.033$ cm with an $R^2 = 0.99$ and the fit to $I_p = 5.5$ kA provides $L_T = 1.168$ cm with an $R^2 = 0.98$	51

List of Acronyms

BM Ballooning Modes

DW Drift Waves

FFT Fast Fourier Transform

FLR Finite Larmor Radius

GBS Global Braginskii Solver

HFS High Field Side

IdBM Ideal Ballooning Mode

InBM Inertial Ballooning Mode

InDW Inertial Drift Wave

IST Instituto Superior Técnico

ITER International Thermonuclear Experimental Reactor

LAR Large Aspect Ratio

LCFS Last Closed (magnetic) Flux Surface

LFS Low Field Side

PSI Plasma-Surface Interaction

RBM Resistive Ballooning Mode

RDW Resistive Drift Wave

SOL Scrape-off Layer

1.1 Quest for Energy

In 2012, fossil fuels in Portugal represented 74.9 % of total energy consumption [7]. In the United States (Fig. 1.1), that number rises to 83.6 %. There are countries like Algeria, United Arab Emirates, Turkmenistan, Saudi Arabia, Qatar, Oman and Kuwait where we see numbers above 95 %. Can this consumption be sustainable?

Over time, oil companies discovered more reserves and new technologies unlocked even more oil resources. Today the world has more *proven oil reserves*¹ than ever before (Fig. 1.2). In the period 1980 to 2007, proven reserves doubled [2]. One of the main reasons that proven reserves have doubled over the last 30 years or so is that oil exploration increased and production technologies improved.

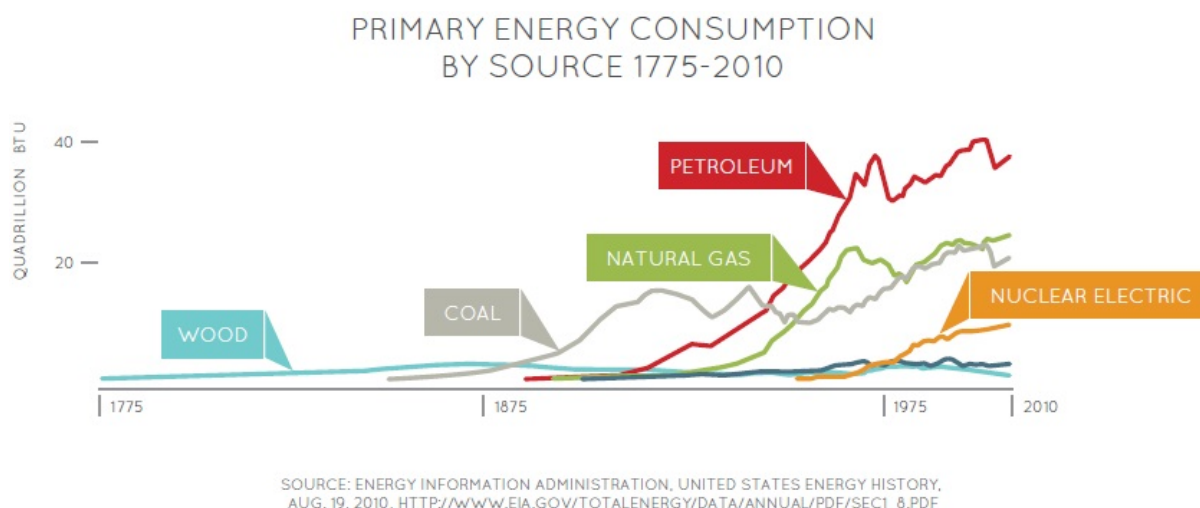
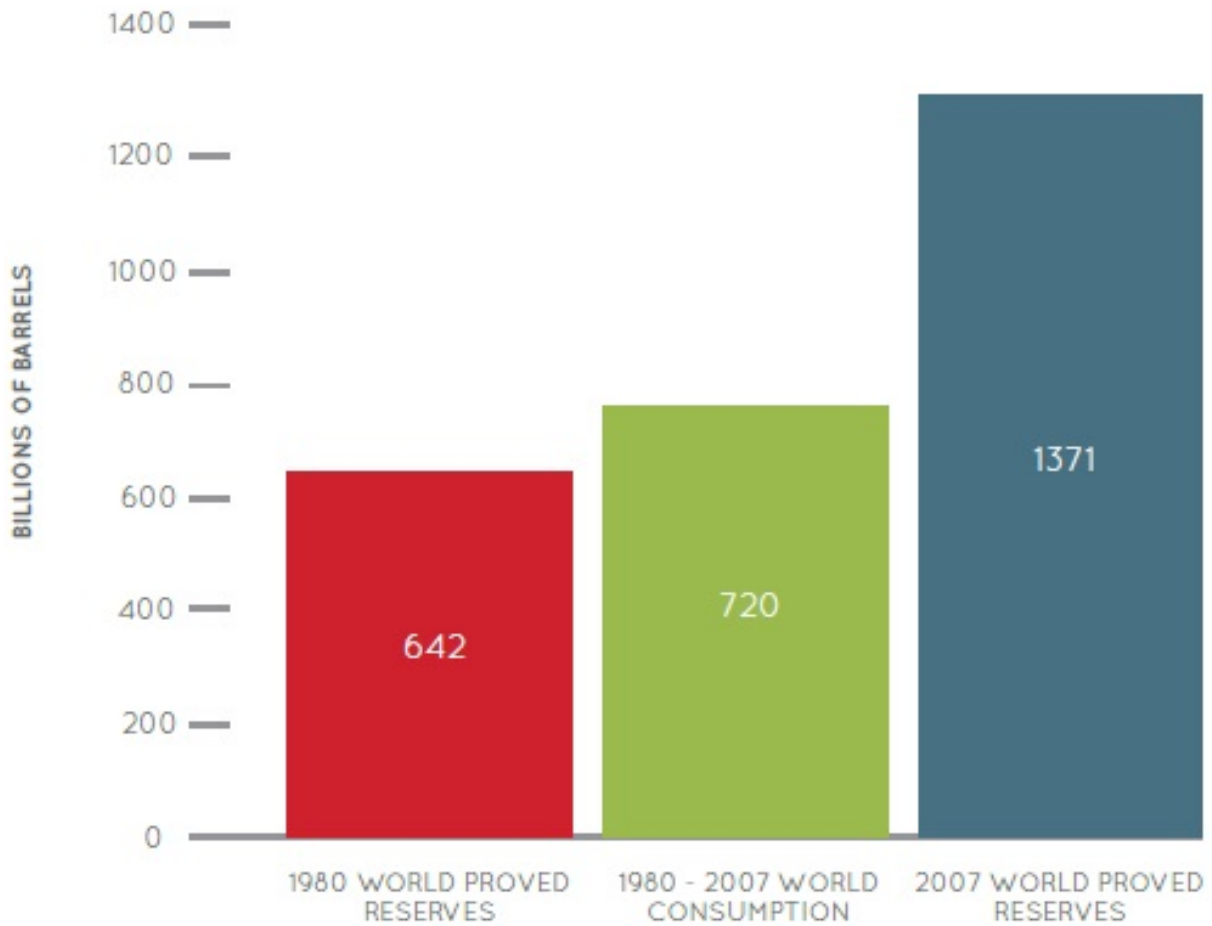


Figure 1.1: Energy consumption in the U.S. by source as a function of time [2].

According to recent reports [8], demand will surpass supply by 2015 if the world's oil depletion rate remains at its 2010 value. Besides being limited resources, fossil fuels pose serious problems of pollution. Hence, it is certain that the need for new sources of energy to replace fossil fuels will certainly become a critical problem in the near future.

¹Proven reserves are those reserves claimed to have a reasonable certainty (normally at least 90 % confidence) of being recoverable under existing economic and political conditions, with existing technology.

WORLD PROVED OIL RESERVES VERSUS PRODUCTION 1980–2007



SOURCE: ENERGY INFORMATION ADMINISTRATION,
INTERNATIONAL ENERGY STATISTICS: CRUDE OIL PROVED RESERVES,
[HTTP://TONTO.EIA.DOE.GOV/CFAPPS/IPDBPROJECT/IEDINDEXX3.CFM?TID=5&PID=57&AID=6&CID=REGIONS&SYID=1980&EYID=2010&UNIT=BB](http://tonto.eia.doe.gov/cfapps/ipdbproject/iedindexx3.cfm?tid=5&pid=57&aid=6&cid=regions&syid=1980&eyid=2010&unit=bb)

Figure 1.2: Proved oil reserves versus production [2].

1.2 Why Fusion

Nuclear fusion is a promising source of energy to respond to the increasing world energy demand. In the Sun and other stars, fusion reactions occur and are the main source of energy. Here, some nuclei recombine and become less massive. The final mass (m_f) is less than the initial mass (m_i), where the “missing mass” is converted into energy by the well known Einstein’s equation

$$E = (m_i - m_f)c^2, \quad (1.1)$$

where c is the speed of light.

The fusion process is safe, although it produces radioactive waste, similarly to fission reactions. However, fusion waste is much more manageable than fission, where instead of half-lives of $10^3 - 10^5$ years [9], we can have (with an appropriate choice of materials) half-lives of dozens of years [10]. The Deuterium source for the fusion process Deuterium-Tritium can easily be extracted from sea water, which implies that the fuel source for fusion is, in principle, inexhaustible. Tritium is bred from the reaction of Lithium with neutrons inside the reactor and the known sources of Lithium are sufficiently large to last thousands of years (see [11]). Also, see [12] for a special issue on ITER physics basics, specially the question of tritium breeding blankets and their feasibility.

Major accidents cannot take place since fusion reactors must be continuously fueled, so it can be stopped easily. There is no doubt that this process works, since it is what mainly powers the Sun and the stars, where gravitational energy holds the fusion protons together against the de-confining tendency due to thermal expansion and uncontrolled fusion reactions have been achieved on Earth, such as H-bombs [13]. Nowadays, the biggest challenge is to achieve fusion in a controlled manner (namely *plasma confinement*), which requires a detailed study on plasma physics. To confine a plasma, we need to maintain it in a stable equilibrium state, where the loss of particles and heat in the reactor must be slow enough for it to be self-sustained.

1.3 The Dynamics of Magnetically Confined Plasmas

Dwight R. Nicholson starts his book noting that "A plasma is a gas of charged particles, in which the potential energy of a typical particle due to its nearest neighbor is much smaller than its kinetic energy. The plasma state is the fourth state of matter" [14].

As the temperature of a material is raised, its state changes from solid to liquid and then to gas. Elevating it further, a high percentage of the gas atoms are ionized and a high temperature "gaseous" state is achieved. Here, the charge numbers of ions and electrons are nearly the same and, macroscopically, charge neutrality is maintained.

When ions and electrons move, they interact through the Coulomb force. This, in turn, has the form

$$F \propto \frac{1}{r^2}, \quad (1.2)$$

where r is the distance between the particles. Therefore, charged particles interact via long range forces. This leads to collective motion, characteristic of the plasma state.

The Nobel prize winning American chemist Irvin Langmuir first used this term (plasma) to describe an ionized gas in 1927. He was reminded of the way blood plasma carries red and white corpuscles much like an electrified fluid carries electrons and ions. Along with his colleague Lewi Tonks, Langmuir was investigating Tungsten-filament light bulbs.

Although nowadays there are several different machines with different geometries and configurations, in this thesis we will focus on a specific device designed to achieve nuclear fusion – a tokamak (Fig. 1.3). This is a low pressure gas discharge tube bent into a closed circular shape with a strong toroidal magnetic

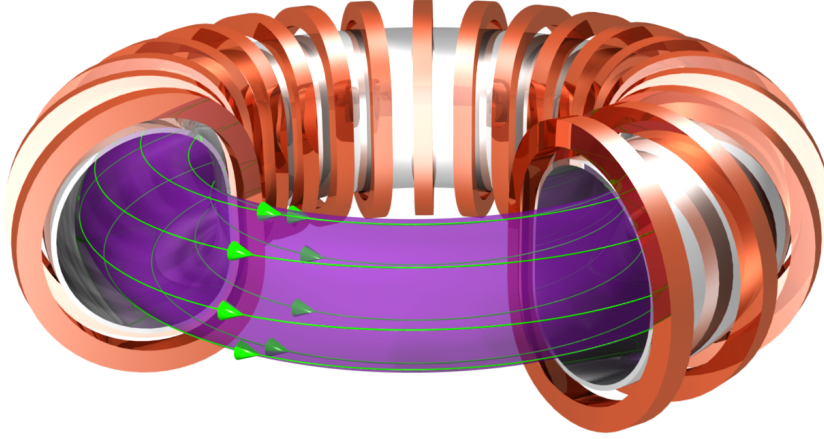
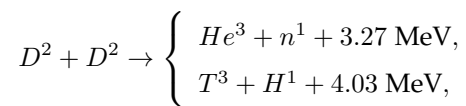


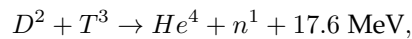
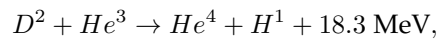
Figure 1.3: Schematic representation of a tokamak and the corresponding magnetic field lines (figure taken from [3]). The plasma is depicted in blue; the red annuli are the toroidal field coils.

field, B_ϕ , and a weaker poloidal field, B_θ , containing a high temperature plasma within the torus. This sort of containment is not easy to achieve. Charged particles cannot move easily through strong magnetic fields. If the fields are closed into embedded surfaces, then charged particles (like Deuterium and Tritium ions) trapped in this way and colliding with enough energy to overcome their repulsive Coulomb potential, will fuse and liberate energy through the law (1.1). External electric currents flowing in coils that stream around the torus generate the toroidal field. There is a much weaker superimposed poloidal field, B_θ , generated by an electric current, I_p , flowing toroidally in the plasma.

In a plasma consisting of Deuterium, or Deuterium mixed with Tritium, the fusion reactions



and



will occur frequently if the ion temperature, T_i , and the ion number density, n_i , are large enough. In a fusion reactor, these high values of T_i and n_i must be maintained for long enough time for the energy released by fusion to more than balance the energy losses due to radiation, conduction, convection and neutron flux.

There is an important statement, due to John D. Lawson in 1955. He decided, as a young engineer, to work out how ambitious the task of achieving fusion is. He formulated the so-called *Lawson's Criteria*, calculating the requirements for more energy to be created than is put in, and came up with a dependence

on three quantities - temperature (T), density (n) and confinement time (τ).

The confinement time is defined as the time that energy remains in the plasma before escaping. This parameter is crucial for fusion research and, from one microsecond in Lawson's time, it has improved to about one second in JET [15]. Lawson's Criteria says that in order to achieve ignition in a D-T (Deuterium-Tritium) plasma, the following inequality must hold [16]:

$$\tau n T > 5 \times 10^{21} \text{ s m}^{-3} \text{ keV.} \quad (1.3)$$

This is derived from the definition of confinement time as the energy content of the plasma divided by the power loss ($\tau = W/P_{\text{loss}}$) where the thermal energy of a plasma can be defined as the integral over volume

$$W = \int \frac{3}{2} k (n_e T_e + (n_D + n_T) T_i) dV, \quad (1.4)$$

where k is the Boltzmann's constant, n_e and T_e are the electron density and temperature, respectively, n_D and n_T are the ion densities of Deuterium and Tritium and T_i is their temperature. With the assumption that the Deuterium and Tritium densities are equal and the temperatures are roughly the same, we obtain

$$\frac{W}{V} \simeq 3 n_e k T, \quad (1.5)$$

where V is the volume. The volumetric equation for a hot plasma cloud (assuming that it has a Gaussian energy curve), which dictates the released energy [16] provides the number of fusions f per volume per time

$$f = n_D n_T \langle \sigma v \rangle = \frac{n_e^2}{4} \langle \sigma v \rangle, \quad (1.6)$$

where v is the relative velocity between the two species, σ is the fusion cross-section, the brackets are an average over the Maxwellian velocity distribution and we used $n_D = n_T = n_e/2$. To keep ignition, the energy produced within the plasma must be greater or equal than the one that leaves the plasma, leaving the balance

$$f E_{fp} \geq P_{\text{loss}}, \quad (1.7)$$

where E_{fp} the energy of the charged fusion products. Substituting f and P_{loss} , we obtain the standard definition of the Lawson Criterion, without the smaller contribution of the neutron emissions to plasma heating

$$n_e \tau T \geq \frac{12 k T^2}{E_{fp} \langle \sigma v \rangle}. \quad (1.8)$$

The minimum value of the RHS of (1.8) is reached for D-T near the temperature of 14 keV and the average $\langle \sigma v \rangle$ in this region is approximately $1.1 \times 10^{-24} \text{ m}^3/\text{s}$ (where T is in keV) leading to (1.3).

One of the major challenges today that keeps us from achieving Lawson's criteria is the extremely

complex interaction between the plasma and the device. This requires a profound study of the plasma-surface interaction and the plasma boundary (due to high energy and particle fluxes on surfaces). This is defined as the outermost closed magnetic flux surface contained in the device (in this case a tokamak). The shape of this boundary is often referred to as *plasma shape*. Unfortunately, this cannot be measured in a direct manner, but it is needed for control issues. Luckily, using indirect measurements of the magnetic field, one can estimate this shape in real time. Once the magnetic flux distribution is known, it is possible to reconstruct the plasma boundary.

Man-made plasmas almost always involve interaction with solid state materials, for example, electrodes or the walls containing vessel. This Plasma-Surface Interaction (PSI) often has profound effects on both the plasma and the material contained in the vessel. After all, they determine the boundary conditions in which the plasma basic properties are strongly dependent. At the interface between the solid and the plasma a thin net-charge layer called "Debye sheath" develops spontaneously [17]. The Debye sheath was first described also by Langmuir in 1923. As he wrote in [18] "electrons are repelled from the negative electrode, while positive ions are drawn towards it. Around each negative electrode there is thus a sheath of finite thickness containing only positive ions and neutral atoms".

From the sheath to the wall, charged particles collide with a solid surface which tends to stick the needed time to recombine. Having a finite probability of back scattering from a solid surface, ions pick up electrons from the surface and tend to return as neutrals. An equilibrium can be achieved, since electrons also stick to solid surfaces. Thus, a solid surface acts as a plasma charge sink.

Ionization of neutral particles by electron impact occurs throughout the tokamak. Resulting electron-ion pairs will then fall to the walls and stick to the surface until they recombine, forming neutrals that are released back to the plasma and ionized again. In this manner, a recycling steady-state is established, resulting in a constant plasma density.

1.4 The Scrape-Off Layer, SOL

There is a special device that controls the particle movement inside a tokamak, preventing the plasma touching the wall and controlling the plasma-solid interaction. This is usually done by a limiter or a divertor, where the magnetic field lines are not closed any more. The different types of limiters and divertors can be found in Fig. 1.4.

The Debye sheath is formed on the sides of the limiter due to the motion of particles to those locations. This way, the plasma boundary does not extend all the way to the walls due to fast loss of particles to the limiter, giving the particle a small time to diffuse beyond the limiter inner radius a , limiting the radius of the plasma column to a slightly larger value than a .

A key role is played by the Last Closed (magnetic) Flux Surface (LCFS). This is the last flux surface that goes outwards from the main plasma and does not touch a solid surface. In a surface on a region inside the LCFS magnetic lines are closed, while those further out are open. The region radially outboard of the LCFS is called the SOL (see Fig. 1.5).

For the purpose of this work, we focus on the poloidal limiter, a circular annular plate of inner radius

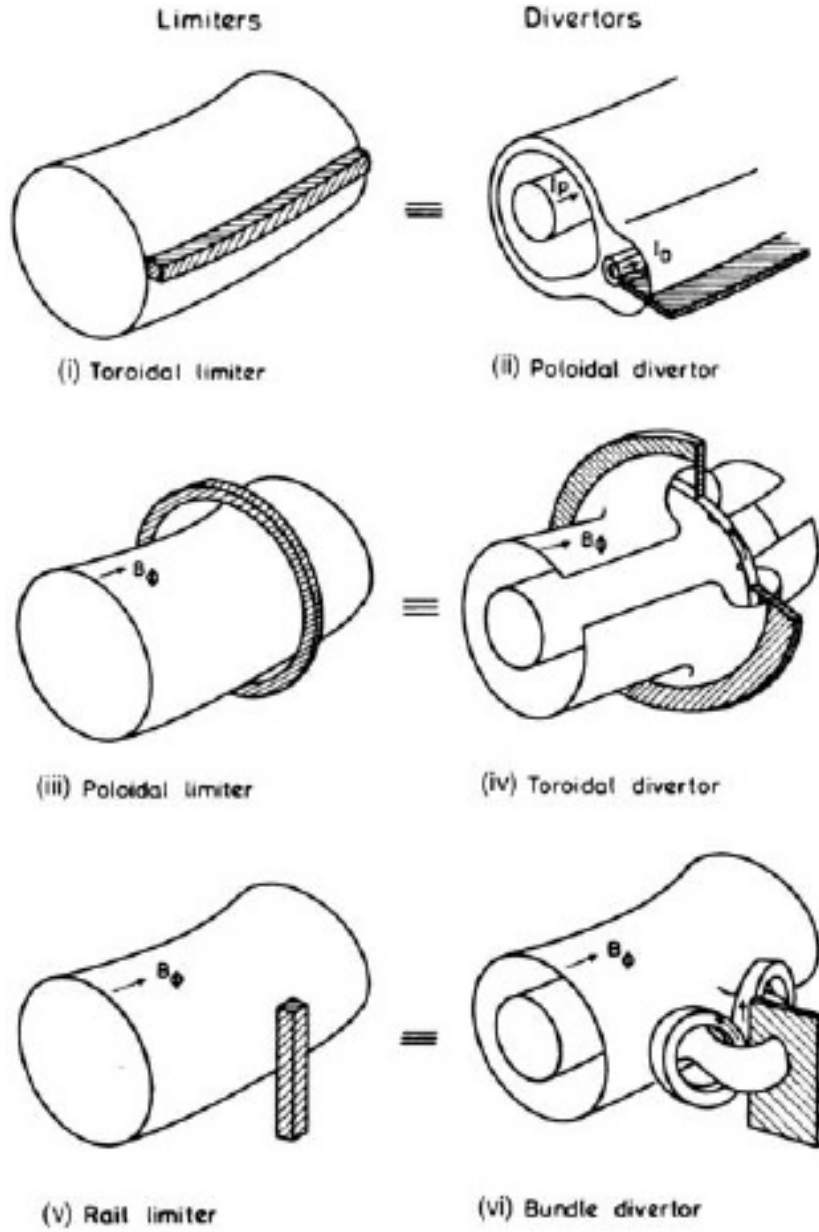


Figure 1.4: Different examples of poloidal and toroidal limiters [4].

$r = a_{\text{plasma}}$ and outer radius $r = a_{\text{wall}}$ (Fig. 1.4 (iii)). This limiter can be present at one or more toroidal locations. The typical parallel-to- \mathbf{B} distance that a particle has to travel in the SOL before striking a poloidal limiter is

$$L_z \simeq \frac{2\pi R}{N}, \quad (1.9)$$

where N is the number of poloidal limiters. This will be used as our connection length L_z .

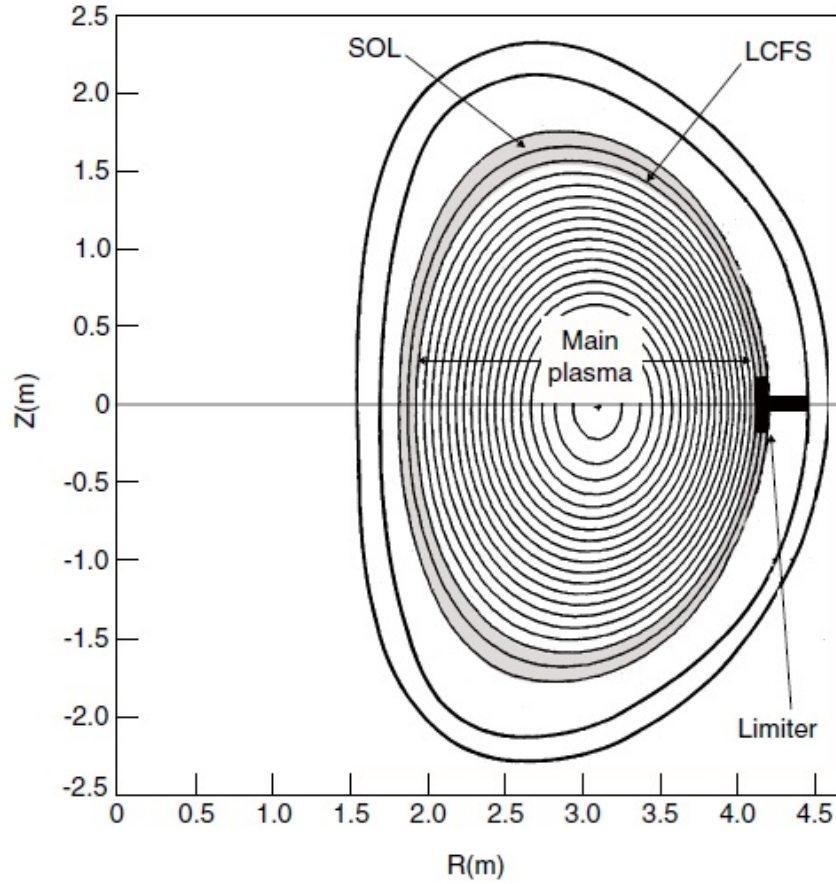


Figure 1.5: For the limiter configuration, the last closed magnetic flux surface, LCFS, is defined by the leading edge of the limiter. A JET-size plasma is shown (figure taken from [4]).

1.5 ISTTOK Geometry and the GBS code

1.5.1 ISTTOK

ISTTOK is a large aspect ratio tokamak with a circular cross-section with a poloidal (graphite) limiter ([19], [20]). The main goal of this thesis is to modify and apply the GBS code described in the next section in order to simulate the SOL environment of this device and compare with the existing results ([21], [22] and [23]).

Major Radius (R)	46 cm
Minor Radius (a)	8.5 cm
Toroidal magnetic field (B_T)	0.5 Tesla
Plasma current (I_p)	4-6 kA
Electron temperature (T_e)	20 eV
Density (n)	$0.4 - 1.2 \times 10^{18} \text{ m}^{-3}$

Table 1.1: Geometrical parameters of ISTTOK around the limiter [1].

With a typical toroidal magnetic field B_T of 0.5 T and a poloidal magnetic field of typically $B_p \simeq 3\%$ of B_T , the field lines are disposed in helical shape. The safety factor q , when an integer, is the number of toroidal transits required for the total magnetic field \mathbf{B} to make one poloidal transit. We can calculate

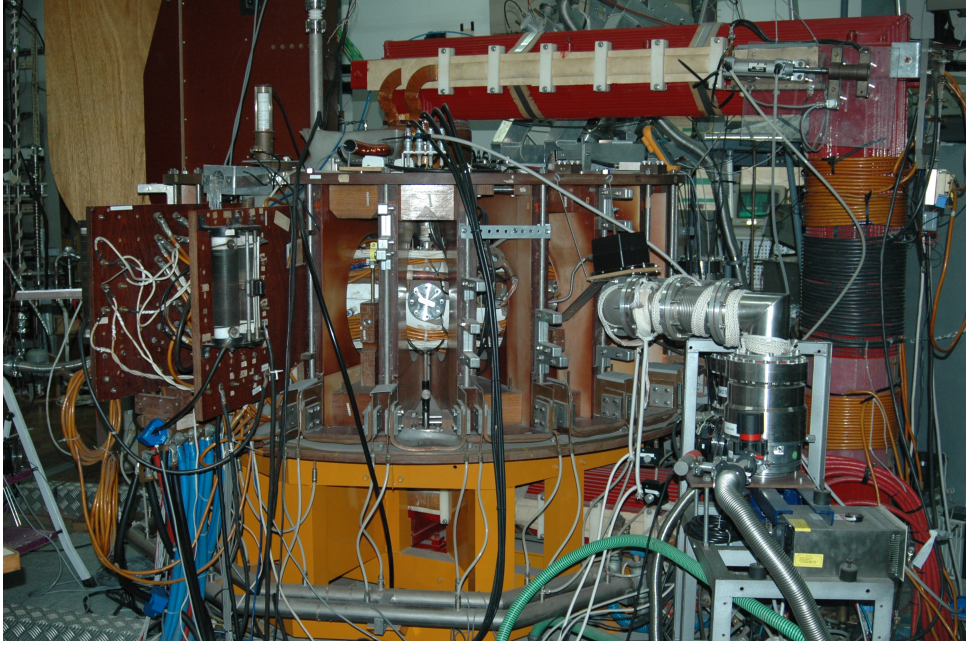


Figure 1.6: General view of ISTTOK [5].

approximately for a large aspect ratio ($\frac{R}{a} \gg 1$) circular cross-section tokamak (such as ISTTOK) the safety factor

$$q(a) \simeq \frac{aB_T}{RB_p}, \text{ as } \epsilon = \frac{a}{R} \rightarrow 0, \quad (1.10)$$

where estimating from Ampère's law the poloidal magnetic field and relating it with the plasma current provides

$$B_\theta(a) \simeq \frac{\mu_0 I_p}{2\pi a}. \quad (1.11)$$

In terms of edge diagnostics, four multi-pin probe systems have been installed at the same toroidal location at different poloidal positions in the tokamak ISTTOK edge plasma equally divided in the poloidal plane. Each probe system consists of five tungsten cylindrical pins with a diameter of 0.75 mm and an exposed length of 2.5 mm. These small free standing pins minimize the plasma perturbation. The inner-most pins are located at a minor radius of $r = 7.5$ cm ($r/a \simeq 0.9$) and the other two pins 5 mm further out ($r/a \simeq 0.95$). The detail edge diagnostics and experimental results are expressed in [1].

1.5.2 GBS Code

In this work we simulate ISTTOK SOL dynamics with the GBS code. This is based on the drift-reduced Braginskii equations and models the SOL plasma turbulence with proper boundary conditions derived from sheath dynamics [24]. It has been developed with the goal of simulating plasma SOL turbulence by evolving the full profiles of the various quantities with no separation between *perturbations* and *equilibrium*. These simulations can explore the self-consistent evolution and structure of the plasma

profiles in the presence of plasma density and heat input from the core of the fusion machine, cross-field transport driven by several plasma instabilities (interchange or drift wave instability, for example) and parallel losses at the sheaths, where the magnetic field lines terminate on the walls.

We use the GBS code to describe the evolution of several quantities, namely the plasma density, electric potential, electron and ion parallel velocities and electron and ion temperatures in the SOL. At first, the code was conceived to describe the 2D plasma dynamics in basic plasma physics devices [25] and then ported to more complex configurations incorporating a three dimensional model. It has been validated against experiments such as the TORPEX device ([26] and [27]), which is particularly suitable for the code validation since it is equipped with a large number of diagnostics. In this thesis, we developed the code to incorporate a poloidal limiter, such as the geometrical configuration of ISTTOK, and considered electrostatic turbulence in configurations with circular magnetic flux surfaces.

1.6 Scope and Outline of the Thesis

In this thesis, we shall investigate the turbulent regimes in ISTTOK's SOL. In order to define the main turbulent modes in this region, GBS simulations are presented, as well as linear investigations and comparison with experimental results.

The issue of plasma *blob* dynamics is not directly addressed. These are structures of enhanced plasma density relative to the background plasma [28], and they are measured near the edge of magnetized laboratory plasmas such as tokamaks, stellarators, simple magnetized tori and linear devices. In recent years, their study has substantially increased (see e. g. [29], [30] and [31]), as blob dynamics influence important mechanisms such as wall recycling and strength of heat and particle fluxes to the divertor or first wall. Blob dynamics is also influenced by SOL turbulence and the deeper understanding of edge turbulence in the plasma can improve our understanding of blob behavior in ISTTOK and other tokamaks.

In Chap. 2 we derive the set of equations used throughout the thesis and solved by GBS (adimensionalized drift-reduced Braginskii equations) together with the proper boundary and initial conditions. We also present a brief description of the numerical implementation of the code and ISTTOK's geometry.

In Chap. 3 the set of equations is linearized and the linear solver is described together with its numerical implementation. The main linear instabilities in the cold ion limit are described: they are Ballooning Modes (BM) and Drift Waves (DW). In order to accurately describe these modes, we assess at the influence of each parameter: electron mass, resistivity and plasma β_e , in order to identify an inertial, resistive and ideal branch of BM or inertial and resistive branch of DW, studying its growth rate as a function of the main SOL parameters. The *gradient removal hypothesis* is also presented; this suggests that turbulence is non-linearly saturated when the radial gradient of the background plasma pressure is of the same order of the radial gradient of the pressure fluctuations [32].

In Chap. 4 we present the simulation results, identifying the non-linear SOL turbulent regimes, comparing with the linear simulation and experimental results. An analysis is done on the dependence of these modes with SOL operational parameters, namely q , magnetic shear \hat{s} , resistivity ν , ion to electron

temperature ratio τ and the electromagnetic factor β_e (formal definitions in the next chapter).

In Chap. 5 the main results are described together with some possible improvements and future developments of this work.

Description of the Model and the GBS code

2.1 Braginskii Equations

In order to model the turbulence in the edge of a tokamak, one should define a set of reduced equations coherent with the specified regime. To allow the use of a fluid description, the collisionality needs to be high enough so that the plasma is close to thermodynamical equilibrium. This is usually true in the edge, where the temperatures are much lower than in the core because the distribution function becomes a Maxwellian in a time of the order of the collision time τ [33], which is proportional to $T^{3/2}$ (implying $d/dt \ll 1/\tau$). Despite the need of a model as complete as possible, there is a numerical complexity limit that nowadays computers can handle. At a kinetic level, the most complete description is given by the Boltzmann's equation. A widely used model to describe SOL turbulence is the drift reduced model based on the Braginskii equations [33]. In appendix A we present a detailed derivation of those fluid equations and a discussion of the appropriate closure scheme. The system of equations for each species s is given by

$$\frac{dn_s}{dt} + n_s \nabla \cdot \mathbf{V}_s = 0, \quad (2.1)$$

$$m_s n_s \frac{d\mathbf{V}_s}{dt} + \nabla p_s + \nabla \cdot \boldsymbol{\pi}_s - e_s n_s \left(\mathbf{E} + \frac{\mathbf{V}_s}{c} \times \mathbf{B} \right) = \mathbf{R}_s, \quad (2.2)$$

$$\frac{3}{2} \frac{dp_s}{dt} + p_s \nabla \cdot \mathbf{V}_s + \pi_{s_{ij}} \nabla_i V_{s_j} + \nabla \cdot \mathbf{q}_s = Q_s. \quad (2.3)$$

Here, $\frac{d}{dt} = \frac{\partial}{\partial t} + \mathbf{V}_s \cdot \nabla$, $p_s = n_s T_s$ is the plasma pressure, $\boldsymbol{\pi}_s$ the viscosity tensor, \mathbf{E} and \mathbf{B} the electric and magnetic fields respectively, \mathbf{q}_s the heat flux density, Q_s the energy flux density, \mathbf{V}_s the flow velocity of each species s and \mathbf{R}_s the density of momentum per unit time exchanged due to collision with other species.

The closure is done through the assumption that the plasma is collisional and is immersed in a strong magnetic field [34], which implies

$$\omega_{e,i} \tau_{e,i} \gg 1, \quad (2.4)$$

with $\omega_{e,i} = \frac{qB}{m_{e,i}c}$ the Langmuir frequency and $\tau_{e,i}$ the electron/ion collision times,

$$\tau_e = \frac{3\sqrt{m_e}T_e^{3/2}}{4\sqrt{2\pi}\lambda e^4 Z^2 n_e}, \quad \tau_i = \frac{3\sqrt{m_i}T_i^{3/2}}{4\sqrt{2\pi}\lambda e^4 Z^2 n_i}, \quad (2.5)$$

and $\lambda = 24 - \ln\left(\frac{\sqrt{n}}{T_e}\right)$ is the Coulomb logarithm. In ISTTOK we have $\omega_e\tau_e \simeq 123$.

In his paper [33], Braginskii expresses \mathbf{R} , π , \mathbf{q} and Q as proportional to \mathbf{V} , n , T and their gradients. The proportionality coefficients are called *transport coefficients* which are calculated under the hypothesis (2.4) and calculated to arbitrary order in

$$\epsilon = \frac{\rho}{L} \ll 1 \quad (2.6)$$

where ρ is the Larmor radius and L is the macroscopic length-scale. The first order moment of the collision operator $\mathbf{R} \equiv \mathbf{R}_e \equiv -\mathbf{R}_i$ can be written as a sum of a frictional and a thermal contribution $\mathbf{R} = \mathbf{R}_u + \mathbf{R}_T$

$$\mathbf{R}_u = ne \left(\frac{\mathbf{j}_{\parallel}}{\sigma_{\parallel}} + \frac{\mathbf{j}_{\perp}}{\sigma_{\perp}} \right), \quad \mathbf{j}_{\parallel,\perp} = en_e(\mathbf{V}_{\parallel,\perp i} - \mathbf{V}_{\parallel,\perp e}), \quad \sigma_{\perp} = \frac{e^2 n_e \tau_e}{m_e} \quad \sigma_{\parallel} = 1.96\sigma_{\perp}, \quad (2.7)$$

$$\mathbf{R}_T = -0.71n_e \nabla_{\parallel} T_e - \frac{3}{2} \frac{n_e}{\omega_e \tau_e} \mathbf{b} \times \nabla_{\perp} T_e, \quad \mathbf{b} = \frac{\mathbf{B}}{B}, \quad \nabla_{\parallel} = \mathbf{b} \cdot \nabla. \quad (2.8)$$

where σ_{\perp} and σ_{\parallel} are the perpendicular and parallel conductivities, respectively.

In the same manner, the electron heat flux can be described as a sum of two contributions $\mathbf{q}^e = \mathbf{q}_u^e + \mathbf{q}_T^e$. The ion heat flux q^i in (2.11) is shown neglecting terms of order $w_i\tau_i$.

$$\mathbf{q}_u^e = 0.71n_e T_e \mathbf{u}_{\parallel} + \frac{3}{2} \frac{n_e T_e}{\omega_e \tau_e} \mathbf{b} \times \mathbf{u}, \quad (2.9)$$

$$\mathbf{q}_T^e = -\chi_{\parallel}^e \nabla_{\parallel} T_e - \chi_{\perp}^e \nabla_{\perp} T_e - \frac{5}{2} \frac{cn_e T_e}{eB} \mathbf{b} \times \nabla T_e, \quad (2.10)$$

$$\mathbf{q}^i = -\chi_{\parallel}^i \nabla_{\parallel} T_i - \chi_{\perp}^i \nabla_{\perp} T_i + \frac{5}{2} \frac{cn_i T_i}{ZeB} \mathbf{b} \times \nabla T_i. \quad (2.11)$$

with $\mathbf{u} = \mathbf{V}_e - \mathbf{V}_i$ and the thermal conductivities (both parallel and perpendicular for electrons and ions) are given by ([33])

$$\chi_{\parallel}^e = 3.16 \frac{n_e T_e \tau_e}{m_e}, \quad \chi_{\perp}^e = 4.66 \frac{n_e T_e}{m_e \omega_e^2 \tau_e}, \quad (2.12)$$

$$\chi_{\parallel}^i = 3.9 \frac{n_i T_i \tau_i}{m_i}, \quad \chi_{\perp}^i = 2 \frac{n_i T_i}{m_i \omega_i^2 \tau_i}. \quad (2.13)$$

In the limit $\omega\tau \gg 1$ and aligning the z axis with the magnetic field, we obtain the stress tensor π

$$\pi_{xx} = -\frac{\eta_0}{2} (W_{xx} + W_{yy}) - \frac{\eta_1}{2} (W_{xx} - W_{yy}) - \eta_3 W_{xy}, \quad (2.14)$$

$$\pi_{yy} = -\frac{\eta_0}{2} (W_{xx} + W_{yy}) - \frac{\eta_1}{2} (W_{xx} - W_{yy}) + \eta_3 W_{xy}, \quad (2.15)$$

$$\pi_{zz} = -\eta_0 W_{zz}, \quad (2.16)$$

$$\pi_{xy} = \pi_{yx} = -\eta_1 W_{xy} + \frac{\eta_e}{2} (W_{xx} - W_{yy}), \quad (2.17)$$

$$\pi_{xz} = \pi_{zx} = -\eta_2 W_{xz} - \eta_4 W_{yz}, \quad (2.18)$$

$$\pi_{yz} = \pi_{zy} = -\eta_2 W_{yz} - \eta_4 W_{xz}, \quad (2.19)$$

$$\eta_0^e = 0.73 n_e T_e \tau_e, \quad \eta_1^e = 0.51 \frac{n_e T_e}{\omega_e^2 \tau_e}, \quad \eta_2^e = 4\eta_1^e, \quad (2.20)$$

$$\eta_3^e = -\frac{n_e T_e}{2\omega_e}, \quad \eta_4^e = 2\eta_3^e, \quad \eta_0^i = 0.96 n_i T_i \tau_i, \quad (2.21)$$

$$\eta_1^i = \frac{3}{10} \frac{n_i T_i}{\omega_i^2 \tau_i}, \quad \eta_2^i = 4\eta_1^i, \quad \eta_3^i = \frac{n_i T_i}{2\omega_i}, \quad \eta_4^i = 2\eta_3^i. \quad (2.22)$$

where the rate-of-strain tensor W is defined as

$$W_{\alpha,\beta} \equiv \frac{\partial V_\alpha}{\partial x_\beta} + \frac{\partial V_\beta}{\partial x_\alpha} - \frac{2}{3} \delta_{\alpha,\beta} \nabla \cdot \mathbf{V}. \quad (2.23)$$

It is interesting to note that in the absence of magnetic field we have $\pi = -\eta_0 W$. To conclude, the heat generation Q can be written as

$$Q_e = -\mathbf{R}_e \cdot \mathbf{u} - Q_i, \quad Q_i = \frac{3m_e n_e}{m_i \tau_e} (T_e - T_i). \quad (2.24)$$

The electron heat generation Q_e is composed of a Joule heating term due to friction with ions ($\mathbf{R}_e \cdot \mathbf{u}$) and a term due to the difference in temperature between them. The Joule heating term in Q_i is neglected, being $\approx m_e/m_i$ smaller than the Joule heating term due to friction ($\mathbf{R}_e \cdot \mathbf{u}$).

These are the so-called Braginskii equations. Since they are rigorously justified only for high collisionality, which implies τ_e and τ_i small. This is justified since they are proportional to $T_e^{3/2}$ and $T_i^{3/2}$ and these are low at the edge of the fusion plasma. Braginskii equations also describe dynamics at a wide range of timescales which can be very disparate from the dynamics of interest.

To better grasp which magnitudes we are referring to, it is known that in ISTTOK the ratio of temperatures from the core to the edge has a maximum of $\left(\frac{T_{e,\text{core}}}{T_{e,\text{edge}}}\right)^{3/2} \simeq 45$ and in densities $\frac{n_{\text{core}}}{n_{\text{edge}}} \simeq 8$ [1]. The value of τ_e in ISTTOK's edge is approximately $\tau_e \approx 2.56402 \times 10^{-6}$ s. In terms of time variations in the SOL, they are characterized by a scale much slower than the ion gyromotion and a spatial scale of the order of the Larmor radius at the sound speed c_s

$$\rho_s = \frac{c_s}{\omega_i}, \quad c_s^2 = \frac{T_e}{m_i}. \quad (2.25)$$

It is worthy to note that making use of the smallness of the mass ratio $\frac{m_e}{m_i}$ to approximate $\mathbf{V}_i \simeq \mathbf{V} + \mathcal{O}\left(\frac{m_e}{m_i}\right)$, $\mathbf{V}_e \simeq \mathbf{V} - \delta \frac{\mathbf{j}}{ne} + \mathcal{O}\left(\frac{m_e}{m_i}\right)$ with $\delta \equiv \frac{\rho}{L}$ and equation terms in order δ in the Braginskii equations leads to the simpler model that combines Navier-Stokes and Maxwell's equations known as MHD (Magnetohydrodynamics).

2.2 Drift Reduced Model

The dynamics present in Braginskii's equation presented above range from electron cyclotron frequency $w_{ce} \simeq 10^{11} s^{-1}$ up to the confinement time scale of order 1 s [6]. In order to eliminate fast time scale variations in our system, a drift reduced model is employed using (following [6])

$$\frac{\partial}{\partial t} \approx \mathbf{V}_{E \times B} \cdot \nabla \approx \frac{\rho_s^2}{L_\perp^2} \omega_i \ll \omega_i, \quad (2.26)$$

where, typically, at the region of interest ρ_s is much smaller than the typical equilibrium scale length L_\perp . On ISTTOK, $\rho_s/L_p \simeq 0.09$. The $\mathbf{E} \times \mathbf{B}$ velocity is

$$\mathbf{V}_{E \times B} = -\frac{c}{B} \nabla \phi \times \mathbf{b}, \quad (2.27)$$

where in general $\mathbf{E} = -\nabla \phi - \frac{1}{c} \frac{\partial \mathbf{A}}{\partial t}$. Thanks to fact that the plasma turbulence takes place on a much bigger spatial scale than the charge unbalancing, namely that

$$\rho_s \gg \lambda_D, \quad \text{where } \lambda_D \equiv \sqrt{\frac{T_e}{2\pi e^2 n}} \text{ is the Debye Length,} \quad (2.28)$$

we can assume a quasi neutral regime $n \equiv n_i = n_e$. Also embedded in the drift ordering is the distinction between dynamics parallel and perpendicular to the magnetic field $\mathbf{V}_s = V_{\parallel s} \mathbf{b} + \mathbf{V}_\perp$, with the turbulence essentially aligned with the field line, implying

$$|\nabla_{\parallel}| \ll |\nabla_{\perp}|. \quad (2.29)$$

Assuming that the viscous terms are small and performing the parallel and perpendicular splitting, we obtain

$$\mathbf{V}_{\perp e} = \mathbf{V}_{E \times B} + \mathbf{V}_{de}, \quad \mathbf{V}_{\perp i} = \mathbf{V}_{E \times B} + \mathbf{V}_{di} + \mathbf{V}_{pol}, \quad (2.30)$$

$$\mathbf{V}_{de} = -\frac{\mathbf{b} \times \nabla p_e c}{enB}, \quad \mathbf{V}_{di} = \frac{\mathbf{b} \times \nabla p_i c}{enB}, \quad (2.31)$$

with $\mathbf{V}_{de}/\mathbf{V}_{di}$ the electron/ion diamagnetic drift velocity. In terms of $\frac{\rho_i}{L_\perp}$ ordering, the diamagnetic drift velocity together with the $\mathbf{E} \times \mathbf{B}$ drift constitute the zeroth order approximation to $\mathbf{V}_{\perp i}$ ($\mathbf{V}_{\perp i0}$). The first

order term is the polarization velocity

$$\begin{aligned} \mathbf{V}_{pol} &= \frac{\mathbf{b}}{\omega_i} \times \frac{d\mathbf{V}_{\perp i0}}{dt} + \left[\mathbf{a} \times \left(\nabla \times \frac{\mathbf{b}}{\omega_i} \right) \cdot \nabla \right] \mathbf{V}_{\perp i0} + \left[\mathbf{a} \times \left(G\boldsymbol{\kappa} - \frac{\nabla G}{3} \right) \right] \\ &+ \left\{ \frac{\mathbf{a}}{p_i} \times \nabla_{\perp} \left[\frac{2p_i}{\omega_i} \nabla \cdot (\mathbf{b} \times \mathbf{V}_{\perp i0}) \right] - \frac{a}{p_i} \nabla_{\perp} \left(\frac{p_i}{2\omega_i} \nabla_{\perp} \cdot \mathbf{V}_{\perp i0} \right) \right\}, \end{aligned} \quad (2.32)$$

$$\mathbf{a} = \frac{v_{Ti}^2}{\omega_i} \mathbf{b}, \quad v_{Ti} = \sqrt{\frac{T_i}{m_i}}, \quad G = -\eta_0 \left(2\nabla_{\parallel} V_{\parallel} - \boldsymbol{\kappa} \cdot \mathbf{V} - \frac{\nabla \cdot \mathbf{V}}{3} \right),$$

with the definition of field curvature $\boldsymbol{\kappa} \equiv (\mathbf{b} \cdot \nabla) \mathbf{b}$ and G the stress function. In order to derive (2.32) the transfer momentum from electrons to ions \mathbf{R}_i has been neglected, the perpendicular component of the frictional and thermal forces in \mathbf{R}_e has been neglected and the stress tensor $\boldsymbol{\pi}$ is the sum of a viscous part and a Finite Larmor Radius (FLR) part (where $\frac{\rho_i}{L_{\perp}} \neq 0$) which take the form (neglecting η_1, η_2 and η_4 related terms in favor of η_3)

$$\begin{aligned} \boldsymbol{\pi}_{vis} &= \left(\mathbf{b}\mathbf{b} - \frac{\mathbf{I}}{3} \right) G, \\ \nabla \cdot \boldsymbol{\pi}_{FLR} &= -mn(\mathbf{V}_d \cdot \nabla) \mathbf{V} + p \left[\left(\nabla \times \frac{\mathbf{b}}{\omega} \right) \cdot \nabla \right] \mathbf{V} \\ &+ \nabla_{\perp} \left(\frac{p}{2\omega} \nabla \cdot \mathbf{V} \right) + \mathbf{b} \times \nabla \left(\frac{p}{2\omega} \nabla_{\perp} \cdot \mathbf{V} \right). \end{aligned} \quad (2.33)$$

For a more detailed derivation we refer the reader to [6]. We conclude with the divergence of the polarization drift that can be written as

$$\nabla \cdot (n\mathbf{V}_{pol}) = \nabla_{\perp} \frac{nc}{B\omega_i} \frac{d}{dt} \left(\mathbf{E}_{\perp} - \frac{\nabla_{\perp} p_i}{en} \right) + \left(\frac{\mathbf{b}}{3m_i\omega_i} \times \boldsymbol{\kappa} \cdot \nabla \right) G. \quad (2.34)$$

2.3 Vorticity and Continuity equations

In analogy with fluid dynamics where the vorticity is defined as the curl of the flow velocity, we define the vorticity as

$$\boldsymbol{\omega} = \nabla_{\perp}^2 \phi. \quad (2.35)$$

The continuity equation for each species s with the diamagnetic drift velocity and $\mathbf{E} \times \mathbf{B}$ velocity present in the perpendicular direction for both ions and electrons and the polarization drift added to the ion perpendicular velocity reads

$$\frac{\partial n_s}{\partial t} + \nabla \cdot [n (\mathbf{V}_{\perp s} + \mathbf{V}_{\parallel s})] = 0. \quad (2.36)$$

Subtracting both equations and imposing the quasi-neutrality condition we obtain the vorticity

equation (equivalent to $\nabla \cdot \mathbf{j} = 0$ implying that the displacement current is negligible)

$$-\frac{nc}{B\omega_i} \frac{d}{dt} \left(\omega + \frac{\nabla_{\perp}^2 p_i}{en} \right) + \frac{\mathbf{b}}{3m_i\omega_i} \times \boldsymbol{\kappa} \cdot \nabla G_i + \nabla_{\parallel} \frac{j_{\parallel}}{e} + \nabla \cdot n(\mathbf{V}_{di} - \mathbf{V}_{de}) = 0, \quad (2.37)$$

where the Boussinesq approximation (2.38) has been applied.

$$\nabla_{\perp} \frac{nc}{B\omega_i} \frac{d}{dt} \left(\mathbf{E}_{\perp} - \frac{\nabla_{\perp} p_i}{en} \right) \simeq -\frac{nc}{B\omega_i} \frac{d}{dt} \left(\omega + \frac{\nabla_{\perp}^2 p_i}{en} \right). \quad (2.38)$$

For the role of this approximation in the SOL region we refer the reader to [31].

2.4 Semi-Electrostatic Limit

In both the transverse and longitudinal direction of the magnetic field lines Braginskii equations contain both shear and compressional Alfvén waves, which are driven by magnetic field line tension. The compressional Alfvén wave is several orders of magnitude faster than the typical turbulent fluctuations (which typically occur at time scales of order 10^{-6} s), so this dynamics must be removed. For example in ISTTOK's SOL, the Alfvén velocity $V_A \simeq 10^7$ m/s and $\omega_i \simeq 10^4$ s $^{-1}$.

Choosing a vector potential \mathbf{A} purely parallel to the equilibrium magnetic field, being ψ the poloidal flux function,

$$\delta \mathbf{A} = -\psi \mathbf{b}, \quad (2.39)$$

achieves this goal. Assuming that

$$\beta \equiv 8\pi \frac{P}{B^2} \ll 1, \quad (2.40)$$

and noting that typically, the scale lengths in the parallel direction are much larger than the ones in the perpendicular direction, we can write the perturbed magnetic field as [24]

$$\delta \mathbf{B} = -\nabla \times (\psi \mathbf{b}) \simeq \mathbf{b} \times \nabla_{\perp} \psi = \delta \mathbf{B}_{\perp}. \quad (2.41)$$

In this manner, we can write the electric field and the Ampere's law as

$$\mathbf{E} = -\nabla \phi + \frac{1}{c} \frac{\partial \psi}{\partial t} \mathbf{b}, \quad (2.42)$$

$$\nabla_{\perp}^2 \psi = \frac{4\pi}{c} j_{\parallel}. \quad (2.43)$$

Also, there is a contribution due to the magnetic perturbations in the parallel derivative

$$\nabla_{\parallel} = \mathbf{b} \cdot \nabla + \frac{\mathbf{b}}{B} \times \nabla_{\perp} \cdot \nabla. \quad (2.44)$$

2.5 Parallel Motion

Projecting the momentum equations (2.2) along the parallel direction and retaining the parallel component of \mathbf{R}_e yields

$$m_e \frac{d^e V_{\parallel e}}{dt} = -\frac{\nabla_{\parallel} p_e}{n} - \frac{2}{3} \nabla_{\parallel} G_e + e \nabla_{\parallel} \phi - \frac{e}{c} \frac{\partial \psi}{\partial t} + \frac{e j_{\parallel}}{\sigma_{\parallel}} - 0.71 \nabla_{\parallel} T_e, \quad (2.45)$$

with the electron total time derivative $\frac{d^e}{dt} \equiv \frac{\partial}{\partial t} + (\mathbf{V}_{E \times B} + \mathbf{V}_{\parallel e}) \cdot \nabla$ and considering that the FLR part of the stress tensor is perpendicular to the magnetic field yielding $\nabla \cdot \boldsymbol{\pi}_e = \frac{2}{3} \nabla_{\parallel} G_e$. The diamagnetic contribution has canceled out by the first term in the $\nabla \cdot \boldsymbol{\pi}_{FLRe}$ equation.

The evolution of the ion parallel velocity is obtained adding the parallel components of the electron and ion momentum equations neglecting the $\boldsymbol{\pi}_e$ tensor since both FLR and viscous contributions are smaller than their ion counterpart by a factor of m_e and $\sqrt{m_e}$ respectively

$$m_i \frac{dV_{\parallel i}}{dt} = -\frac{\nabla p}{n} - p_i \nabla \times \frac{\mathbf{b}}{w_i} \cdot \nabla V_{\parallel i} - \frac{2}{3} \nabla_{\parallel} G_i. \quad (2.46)$$

2.6 Temperature Equations

For the electron temperature, we neglect the frictional part of heating, the second term in the thermal force (2.8) and the electron-ion heat transfer in the heat generation Q_e and the term proportional to χ_{\perp}^e and the second term in (2.9) in the heat flux term q_e since it is smaller than χ_{\parallel}^e by a factor $\omega_e \tau_e$. For the ion temperature, we neglect the electron-ion heat transfer ($Q_i = 0$) and the terms proportional to χ_{\perp}^i and to χ_{\parallel}^i in the heat flux \mathbf{q}_i since χ_{\perp}^i is smaller than χ_{\parallel}^i by a factor $\omega_i \tau_i$ and the latter is smaller than χ_{\parallel}^e by a factor $\sqrt{\frac{m_e}{m_i}}$.

Through (2.47) and with the simplifications above, the equation for both the electron and ion temperature is

$$\begin{aligned} \frac{3}{2} n \left(\frac{d}{dt} + \mathbf{V}_{de} \cdot \nabla \right) T_e + p_e \nabla \cdot (\mathbf{V}_{\perp e} + \mathbf{V}_{\parallel e}) - \frac{5c}{2e} \nabla \cdot \left(\frac{p_e \mathbf{b}}{B} \times \nabla T_e \right) \\ - 0.71 T_e \nabla_{\parallel} j_{\parallel} - \nabla \cdot (\chi_{\parallel}^e \nabla_{\parallel} T_e) = 0, \end{aligned} \quad (2.47)$$

$$\frac{3}{2} n \left(\frac{d}{dt} + \mathbf{V}_{di} \cdot \nabla \right) T_i + p_i \nabla \cdot (\mathbf{V}_{\perp i} + \mathbf{V}_{\parallel i}) + \frac{5c}{2e} \nabla \cdot \left(\frac{p_i \mathbf{b}}{B} \times \nabla T_i \right) = 0.$$

In order to evaluate the ion equation in (2.47) numerically, the term $\nabla \cdot \mathbf{V}_{pol}$ has to be evaluated. The term $p_i \nabla \cdot (\mathbf{V}_{\perp i} + \mathbf{V}_{\parallel i})$ may be eliminated through the ion continuity equation

$$p_i \nabla \cdot (\mathbf{V}_{\perp i} + \mathbf{V}_{\parallel i}) = -T_i \left(\frac{dn}{dt} + \mathbf{V}_{di} \cdot \nabla n \right) = -T_i \frac{dn}{dt} + n \mathbf{V}_{di} \cdot \nabla T_i, \quad (2.48)$$

bearing in mind that $\mathbf{V}_{di} \cdot \nabla p_i = 0$. We can also rewrite

$$\frac{5}{2} \frac{c}{e} \nabla \cdot p_i \left(\frac{\mathbf{b}}{B} \times \nabla T_i \right) = -\frac{5}{2} n \mathbf{V}_{di} \cdot \nabla T_i + \frac{5}{2} \frac{c}{e} \left(\nabla \times \frac{\mathbf{b}}{B} \right) \cdot \nabla T_i. \quad (2.49)$$

In the total derivative, the term $\mathbf{V}_{pol} \cdot \nabla$ is much smaller than the other contributions, being therefore neglected (but retaining as before the term proportional to $\nabla \cdot \mathbf{V}_{pol}$). Substituting back everything, the ion equation that can be used numerically is given by

$$\frac{3n}{2} \frac{dT_i}{dt} + T_i [n \nabla \cdot (\mathbf{V}_{E \times B} + \mathbf{V}_{\parallel e}) + \nabla \cdot (n \mathbf{V}_{de})] + \frac{5}{2} \frac{c}{e} p_i \left(\nabla \times \frac{\mathbf{b}}{B} \right) \cdot \nabla T_i = 0. \quad (2.50)$$

2.7 GBS Model

We have described so far the set of drift-reduced equations describing the dynamics of plasma density, vorticity, electron and ion parallel velocities and electron and ion temperatures. In order to summarize them in a straightforward numerical form we introduce the curvature operator C , the Poisson brackets operator, the adimensionalized resistivity ν (2.52), the ion to electron temperature ratio τ , the reference ion sound speed c_{s0} and the plasma parameter β .

$$C(f) = \frac{B}{2} \left(\nabla \times \frac{\mathbf{b}}{B} \right) \cdot \nabla f, \quad [\phi, f] = \mathbf{b} \cdot (\nabla \phi \times \nabla f), \quad (2.51)$$

$$\nu = \frac{e^2 n R}{m_i \sigma_{\parallel} c_{s0}}, \quad c_{s0} = \sqrt{\frac{T_{e0}}{m_i}}, \quad \tau = \frac{T_{i0}}{T_{e0}}, \quad \beta = \frac{n_0 T_{e0}}{\frac{B^2}{8\pi}}. \quad (2.52)$$

With these definitions, we can express [24]

$$\nabla \cdot (n \mathbf{V}_{de}) = -\frac{2c}{eB} C(p_e) \quad (2.53)$$

$$\nabla \cdot (n \mathbf{V}_{E \times B}) = \frac{c}{B} [\phi, n] + \frac{2cn}{B} C(\phi), \quad (2.54)$$

$$G_i = -3\eta_{0i} \left[\frac{2}{3} \nabla_{\parallel} V_{\parallel i} + \frac{C(\phi)}{3} + \frac{c}{enB} C(p_i) \right], \quad (2.55)$$

$$G_e = -3\eta_{0e} \left[\frac{2}{3} \nabla_{\parallel} V_{\parallel e} + \frac{C(\phi)}{3} + \frac{c}{enB} C(p_e) \right], \quad (2.56)$$

$$\nabla \cdot (n \mathbf{V}_{\parallel e}) = n \nabla_{\parallel} V_{\parallel e} + V_{\parallel e} \nabla_{\parallel} n, \quad (2.57)$$

where in the last equation $\nabla \cdot \mathbf{b}$ has been neglected (a direct consequence of neglecting finite aspect ratio effects).

In the model, diffusion operators \mathcal{D} are introduced for numerical purposes. Acting on an arbitrary field A , in general terms the diffusion operator takes the form (2.58). Its full form depends on the quantity A . As an example, for the electron temperature term, the diffusion coefficient $\mathcal{D}_{T_e}^{\parallel}$ is derived from the

term $\nabla \cdot (\chi_{\parallel e} \nabla_{\parallel} T_e)$ supposing $\chi_{\parallel e}$ constant.

$$\frac{\partial A(\mathbf{r}, t)}{\partial t} = \nabla \cdot (\mathcal{D}_A(A, \mathbf{r}) \nabla A(\mathbf{r}, t)). \quad (2.58)$$

With the definitions above, the system of equations are solved in a normalized form by GBS with the standard gyro-Bohm normalization (with ρ_s and c_s). We normalize n to the reference density n_0 , T_e and T_i to the reference temperatures T_{e0} and T_{i0} , ϕ to $\frac{T_{e0}}{e}$, $V_{\parallel e}$ and $V_{\parallel i}$ to c_{s0} (and c_s to c_{s0}), ψ to $\frac{\beta c m_i c_{s0}}{2e}$ and time t to $\frac{R}{c_{s0}}$ where R is the major radius. Lengths in the perpendicular direction are normalized to $\rho_{s0} = \frac{c_{s0}}{w_i}$ and in the parallel direction to R .

With the coupling $\nabla_{\perp}^2 \psi = n(V_{\parallel i} - V_{\parallel e})$ and $\nabla_{\perp}^2 \phi = w$ and with the notation

$$[\phi,]A \equiv [\phi, A], \quad \mathcal{D}_A A \equiv \mathcal{D}_A(A), \quad (2.59)$$

the complete adimensionalized system of equations with source terms S_{α} is given by the system (2.60)-(2.65) where $\Omega = \omega + \tau \nabla_{\perp}^2 T_i$ and $U_{\parallel e} = \frac{m_e}{m_i} V_{\parallel e} + \frac{\beta_e}{2} \psi$ (for a more detailed derivation see [35]).

$$\frac{\partial n}{\partial t} = -\frac{R}{B\rho_{s0}} [\phi, n] - \nabla_{\parallel} (n V_{\parallel e}) + \frac{2n}{B} \left[C(T_e - \phi) + \frac{T_e}{n} C(n) \right], \quad (2.60)$$

$$\begin{aligned} \frac{\partial \Omega}{\partial t} = & -\frac{R}{B\rho_{s0}} [\phi, \Omega] - V_{\parallel i} \nabla_{\parallel} \Omega + B^2 \nabla_{\parallel} j_{\parallel} + \frac{B}{3n} C(G_i) \\ & + B^2 j_{\parallel} \nabla_{\parallel} \log(n) + 2BC(T_e + \tau T_i) + 2BC(n) \frac{T_e + \tau T_i}{n}, \end{aligned} \quad (2.61)$$

$$\frac{\partial U_{\parallel e}}{\partial t} = -\frac{R}{B\rho_{s0}} \frac{m_e}{m_i} ([\phi, V_{\parallel e}] + V_{\parallel e} \nabla_{\parallel} V_{\parallel e}) + \nabla_{\parallel} \phi - (1.71 \nabla_{\parallel} + \nabla_{\parallel} \log(n)) T_e - \frac{2}{3} \nabla_{\parallel} G_e + \nu j_{\parallel}, \quad (2.62)$$

$$\frac{\partial V_{\parallel i}}{\partial t} = -\frac{R}{B\rho_{s0}} [\phi, V_{\parallel i}] - V_{\parallel i} \nabla_{\parallel} V_{\parallel i} - \frac{2}{3} \nabla_{\parallel} G_i - (\nabla_{\parallel} + \nabla_{\parallel} \log(n)) (T_e + \tau T_i), \quad (2.63)$$

$$\begin{aligned} \frac{\partial T_e}{\partial t} = & -\frac{R}{B\rho_{s0}} [\phi, T_e] - V_{\parallel e} \nabla_{\parallel} T_e - \frac{2}{3} T_e \nabla_{\parallel} V_{\parallel e} + \frac{2}{3} 0.71 T_e (\nabla_{\parallel} + \nabla_{\parallel} \log(n)) j_{\parallel} \\ & + \frac{4}{3} \frac{T_e}{B} \left(\frac{7}{2} C(T_e) + \frac{T_e}{n} C(n) - C(\phi) \right), \end{aligned} \quad (2.64)$$

$$\begin{aligned} \frac{\partial T_i}{\partial t} = & -\frac{R}{B\rho_{s0}} [\phi, T_i] - V_{\parallel i} \nabla_{\parallel} T_i + \frac{4}{3} \frac{T_e^2}{B} \frac{C(n)}{n} \\ & + \frac{4}{3} \frac{T_e}{B} C \left(T_e + \tau \frac{5}{2} T_i - \phi \right) + \frac{2}{3} T_i (j_{\parallel} \nabla_{\parallel} \log(n) - \nabla_{\parallel} V_{\parallel e}), \end{aligned} \quad (2.65)$$

2.8 ISTTOK Geometry

The system of equations (2.60) to (2.65) is stated for a general layout of equilibrium magnetic field. The configuration of interest is ISTTOK's geometry, which uses a poloidal limiter. Due to this fact, the magnetic field lines in the poloidal plane have geometry represented in Fig. 2.1. This asserts the poloidal symmetry present in ISTTOK's geometry and, therefore, we should also expect this symmetry in the simulation results (as opposed to a toroidal limiter that provides toroidal symmetry). We also consider an $s - \alpha$ geometry [36] (where operators are computed in the large aspect ratio limit $\epsilon = a/R \rightarrow 0$) and with the poloidal limiter located at $z = 0$.

A right handed coordinate system $[y, x, z]$ is used, where x is the flux coordinate and corresponds to the radial direction (since we work in a circular magnetic flux surface), z is a coordinate parallel to the total magnetic field \mathbf{B} and y is the coordinate perpendicular to both x and z . In the large aspect ratio limit, the plane (x, y) coincides with the poloidal plane, which implies $y = a\theta$, where $0 < \theta < 2\pi$ is the poloidal angle and $0 < z < 2\pi$.

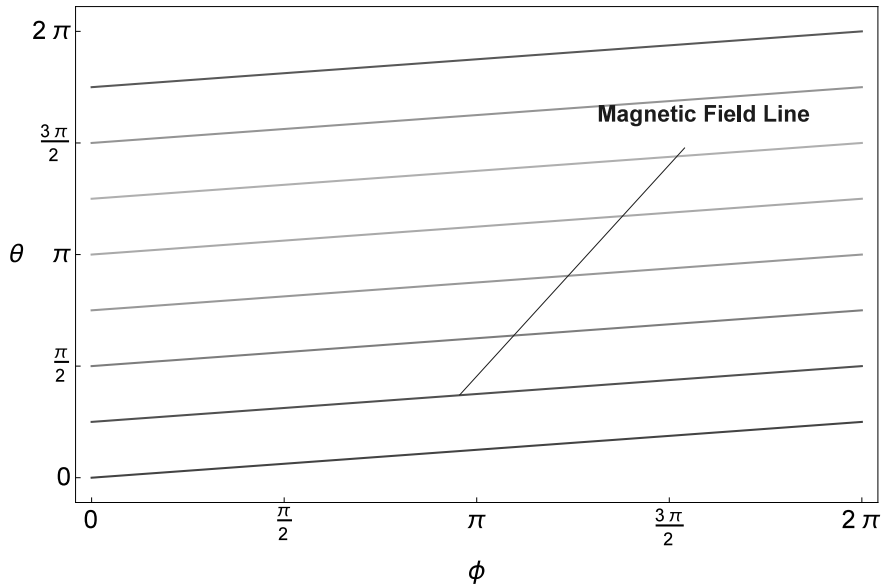


Figure 2.1: Representation of the magnetic field line geometry at ISTTOK with a $q = 8$, where θ is the poloidal angle and ϕ the toroidal one (in radians).

In this geometry, the previously defined operators take the form (in a general form of $\hat{s} \neq 0$)

$$[f, g] = \partial_y f \partial_x g - \partial_x f \partial_y g, \quad (2.66)$$

$$C(f) = \sin \theta \partial_x f + \left(\sin \theta \frac{y \hat{s}}{a} + \cos \theta \right) \partial_y f, \quad (2.67)$$

$$\nabla_{\perp}^2 f = \partial_x^2 f + \frac{2y \hat{s}}{a} \partial_{x,y}^2 f + \left[1 + \left(\frac{y \hat{s}}{a} \right)^2 \right] \partial_y^2 f, \quad (2.68)$$

$$\nabla_{\parallel} f = \partial_z f + \frac{R \beta}{2 \rho_{s0}} [\psi, f]. \quad (2.69)$$

In this system, the pitch of the field line varies radially in the presence of magnetic shear. This effect is studied in chapter 3. In table 2.1 we state the code input parameters for ISTTOK in GBS units (lengths normalized to ρ_s).

Major Radius (R)	503.7
Minor Radius (a)	93.08
SOLwidth	16.43
β	2.577×10^{-5}
L_y	584.8
ν	1.137×10^{-3}
m_e/m_i	0.00055
q	8

Table 2.1: Code input parameters for ISTTOK in GBS units [1].

2.9 Numerical Implementation

The domain is discretized along the x , y and z direction, with the grid points defined as

$$x_i = \left(i - \frac{1}{2} \right) \Delta x, \quad i = 0, \dots, N_x + 1, \quad \Delta x = \frac{Lx}{N_x}, \quad (2.70)$$

$$y_j = \left(j - \frac{1}{2} \right) \Delta y, \quad i = 0, \dots, N_y + 1, \quad \Delta y = \frac{Ly}{N_y}, \quad (2.71)$$

$$z_k = \begin{cases} \left(k - \frac{1}{2} \right) \Delta z, & i = 0, \dots, N_z + 1, \quad \Delta z = \frac{Lz}{N_z}, & \text{for } A = V_{\parallel e}, V_{\parallel i}, \\ k \Delta z, & i = 0, \dots, N_z, & \text{for } A = n, T_e, T_i, w. \end{cases} \quad (2.72)$$

There are N_x , N_y , N_z intervals in the (x, y, z) direction, numbered from 1 to N_x , N_y , N_z . Each physical quantity A is written $A_{i,j,k} \equiv A(x_i, y_j, z_k)$ with each index running from the intervals defined from 2.70 to 2.72. The physical domain runs from 1 to N_{xyz} but one ghost cell is introduced to the left and right of each domain to account for the width of the finite difference scheme.

In the x and y directions, the grid points are located at the middle of the interval. There is formally no

z derivative in the equations but it appears in the parallel gradient operator. For numerical reasons, the parallel gradient terms are computed at the middle of the interval $z_{k+\frac{1}{2}}$, being shifted by half an interval to the left for $V_{||e}$ and $V_{||i}$.

In order to reduce the computational cost of the simulations, we take advantage of the fact that turbulence is mostly aligned in the direction parallel to the field. For this purpose, we choose N_y and N_z in such a way that the discretization points fall on the field lines, *i.e.* we impose

$$\Delta_j = \frac{N_y}{N_z q} \in \mathbb{N}, \quad (2.73)$$

which allows the use of a low resolution in the toroidal direction. The parallel derivative can then be approximated as

$$(\mathbf{b} \cdot \nabla) A_{i,j,k} \simeq \frac{1}{2\Delta z} (A_{i,j+\Delta j,k} - A_{i,j-\Delta j,k}). \quad (2.74)$$

In the x and y directions a standard centered finite difference scheme is used

$$\left. \frac{\partial A}{\partial x} \right|_{i,j,k} \simeq \frac{1}{2\Delta x} (A_{i+1,j,k} - A_{i-1,j,k}), \quad (2.75)$$

except the Poisson brackets, which are discretized according to the Arakawa scheme [37]. A second order centered finite difference scheme is used on the Laplacian operator and a fourth order Runge-Kutta scheme is used for the time stepping. In order to ensure the positivity of n , T_e and T_i , Eqs. (2.60) to (2.65) are rewritten in terms of $\theta_n = \log n$, $t_e = \log T_e$ and $t_i = \log T_i$.

The parallelization scheme is done with a standard MPI domain decomposition. The total number of processes is $N_p \equiv N_{P_x} N_{P_z}$, where the physical domain in x and z is divided as equally as possible into N_{P_x} and N_{P_z} parts. With the addition of one ghost cell to the left and to the right, each array representing the physical quantity $A(x, y, z)$ will have a size of $\left(\frac{N_x}{N_{P_x}} + 2\right) (N_y + 2) \left(\frac{N_z}{N_{P_z}} + 2\right)$ elements in each process. For more details we refer to [24].

2.10 Boundary and Initial Conditions

Our system of equations is solved in a periodic domain in the poloidal direction, but there is a finite extension of the domain in the toroidal direction due to the presence of the poloidal limiter and in the radial direction. In the toroidal direction the plasma touches the conducting limiter and spontaneously generates a thin layer contiguous to the wall, the so-called sheath (see Fig. 2.2), where quasi-neutrality and the drift approximations are broken. As $m_e \ll m_i$ electrons tend to reach the wall at a higher rate than the ions and in order to prevent an electron loss to the wall larger than the ion loss, the plasma naturally builds up a potential drop between the bulk plasma and the wall.

An extensive derivation of the boundary conditions at the magnetic presheath entrance is presented in [38] for $\tau = 0$ and in [35] for $\tau > 0$. GBS allows the choice between Neumann and Dirichlet boundary conditions for all the fields but for the parallel electron and ion velocities, Bohm's boundary conditions

are implemented. These are derived using a detailed kinetic treatment of the electron dynamics in the sheath region (see [4]).

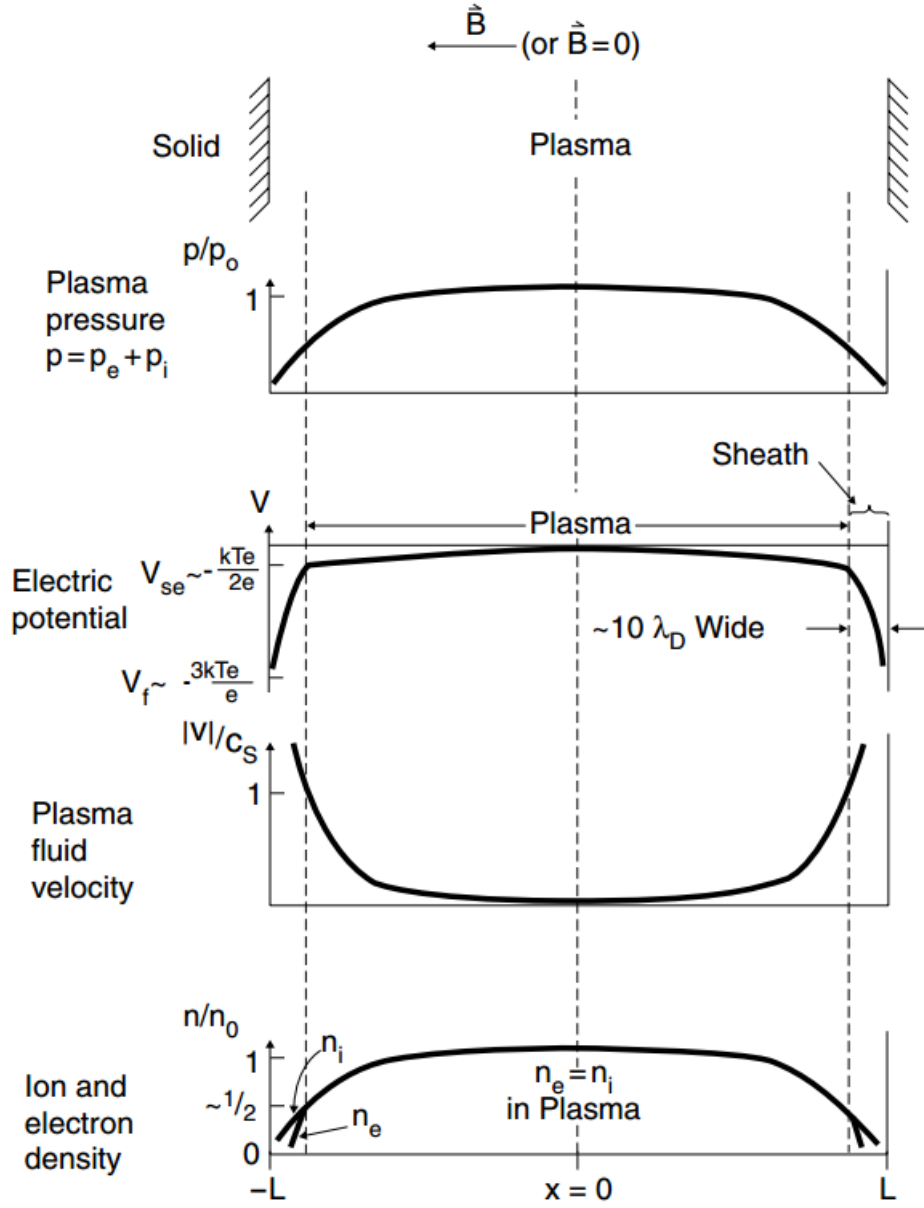


Figure 2.2: Schematic of the variation of plasma pressure, electric potential, plasma velocity and ion/electron densities in the plasma between two semi-infinite planes (figure taken from [4]).

So at the sheath, particularly at $z = 0$ and at $z = 2\pi$ (at the limiter), we use

$$V_{\parallel e_s} = \pm \sqrt{T_e} e^{\Lambda - \frac{\phi}{T_e}}, \quad (2.76)$$

$$V_{\parallel i_s} = \pm \sqrt{T_e} \sqrt{1 + \tau \frac{T_i}{T_e}}. \quad (2.77)$$

Since most of the particles are lost at the limiter preventing them from reaching the vessel wall, the conditions applied to the outer edge of the simulation domain do not influence the turbulence dynamics

significantly. To mimic the plasma outflow from the core, a particle and heat source mimic the plasma outflow from the core, being located at a finite distance from the inner boundary of the domain. The region between the source and the inner boundary of the domain is not taken into account for turbulence analysis.

Each quantity is then initialized as $A = A_0 + \tilde{A}(y, x, z)$, where A_0 has a constant value and \tilde{A} is a random field whose amplitude can be chosen. For $V_{\parallel e}$ and $V_{\parallel i}$ a profile varying linearly between the two values of each $V_{\parallel e_s}$ and $V_{\parallel i_s}$ is used. The source term for the fields $A = n, T_e, T_i$ is defined as

$$\text{Source} = A_f e^{-\frac{(x-x_s)^2}{\sigma_s^2}}, \quad (2.78)$$

where x_s represents the radial position of the source, A_f its strength and σ_s its width. With each new simulation, a quasi-stationary state is reached after a transient phase, in which the plasma, generated by the source and transported by turbulence, is eventually removed from the system by losses at the vessel walls. Our analysis is focused primarily in the quasi-stationary state.

Analysis of Turbulence Regimes in ISTTOK's SOL

3.1 Linearized System and Linear Solver

We linearize the system of Eqs. (2.60) to (2.65) assuming that the equilibrium n and T can be described as $f = f_{00} \left(1 + \frac{x}{L_f}\right)$ where f_{00} represents the equilibrium value and looking for solutions of the form $e^{\gamma t}$ where γ is the linear growth rate of the mode [39].

With $\Omega = \omega + \tau \nabla_{\perp}^2 T_i$ and $U_{\parallel e} = \frac{m_e}{m_i} V_{\parallel e} + \frac{\beta_e}{2} \psi$ the linear system is given by

$$\gamma \frac{n}{n_{00}} = + \frac{2}{B} C \left(T_e + \frac{T_{e00}}{n_{00}} n - \phi \right) + \frac{R}{L_n} \frac{\partial \phi}{\partial y} - \nabla_{\parallel} V_{\parallel e}, \quad (3.1)$$

$$\gamma \Omega = + 2B \left[C(T_e) + \frac{T_{e00}}{n_{00}} C(n) \right] + 2B\tau \left[C(T_i) + \frac{T_{i00}}{n_{00}} C(n) \right] + \frac{B^2}{T_{e00}} \nabla_{\parallel} j_{\parallel}, \quad (3.2)$$

$$\gamma U_{\parallel e} = - \nabla_{\parallel} \left(1.71 T_e - \frac{T_{e00}}{n_{00}} n \right) + \nabla_{\parallel} \phi + \nu j_{\parallel}, \quad (3.3)$$

$$\gamma V_{\parallel i} = - \nabla_{\parallel} (T_e + \tau T_i) - \frac{T_{e00} + \tau T_{i00}}{n_{00}} \nabla_{\parallel} n, \quad (3.4)$$

$$\gamma \frac{T_e}{T_{e00}} = + \frac{R}{L_{T_e}} \frac{\partial \phi}{\partial y} + \frac{4}{3B} C \left(\frac{7}{2} T_e + \frac{T_{e00}}{n_{00}} n - \phi \right) + \frac{2}{3} 0.71 \nabla_{\parallel} j_{\parallel} - \frac{2}{3} \nabla_{\parallel} V_{\parallel e}, \quad (3.5)$$

$$\gamma \frac{T_i}{T_{i00}} = + \frac{4}{3B} C \left(T_e + \frac{T_{e00}}{n_{00}} n - \phi \right) + \frac{R}{L_{T_i}} \frac{\partial \phi}{\partial y} - \frac{10\tau}{3B} C(T_i). \quad (3.6)$$

The main parameters characterizing the SOL in this linear drift-reduced model are L_n , the typical gradient scale length $\eta_{e,i} = \frac{L_n}{L_{T_{e,i}}}$, the ratio between density and temperature gradient length, together with the plasma β_e , parallel resistivity ν , magnetic shear \hat{s} , the tokamak major and minor radii R and a and the safety factor q . Despite the apparent simplicity of the model, it allows us to capture the most important properties of DW (Drift Waves) and BM (Ballooning Modes) (major instabilities described in section 3.2). It is important to note that modes other than the ones referred here could become unstable

in the edge and SOL regions of tokamak plasmas such as peeling-ballooning modes, external kinks and sheath modes ([40] and [41]) but, following past studies carried out with low-frequency non-linear electromagnetic models (both fluid and gyrofluid) in agreement with experimental results ([42], [43] and [44]), DW and BM typically determine the plasma turbulent dynamics in the SOL. These studies, however, do not clarify their relative importance.

In this chapter, we shall evaluate the relative importance of DW and BM for the geometry considered and how the different SOL operational parameters change the character of the turbulent modes. Following non-local, linear studies of BM and DW (see [45]), the scale length in the radial direction is larger than in the poloidal direction, i.e., $\frac{k_y}{k_r} \simeq \sqrt{k_y L_p} \gg 1$. Therefore, we ignore the radial mode dependence and assume $k_y \gg k_r$. Using a field line following approach, each perturbed quantity is Fourier decomposed in the y direction and z is the parallel coordinate with $0 < z < 2\pi$ (L_z is given by the distance between the poloidal limiters, i. e., one field line turn)

$$f_{k_y}(y, z, t) = f_{k_y}(z) e^{ik_y y + \gamma t}, \quad (3.7)$$

$$\nabla_{\parallel} f_{k_y}(y, z, t) = \frac{\partial f_{k_y}(z)}{\partial z} e^{ik_y y + \gamma t}. \quad (3.8)$$

The ∂_y operator is substituted by ik_y and the parallel derivative is calculated directly on the discretized parallel direction z with a finite difference scheme. Therefore, the curvature operator and the Laplacian operator become [39]

$$C = -2ik_y \left[\cos \frac{z}{q} + \frac{z}{q} \hat{s} \sin \frac{z}{q} \right], \quad (3.9)$$

$$\nabla_{\perp}^2 = -k_{\perp}^2 = -k_y^2 \left[1 + \left(\hat{s} \frac{z}{q} - \pi \hat{s} \right)^2 \right]. \quad (3.10)$$

This reduces our set of linear equations to a one-dimensional eigenvalue problem in the z direction for γ which is solved by the linear code. It discretizes $z = [0, L_z]$ with N_z points with a grid distance between each point $\Delta z \equiv z_{i+1} - z_i = \frac{L_z}{N_z - 1}$ and $z_i = (i - 1)\Delta y$ for the quantities n, ϕ, T_e and T_i . As in GBS, we compute a different grid for ψ and $V_{\parallel i}$ having $N_z - 1$ points with the same grid distance Δz and $y_z = (i - 1/2)\Delta y$. We denote the first as the unshifted grid and the last as the shifted grid. We refer the reader to [39] for a detailed description of the numerics.

Introducing the vector

$$\mathbf{x} = [n_1, \dots, n_{N_z}, \psi_1, \dots, \psi_{N_z-1}, V_{\parallel i,1}, \dots, V_{\parallel i,N_z-1}, T_{e,1}, \dots, T_{e,N_z}, T_{i,1}, \dots, T_{i,N_z}] \quad (3.11)$$

the resulting set of equations can be written as

$$L \frac{\partial}{\partial t} \mathbf{x} = M \mathbf{x}. \quad (3.12)$$

The eigenvalue problem is solved through an iterative solver that integrates the time evolution of (3.12) by discretizing it with a numerical scheme of the form

$$\frac{\mathbf{x}_{t+\Delta t} - \mathbf{x}_t}{\Delta t} = (1 - \Theta)L^{-1}M\mathbf{x}_t + \Theta L^{-1}M\mathbf{x}_{t+\Delta t}, \quad (3.13)$$

where $\Theta = 0$ leads to a fully explicit scheme, while $\Theta \neq 0$ leads to an implicit scheme. The growth rate is calculated by comparing the solution at two different time steps. In our work, we shall use $\Theta = 0.5$ (which is the only value that guarantees 2nd order accuracy).

It is important to derive the expression for the parallel derivative in terms of the poloidal and toroidal direction since we will be using it throughout the document. In Fig. 2.1 we can see that the magnetic field lines have a small ‘‘pitch’’ angle (that we shall call ϵ) that has the value

$$\epsilon = \arctan\left(\frac{a}{qR}\right), \quad (3.14)$$

due to the fact that after one turn of the field line, it moves a distance $\frac{2\pi a}{q}$ in the poloidal direction and $2\pi R$ in the toroidal direction, with $\frac{a}{qR}$ the slope of the straight lines of the magnetic field in the $\theta - \phi$ plane. Calling z_ϕ the toroidal direction, y the poloidal direction and z the parallel one, we can write

$$z_\phi = z \cos \epsilon, \quad y = z \sin \epsilon. \quad (3.15)$$

Using the chain rule, the parallel derivative can be written as

$$\nabla_{\parallel} = \frac{\partial}{\partial z} = \frac{\partial z_\phi}{\partial z} \frac{\partial}{\partial z_\phi} + \frac{\partial y}{\partial z} \frac{\partial}{\partial y} = \cos \epsilon \frac{\partial}{\partial z_\phi} + \sin \epsilon \frac{\partial}{\partial y}. \quad (3.16)$$

With simple geometrical arguments, and taking into account that we are in a large aspect ratio limit ($\epsilon \ll 1$), we can write

$$\cos \epsilon = \frac{R^2}{\sqrt{R^2 + \left(\frac{a}{q}\right)^2}} \simeq 1, \quad (3.17)$$

$$\sin \epsilon = \frac{a/q}{\sqrt{R^2 + \left(\frac{a}{q}\right)^2}} \simeq \frac{a}{qR}. \quad (3.18)$$

$$(3.19)$$

Therefore, we can write

$$\partial_z = \frac{a}{qR} \partial_y + \partial_{z_\phi}. \quad (3.20)$$

3.2 Linear SOL Instabilities

A number of instabilities are described by the system of Eqs. (3.1) - (3.6). We shall focus on the DW and BM, whose linear properties have been extensively studied (see for example [43], [46], [42] and [47]).

3.2.1 Drift Waves

DW arise primarily due to the $\mathbf{E} \times \mathbf{B}$ convection of the density profile [6]. A basic example can be seen through the electron/ion continuity equation (2.36) retaining only the term $\mathbf{v} = \mathbf{v}_{E \times B} = \frac{c}{B} \partial_y \phi \mathbf{e}_x$ and assuming quasi-neutrality with $n = n_0 + \tilde{n}$

$$\begin{aligned} \frac{\partial n}{\partial t} &= -\mathbf{v}_{E \times B} \cdot \nabla n_0 = -v_{de} n_0 \frac{\partial e\phi}{\partial y T_e} = -v_{di} n_0 \frac{\partial e\phi}{\partial y T_i}, \\ v_{de,i} &= \frac{c T_{e,i}}{eB} \frac{1}{L_n}, \quad L_n \equiv \frac{n}{\partial_x n}. \end{aligned} \quad (3.21)$$

In the isothermal limit we have in first order the Boltzmann relation

$$0 = -\nabla P_{e,i} - n_0 e \nabla E \Leftrightarrow \frac{\tilde{n}}{n_0} = \frac{e\phi}{T_{e,i}}, \quad (3.22)$$

which combined with (3.24) yields

$$\frac{\partial \tilde{n}}{\partial t} = -v_{de,i} \frac{\partial \tilde{n}}{\partial y}, \quad (3.23)$$

which is a wave propagating perpendicular to the magnetic field and to the density gradient (which is called the electron/ion diamagnetic drift direction).

We now turn to the drift wave instability. Within the linear model described in (3.1) - (3.6), we linearize the perpendicular gradients, neglect the curvature (ballooning) terms and the coupling with sound waves by considering $k_{\parallel} \ll \gamma$ (therefore neglecting $V_{\parallel i}$ dynamics). This yields the DW model [39]

$$\gamma n = ik_y \frac{R}{L_n} \phi - k_{\perp}^2 \nabla_{\parallel} \psi, \quad (3.24)$$

$$-k_{\perp}^2 \gamma \phi = -k_{\perp}^2 \nabla_{\parallel} \psi, \quad (3.25)$$

$$\gamma \psi \frac{\beta}{2} + \frac{m_e}{m_i} \gamma k_{\perp}^2 \psi = k_{\perp}^2 \nu \psi + \nabla_{\parallel} (\phi - n - 1.71 T_e) + ik_{\perp} (1 + 1.71 \eta_e) \frac{\beta}{2} \frac{R}{L_n} \psi, \quad (3.26)$$

$$\gamma T_e = ik_y \eta_e \frac{R}{L_n} \phi - k_{\perp}^2 \frac{2}{3} 1.71 \nabla_{\parallel} \psi. \quad (3.27)$$

We consider the two branches of the drift wave instability in the cold ion limit: the resistive and the inertial one. The resistive branch of DW (Resistive Drift Wave (RDW)) is characterized by the presence of finite resistivity which brakes the adiabaticity. It is obtained from (3.24)-(3.27) by neglecting electron

inertia ($\frac{m_e}{m_i} \rightarrow 0$) and electromagnetic effects ($\beta \rightarrow 0$). In the inertial branch (Inertial Drift Wave (InDW)) the adiabaticity is broken by the presence of finite electron mass, being retrieved from (3.24)-(3.27) by neglecting resistivity ($\nu \rightarrow 0$) and electromagnetic effects [39].

The one dimensional resulting equation for each branch is given by (3.28) with the substitutions bellow. We substitute \tilde{z} by $\bar{z} = z\sqrt{\nu R/L_n}$, $\bar{\gamma} = \gamma L_n/R$, $k_{\perp}^2 = k_y^2 [1 + (\bar{z}\alpha_R\hat{s})^2]$ and $\alpha_R = \sqrt{L_n}/(q\sqrt{\nu R})$ for RDW and \tilde{z} by $\hat{z} = zR\sqrt{m_e}/(L_n\sqrt{m_i})$, $k_{\perp}^2 = k_y^2 [1 + (\hat{z}\alpha_I\hat{s})^2]$ and $\alpha_I = L_n\sqrt{m_i}/(qR\sqrt{m_e})$ for InDW.

$$\bar{\gamma}k_{\perp}^2\phi = \left(1 - ik_y\frac{1 + 1.71\eta_e}{\bar{\gamma}}\right)\frac{\partial^2\phi}{\partial\bar{z}^2} + 2.94\frac{\partial^2(k_{\perp}^2\phi)}{\partial\bar{z}^2}. \quad (3.28)$$

3.2.2 Ballooning Modes

BMs are curvature driven modes which together with DW are perceived to be the most important drives of plasma turbulence in the SOL region. As in the previous section, we can analyze a simple case to gain some insight on the basic physical mechanism. Decomposing the diamagnetic drifts defined in (2.31) and approximating $\nabla \times \frac{\mathbf{b}}{B} \simeq \frac{2}{B}\mathbf{b} \times \boldsymbol{\kappa}$ which holds for $\nabla \times \mathbf{B} = 0$ at negligible local current density, we find

$$\mathbf{v}_{di} = -2\frac{cT_i}{eB}\mathbf{b} \times \boldsymbol{\kappa} - \frac{c}{en}\nabla \times \frac{p_i\mathbf{b}}{B}, \quad (3.29)$$

$$\mathbf{v}_{de} = +2\frac{cT_e}{eB}\mathbf{b} \times \boldsymbol{\kappa} + \frac{c}{en}\nabla \times \frac{p_e\mathbf{b}}{B}. \quad (3.30)$$

The term $\pm\frac{c}{en}\nabla \times \frac{p_{e,i}\mathbf{b}}{B}$ describes a gyro motion of the particles which does not displace the guiding center, being therefore irrelevant to the final equations [6]. Particularly, it appears only in the form $\nabla \cdot n\mathbf{v}_{de,i}$, which does not contribute. The terms (3.29) and (3.30) are the sum of the gradient B drift and the centrifugal drift, leading to particle motion perpendicular to the magnetic field and to the field line curvature $\boldsymbol{\kappa}$. With different signs, ions and electrons drift into opposite directions creating an electric field and a space charge (see Fig. 3.1).

At the high-field side (poloidal angle where B is stronger), ∇n and $\boldsymbol{\kappa}$ point into opposite directions leading to a stable configuration. At the low-field side, the magnetic drift shifts the ions upwards and the electrons downwards, where a density gradient in the direction parallel to the particle motion causes a charge separation and a consequent electric field. This field leads to an $\mathbf{E} \times \mathbf{B}$ drift, amplifying the initial perturbation and therefore completing the instability mechanism. Essentially, the instability must be localized within the unfavourable curvature region (ballooning mode) or the curvature must be destabilizing on average (interchange mode).

As ballooning modes are driven by an interchange character and the presence of a magnetic field line curvature and plasma pressure gradients, we neglect the coupling with sound waves, plasma compressibility, parallel flows in the density and temperature equations and the $\nabla_{\parallel}(n + 1.71T_e)$ term in Ohm's law, yielding the system (3.31)-(3.34).

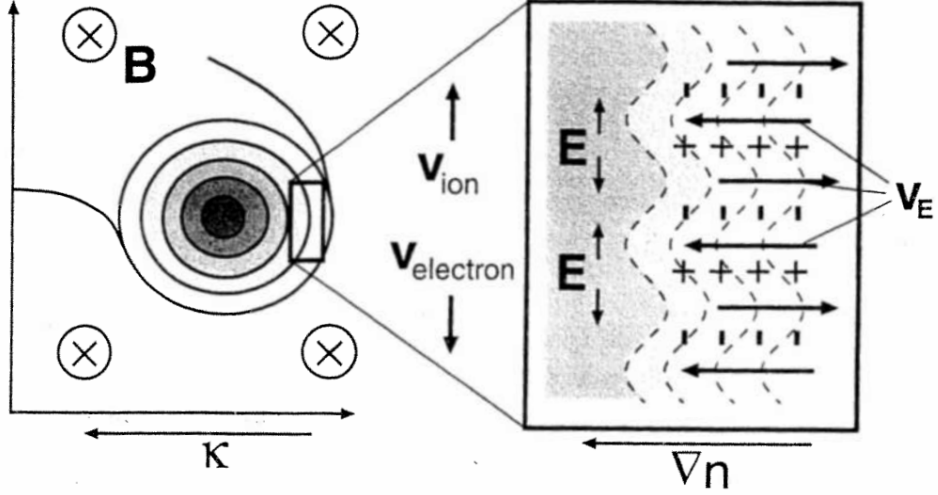


Figure 3.1: Rosenbluth-Longmire picture of curvature driven instabilities with an initial perturbation of the density profile at the low-field side of the torus. The curvature drift shifts electrons and ions into opposite directions and the resulting space charge generates an electric field leading to an $\mathbf{E} \times \mathbf{B}$ drift that amplifies the initial perturbation (figure taken from [6]).

$$\gamma n = ik_y \frac{R}{L_n} \phi, \quad (3.31)$$

$$-k_{\perp}^2 \gamma \phi = 2C(n + T_e) - k_{\perp}^2 \nabla_{\parallel} \psi, \quad (3.32)$$

$$\gamma \psi \frac{\beta}{2} + \frac{m_e}{m_i} \gamma k_{\perp}^2 \psi = -k_{\perp}^2 \nu \psi + \nabla_{\parallel} \phi + ik_{\perp} (1 + 1.71\eta_e) \frac{\beta}{2} \frac{R}{L_n} \psi, \quad (3.33)$$

$$\gamma T_e = ik_y \eta_e \frac{R}{L_n} \phi. \quad (3.34)$$

Here, we consider the 3 branches associated with BM: the resistive branch (Resistive Ballooning Mode (RBM)) is retrieved from Eqs. (3.31)-(3.34) by neglecting electron inertia and electromagnetic effects, the inertial one (Inertial Ballooning Mode (InBM)) by neglecting resistivity and electromagnetic effects and the ideal (Ideal Ballooning Mode (IdBM)) neglecting electron inertia and resistivity.

The one dimensional resulting equation for each branch is given by (3.35) for RBM, (3.36) for InBM and (3.37) for IdBM. It was found in [39] that the maximum growth rate for all cases is $\gamma_B^{\max} = \sqrt{2R/L_p}$, where it was also performed an intensive study on the parameter space of the linear instabilities of the drift-reduced Braginskii equations. In (3.35) we substitute $\bar{z} = z/q$, $\bar{\gamma} = \gamma/\gamma_B^{\max}$ and $\sigma_R = 1/(\gamma_B^{\max} k_y^2 q^2 \nu)$, in (3.36) $\sigma_{In} = \sqrt{m_i}/(\gamma_B^{\max} k_y q \sqrt{m_e})$ and in (3.37) $\alpha_{MHD} = -q^2 \beta (1 + \eta_e) R/L_n$.

$$\bar{\gamma} \phi [1 + (\bar{z}\hat{s})^2] = \sigma_R \frac{\partial^2 \phi}{\partial \bar{z}^2} + \frac{C}{\bar{\gamma}} \phi, \quad (3.35)$$

$$\bar{\gamma} \phi [1 + (\bar{z}\hat{s})^2] = \frac{\sigma_{In}^2}{\bar{\gamma}} \frac{\partial^2 \phi}{\partial \bar{z}^2} + \frac{C}{\bar{\gamma}} \phi, \quad (3.36)$$

$$\bar{\gamma}\phi [1 + (\bar{z}\hat{s})^2] = \frac{1 + (\bar{z}\hat{s})^2}{\alpha_{MHD}\bar{\gamma}} \frac{\partial^2\phi}{\partial\bar{z}^2} + \frac{C}{\bar{\gamma}}\phi. \quad (3.37)$$

3.3 Linear Instability Analysis

We now study the relative importance of each instability branch described in Chap. 3: RBM, InBM, RDW and InDW. As these simulations are computationally cheap (compared with the non-linear ones), we can perform a scan in each input parameter and determine its growth linear rate and typical pressure gradient length.

Each instability branch provides a different estimate for L_p . The BM branches provide the ballooning character seen before of $L_p(\text{LFS}) > L_p(\text{HFS})$, while the DW branches provide a constant L_p through all poloidal angles. This can be seen quantitatively in Fig. 3.2, where the estimates were performed with ISTTOK-like parameters. We see that the branches that generate the greatest value of L_p are InBM at the LFS and InDW at the HFS. Performing a scan in q, ν, \hat{s}, τ and β_e we shall determine if this constitutes a trend and therefore the turbulence is characteristic of the geometry itself or if the parameters change the fundamental properties of the fluctuations and equilibrium of the plasma profile. The introduction of a finite β_e also leads to the appearance of the Ideal Ballooning Mode (see Chap. 3), whose importance will be assessed.

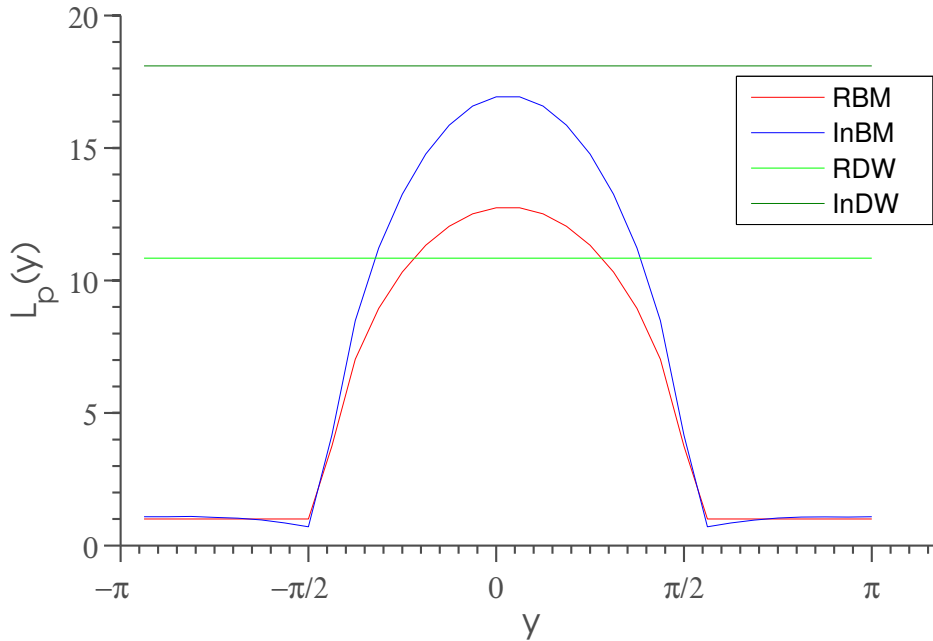


Figure 3.2: Poloidal variation of L_p for the 4 instability branches provided by the gradient removal hypothesis for ISTTOK-like parameters.

For the scan analysis we shall look at the growth rate itself, running the linear solver after the determination of L_p with the gradient removal hypothesis, so we can follow previous linear studies in the SOL (such as [39]). It has been seen in [39] that magnetic shear can play a major role in the determination of the growth rate of each instability branch. Since this parameter was not present in the non-linear

simulations, we present for each growth rate a scan in \hat{s} and a scan in the poloidal variable y such as for the L_p analysis, so each y and \hat{s} we determine which branch provides the greatest growth rate γ .

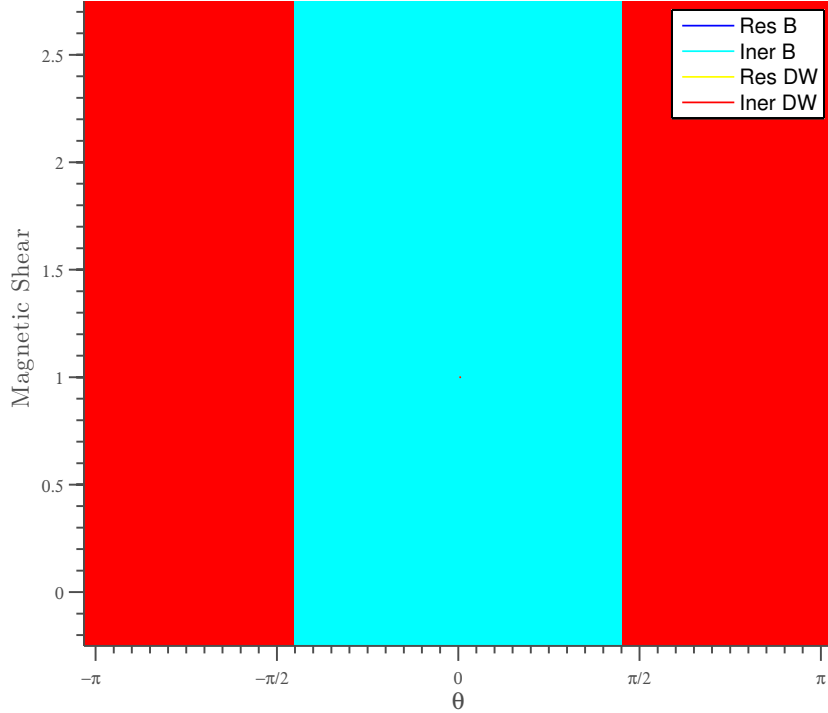


Figure 3.3: Representation of the branch that provides the greatest linear growth rate as a function of the poloidal angle and magnetic shear for the same input parameters inserted in the non-linear simulations.

In Fig. 3.3 we perform this analysis for the ISTTOK-like parameters used in the non-linear simulations. This shows the predominance of the InBM at the LFS region and the InDW at the HFS with no variation as the magnetic shear increases from 0 to 2.5. From Fig. 3.4 we see that, except for values of $\nu < 10^{-3}$, the instability branches that are predicted to play a major role at ISTTOK's SOL remain the same through a scan in τ , q , ν and β_e . It is determined that as τ increases, there is an extension of the InDW region, while for different β_e and q the results stay the same. As ν drops to a value closer to m_e/m_i , the RBM starts to play a role but only in a very small region, negligible for all values of \hat{s} except $\hat{s} = 1.5$. It was also seen that the absolute value of L_p and γ does not alter significantly with \hat{s} . For the case of $\nu < 10^{-3}$, the RBM starts to dominate at the LFS. This shows a strong dependence on this parameter, as even for slight changes on ν the dominant instabilities are different. A non-linear simulation with lower values of resistivity is needed in order to fully assess its influence.

Following [39], the parameter that describes the damping of the mode due to the resistive parallel spread (relevant in the RBM) is σ_R (3.38) and the one that describes the damping due to the inertial spread is σ_{In} (3.38). It is also shown that the growth rate increases as σ_R and σ_{In} decreases. If we look at the ratio $\sigma_R/\sigma_{In} = \sqrt{m_e/m_i}/(\nu k_y)$ for ISTTOK (using the typical value of $k_y = 0.2$ obtained from GBS) we get the value $\sigma_R/\sigma_{In} \simeq 100$ which points to the dominance of the inertial branch (the same analysis may be applied to the drift wave resistive and inertial branch). Note that in ISTTOK $\nu_{ISTTOK} > m_e/m_i$.

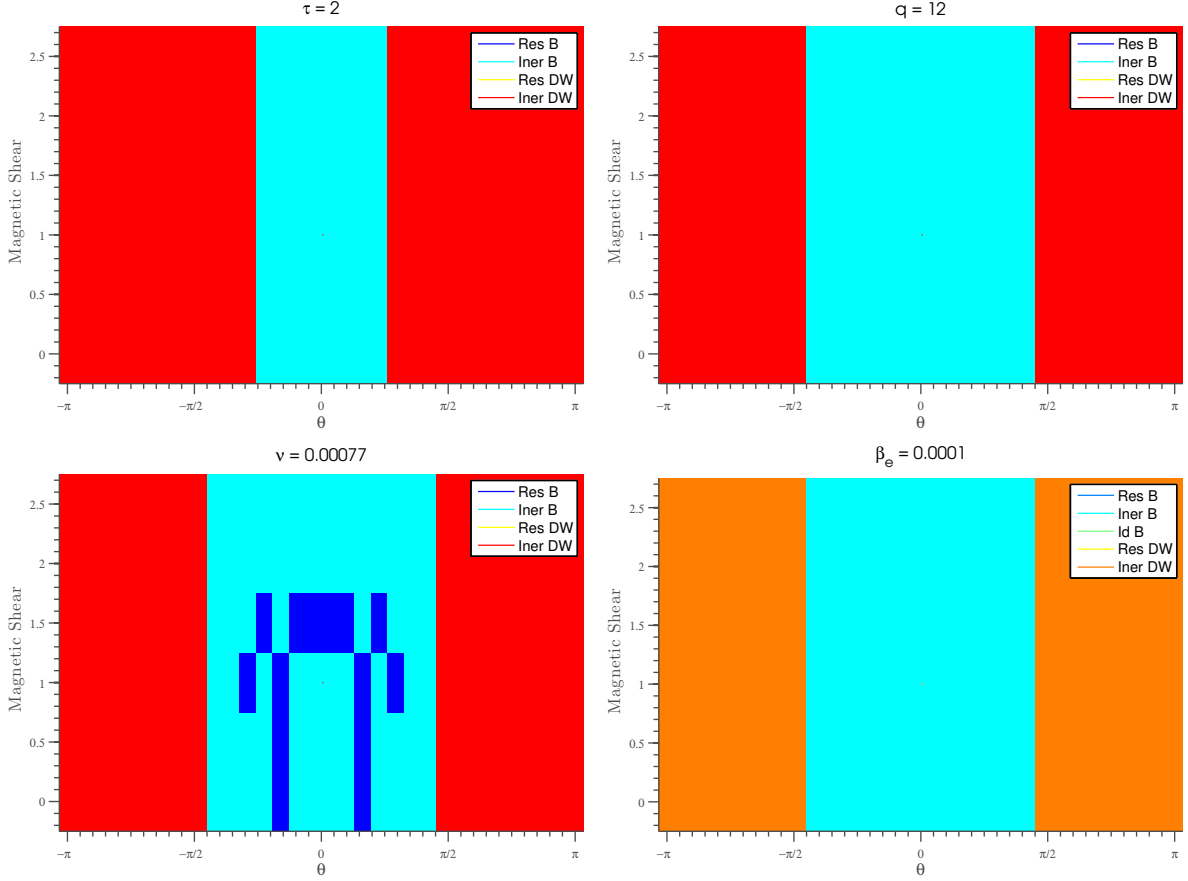


Figure 3.4: Each figure shows which branch provides the greatest linear growth rate as a function of the poloidal angle and magnetic shear. With a scan on each variable τ , q , ν and β_e the inertial DW and BM are the major predicted branches at play at ISTTOK's SOL.

$$\sigma_R = \sqrt{\frac{L_p}{2R}} \frac{1}{k_y^2 \nu}, \quad \sigma_{In} = \sqrt{\frac{L_p m_i}{2R m_e}} \frac{1}{k_y} \quad (3.38)$$

3.4 Gradient Removal Mechanism

There are several mechanisms that have been proposed to explain the saturation of linear modes during the non-linear phase ([48], [49], [47]). In [32], it has been shown that the growth of the Kelvin-Helmholtz instability and the *gradient removal mechanism* play a major role in the SOL through the analysis of the drift-reduced Braginskii equations (as done in this thesis). The latter dictates that the saturation of the linear mode is due to the non-linear flattening of the driving plasma gradients. Analytical estimates and numerical simulations [32] show that the gradient removal saturation mechanism is the one at play in the SOL when $\sqrt{k_y L_p} < 3$ (the KH-stable parameter regime). This mechanism provides an estimation of L_p as a function of the SOL operational parameters that has a quantitative good agreement with simulation and experimental results [35].

It is useful to briefly derive this model starting from the GBS equations, namely the continuity and electron temperature eqs. (2.60) and (2.64). Ignoring the curvature and diffusion terms (which are small compared to the $\mathbf{E} \times \mathbf{B}$ convection and parallel terms) in the SOL we have

$$\frac{\partial p}{\partial t} = -R[\phi, p] - \frac{\partial(pV_{||e})}{\partial z}, \quad (3.39)$$

$$[\phi, p] = \nabla \cdot \Gamma, \quad \Gamma = p \left(\frac{\partial \phi}{\partial y} \mathbf{e}_x - \frac{\partial \phi}{\partial x} \mathbf{e}_y \right), \quad (3.40)$$

where Γ is the adimensionalized pressure flux. Eq. (3.40) can be time averaged during the quasi-steady state phase (dropping times of order $\leq 1/\omega$ where ω is the characteristic turbulence frequency) and along the toroidal and poloidal directions. All quantities are written as $f = \bar{f} + \tilde{f}$, with \bar{f} the averaged and \tilde{f} the fluctuating component. After time and toroidal averaging we obtain

$$\frac{\partial \bar{\Gamma}_x}{\partial x} + \frac{\bar{\Gamma}_y}{2\pi a} \Big|_{\text{limiter}} = - \frac{\overline{pV_{||e}}}{2\pi R} \Big|_{\text{limiter}}, \quad (3.41)$$

where $\bar{\Gamma}_y|_{\text{limiter}}$ and $\overline{pV_{||e}}|_{\text{limiter}}$ are the pressure flux in the poloidal direction and the parallel losses averaged over time and in the toroidal direction, evaluated at the limiter plates. Estimating $\overline{pV_{||e}} \simeq \bar{p}\bar{c}_s$ and neglecting $\Gamma_y \ll \Gamma_x$ (since the characteristic lengths in the x direction are much shorter than in y) we obtain

$$\frac{\partial \bar{\Gamma}_x}{\partial x} \simeq - \frac{\bar{p}\bar{c}_s}{2\pi R} \implies \frac{\bar{\Gamma}_x}{L_p} \approx \frac{\bar{p}\bar{c}_s}{R}. \quad (3.42)$$

This is the balance between the radial flux and the parallel losses, where $L_p = \bar{\Gamma}_x / \frac{\partial \bar{\Gamma}_x}{\partial x}$. Splitting the averaged component and the turbulent part as $\bar{\Gamma}_x = \bar{p} \frac{\partial \bar{\phi}}{\partial y} + \tilde{p} \frac{\partial \tilde{\phi}}{\partial y}$, we can neglect the averaged component approximating the radial flux as

$$\bar{\Gamma}_x \simeq \tilde{p} \frac{\partial \tilde{\phi}}{\partial y} \simeq k_y \tilde{\phi} \tilde{p}, \quad (3.43)$$

with k_y the typical wavelength of the mode. Turbulent saturation of the linearly unstable modes is achieved when the radial gradient of the perturbed pressure becomes comparable to the radial gradient of the background pressure

$$\frac{d\tilde{p}}{dx} \approx \frac{d\bar{p}}{dx}, \quad (3.44)$$

which can also be written as $k_x \tilde{p} \approx \frac{\bar{p}}{L_p}$, where k_x is the typical radial wave number of the instability. With this estimation, we can write

$$\frac{\tilde{p}}{\bar{p}} \approx \frac{1}{L_p k_x}. \quad (3.45)$$

From the leading term in the pressure equation $\partial_t p \sim R[\phi, p]$, we derive $\gamma \tilde{p} \approx R \bar{p} k_y \tilde{\phi} / L_p$ which translates to

$$\tilde{\phi} \approx \frac{\tilde{p}}{\bar{p}} \frac{L_p}{R} \frac{\gamma}{k_y}. \quad (3.46)$$

Following non-local linear theory as outlined in [50] and [45], for DW and BM we estimate k_x as

$$k_x \approx \sqrt{\frac{k_y}{L_p}}. \quad (3.47)$$

Plugging (3.45), (3.46) and (3.47) in (3.42) and (3.43), and using $\bar{c}_s = c_{s0} = 1$ in normalized units, an estimate for L_p is obtained

$$L_p \approx \frac{\gamma}{k_y}, \quad (3.48)$$

which for a non-normalized units yields $L_p \approx \frac{R}{c_s} \frac{\gamma}{k_y}$. The linear code provides the growth rate γ for a given value of k_y and, through a set of values (γ_i, k_{yi}) , we seek the value that yields largest transport choosing the maximum of the ratio γ/k_y [51]. As L_p also depends on the different SOL operational parameters, we obtain a value of L_p that satisfies Eq. (3.48) through Muller's method [52] maintaining all other parameters fixed (see algorithm in appendix B). As in [32], the gradient removal hypothesis assumes the inequality $\sqrt{k_y L_p} < 3$ (the KH stable regime) which will be tested throughout the non-linear and linear simulations. We point that this is a "quasi-linear" model, where we have estimated the size of the non-linearity and included it in the calculation.

3.5 Non-Linear Analysis Techniques

3.5.1 L_p Variation

With the definition $L_p \equiv |\frac{\partial_x p}{p}|$, after averaging over y and z , we seek the decay-like behavior

$$p(x) = p_0 e^{-\frac{x}{L_p}}. \quad (3.49)$$

Within ISTTOK's geometry, the presence of a poloidal limiter implies not only a poloidal symmetry in our system but that the HFS is located at the poloidal location $\theta = 0$ and the LFS at $\theta = \pi$. As the plasma is better confined in the HFS it should in principle drive little turbulence across the magnetic field lines and the reverse is true for the LFS. As L_p is a measure of this transport across the magnetic field lines, it should increase in the LFS and decrease at the HFS while being poloidally periodic (which in turn provides a "Gaussian-like" figure for $L_p(y)$).

These arguments leads us to pursue a ballooning character in the LFS where $L_p(\pi)$ is greater than $L_p(0) = L_p(2\pi)$ in the HFS where we expect a drift-wave character with a much smaller radial variation.

This analysis on L_p is divided in three tests - first obtain an absolute estimate for L_p through a toroidal and poloidal averaging, then estimate the poloidal variation of this value and hence obtaining $L_p(y)$ and finally estimate the toroidal variation and obtain $L_p(z)$ at the HFS and LFS.

First, to test the hypothesis in (3.49) we position ourselves in the SOL region choosing a radial domain between the plasma source from the core and the wall, perform a fit in the radial direction of the toroidal and poloidal average of the plasma pressure (which also applies for L_n and L_T) to the expression (3.49). We then look at the variation of $L_p(y)$ performing a fit at each poloidal location of the toroidal average of

the plasma pressure. Finally we perform a fit for each toroidal direction but looking poloidally at the HFS and LFS (i.e. $L_p(z, y = 0)$ and $L_p(z, y = \pi)$).

These results are then compared with the L_p obtained from the linear code together with the gradient removal estimate (which in GBS units reads $L_p \simeq \frac{\gamma}{k_y}$) and the experimental value.

3.5.2 Cross-Coherence

We apply a ‘‘cross-coherence’’ technique which asserts the DW character of the domain of interest. Since in this case electrons are close to adiabaticity, the amplitudes of ϕ and n are correlated. To see this, we look to the linear Ohm’s law in the isothermal limit

$$\gamma \left(\frac{m_e}{m_i} V_{\parallel e} + \frac{\beta_e}{2} \psi \right) - \nu j_{\parallel} = \nabla_{\parallel} \left(\phi - \frac{T_{e00}}{n_{00}} n \right). \quad (3.50)$$

In this case, the adiabatic braking terms have the parameters β_e , ν and $\frac{m_e}{m_i}$, which in the HFS are small comparing with the RHS of (3.50), where the parallel gradients become dominant. Therefore, we can estimate that $\phi \simeq \frac{T_{e00}}{n_{00}} n + \text{constant}$ and should obtain a clearly correlated plot of $\phi(n)$.

At a fixed radial location and at a half distance in the toroidal direction the ϕ and n fluctuations are normalized to their standard deviation. We then evaluate the probability of finding both fluctuations at a certain ordered pair of amplitudes.

3.5.3 Phase Shift

To assert the BM character, we look at the phase shift $-\pi \leq \delta < \pi$ between ϕ and n fluctuations. The value of δ can be estimated through the linear vorticity equation for cold ions. Neglecting the parallel derivative of the parallel current (which represents the coupling with DW) we obtain

$$\gamma \nabla_{\perp}^2 \phi = 2B \frac{T_{e00}}{n_{00}} C(n). \quad (3.51)$$

Therefore in the case of BM the ϕ and n fluctuations are not correlated but retain a phase shift of $\delta = \frac{\pi}{2}$ (as $C(f) \propto \partial_y f$). The value of δ is calculated at a fixed radial and toroidal position and choosing a small domain at the HFS and other at the LFS, we perform an Fast Fourier Transform (FFT) along y on those fluctuations. From the FFT we compute the phase shift corresponding to each k_y and we bin them as a function of wavenumber on both domains, with the proper weight given by the power spectral density of ϕ and n fluctuations.

3.5.4 Power Spectrum

Experimentally, the different modes discussed in this section have been observed on ISTTOK ([1] and [21]). The HFS and LFS separation has been measured in detail and can be compared with the non-linear and linear results. One of the experimental diagnostics is the frequency spectrum of the floating potential V_f , a measured quantity by ISTTOK’s diagnostics [1]

$$V_f = V - 3T_e. \quad (3.52)$$

As typically observed in the boundary plasma of fusion devices [53], it is found on ISTTOK (Fig. 3.5) that the lowest frequency part of the spectrum ($f < 30 - 50$ kHz) is nearly independent of the frequency and the high frequency part ($f > 80 - 100$ kHz) shows a power-like decay with indices close to -2 both at LFS and HFS. The transition region shows a slope of -1 . We can then compare the power indices and the overall behavior $\text{FFT}(V_f(\text{HFS})) < \text{FFT}(V_f(\text{LFS}))$ at the high-frequency with the GBS simulation results.

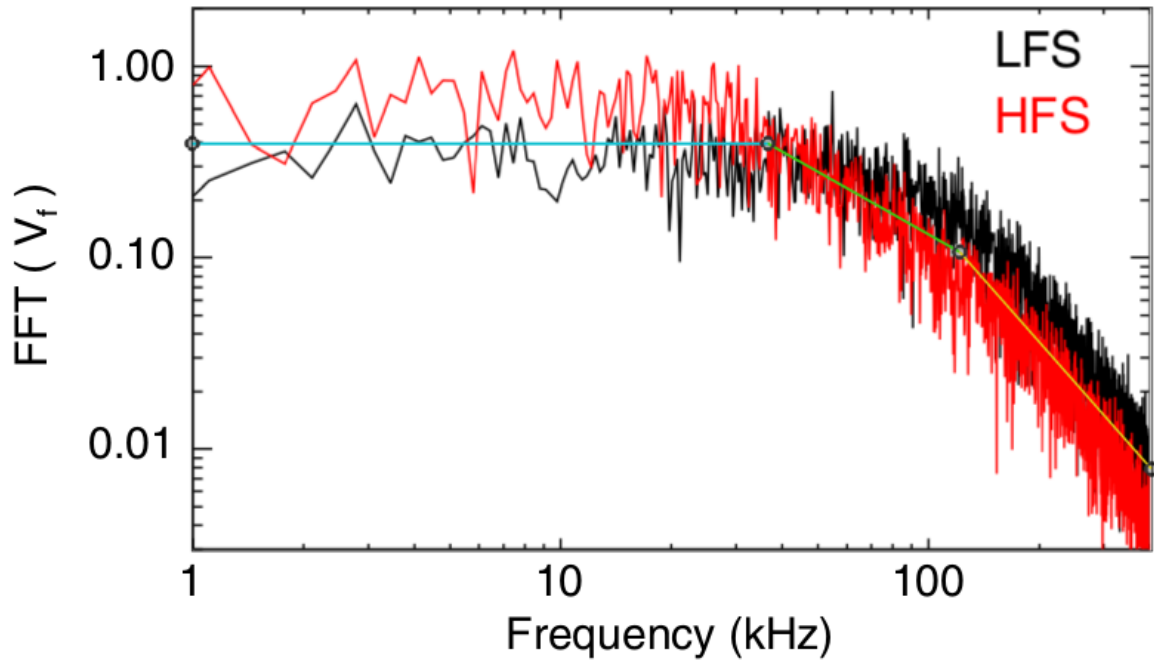


Figure 3.5: Experimental power-spectrum results performed at ISTTOK (figure taken from [1]). The blue line represents the first low-frequency region, the green line the transition region with a slope of -1 and the yellow one the high frequency region with a slope of -2 .

Simulation Results and Analysis

In this chapter we shall present the results of the non-linear simulations of SOL turbulence using the GBS code described in Chap. 2, for which typical simulations can be found in [24]. We present the results that support our methodology to determine the SOL turbulent regimes and compare with the linear code results, which determines the relative importance of the four predicted instability regimes: RBM, InBM, IdBM, RDW and InDW described in Chap. 3. Finally, we perform a comparison between simulation and experiment results.

Within the non-linear simulations, we seek which turbulent regimes play the major role at the LFS and HFS comparing the phase shift and cross-correlation between ϕ and n fluctuations, obtaining the poloidal variation of L_p in order to compare with the gradient removal hypothesis and estimate η_e from GBS simulations and experimental results. The simulations were performed with ISTTOK-like parameters and with no DW and BM coupling.

4.1 GBS Snapshots and Analysis

Comparing the SOL parameters that determine the different instability branches in ISTTOK, β has a value of $\simeq 10^{-5}$, whereas $\nu \simeq 10^{-3}$ and $m_e/m_i \simeq 5 \times 10^{-4}$. The small influence of β and \hat{s} (magnetic shear) is confirmed with the linear code in the next sections. For this reason, GBS simulations were performed using ISTTOK-like parameters without electromagnetic effects and without magnetic shear. The simulations are performed with the typical ISTTOK's edge value of $q = 8$ for cold and hot ions, containing $(N_x = 64, N_y = 512, N_z = 32)$ grid points in the (x, y, z) directions. The plasma and heat source are located at $x = 15$ with $\sigma_s = 2.5$. Further input parameters are provided in table 2.1. For a typical simulation, we use 32 cores through the course of 1 week reaching $\simeq 1000$ GBS time units (approximately 5000 CPU hours).

In Fig. 4.1 we represent a typical time trace of one point of the electric potential ϕ/ϕ_0 at a fixed location (the typical steady state duration at ISTTOK varies from 1 to several ms). There are differences on the absolute value of ϕ at different locations, specially when comparing the LFS with the HFS, but the temporal variation does not alter significantly.

In Fig. 4.2 we represent a typical density snapshot for cold ions in a poloidal plane (as a function of x

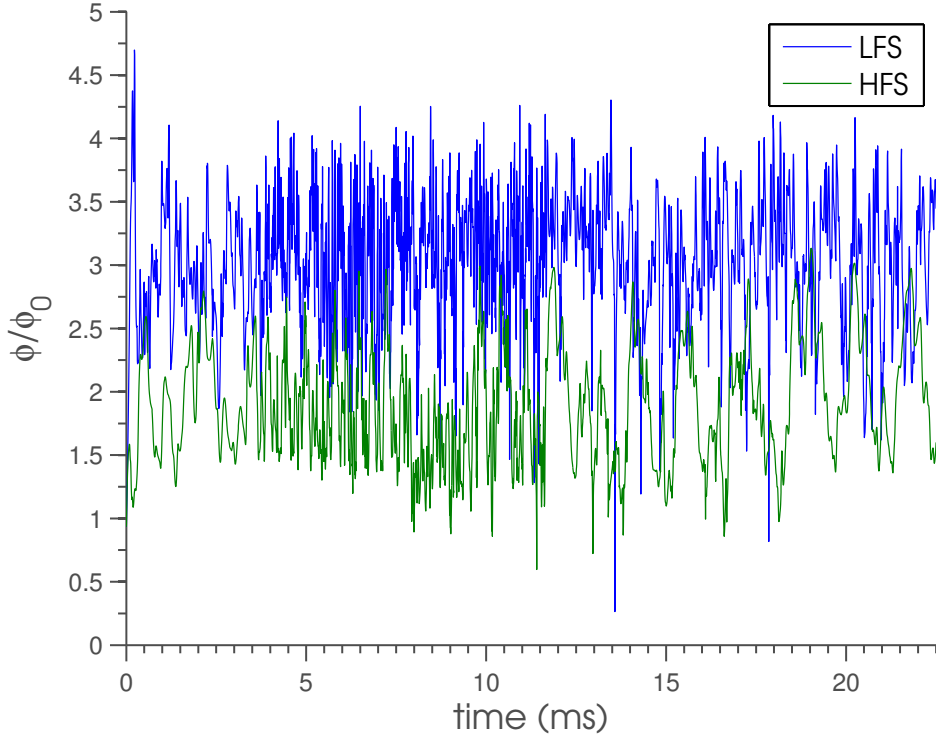


Figure 4.1: Time trace of the electric potential from the beginning of the simulation with cold ions to a quasi-steady state at a fixed location of the HFS $(x, y, z) = (20, 1, 16)$, and LFS $(x, y, z) = (20, 256, 16)$. The typical duration of the quasi-steady state phase at ISTTOK varies from 1 to several ms.

and y) at halfway between the limiter ($z = \frac{L_z}{2}$) in a turbulent state and the same quantity averaged over the quasi-steady period (same time period as in Fig. 4.1). The ring shown starts at the radial position of the source and ends at the wall. There is an observed radial fall-off that depends on y , namely that $L_p(\text{LFS}) > L_p(\text{HFS})$. These statements will be quantified in section 4.2.

In Fig. 4.3 we look at the ion and electron parallel velocities in the toroidal plane (as a function of y and z) for a cold ion simulation. Since electrons possess small inertia, the averaging is not as clear as in the ion parallel velocity, where we see that ions start at $z = 0$ with velocity equal to $-c_{s0}$ (-1 in our normalization) and end at $z = 2\pi$ with c_{s0} . This region represents the limiter and the value is consistent with the Bohm sheath condition, where it expresses a limiter value of $\pm c_{s0} e^{\Lambda - \frac{\phi}{T_e}}$ in Eq. (2.77). This is why the electron velocity has limiting values beyond 1 and -1 at the boundaries (it also has a dependence on ϕ and T_e).

Simulations were also performed with no DW coupling, where we neglect the diamagnetic term in Ohm's law ($\nabla_{\parallel}(n + 1.71T_e)$), and with no BM coupling, where the interchange terms in the vorticity equation are turned off. In Fig. 4.4 we see these two simulation results, averaging the density profile over the simulation period. We note that turning off the interchange drive the ballooning character observed before (where $L_p(\text{LFS}) > L_p(\text{HFS})$) is lost.

Simulations with a different value of $q = 4, 6, 10, 12$ and with $\tau = 1, 2$ were also performed with no fundamental difference in the results detailed in this chapter.

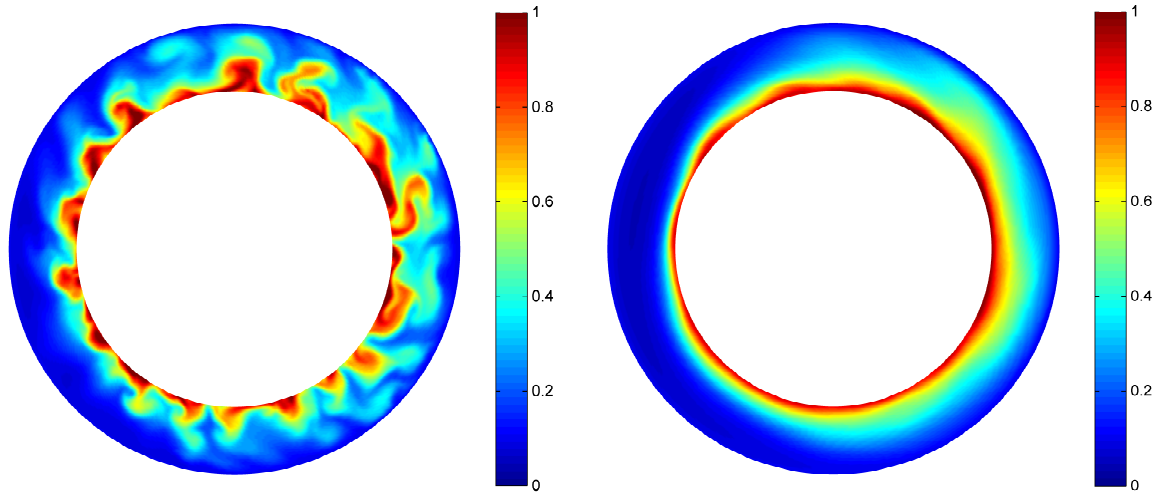


Figure 4.2: Typical snapshot of GBS simulations at a poloidal plane halfway between the limiter. ($z = N_z/2$) Plots show contours of density at a specific time slice - 20 ms (left) and averaged over the steady-state period - between 20 and 22.5 ms (right).

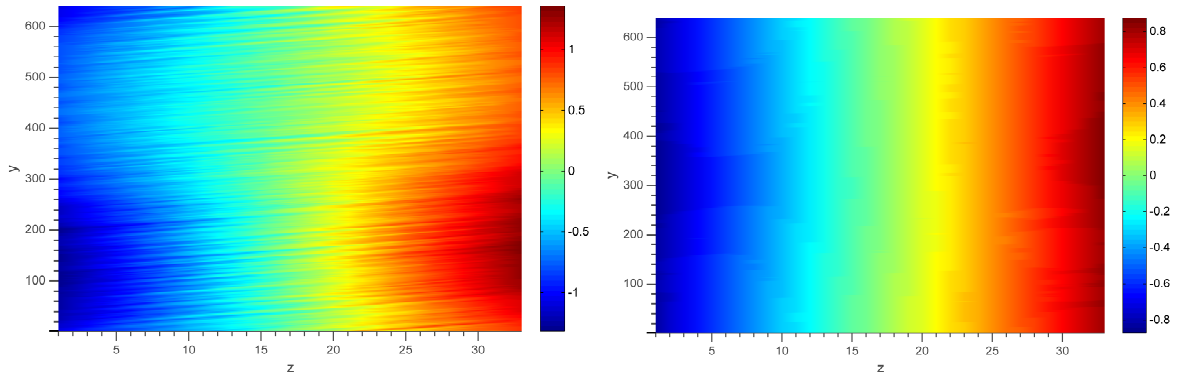


Figure 4.3: Typical snapshot of GBS simulations at a toroidal plane at $x = 20$ (out of 64 x grid points). Plots show contours of electron (left) and ion (right) parallel velocity averaged over the steady-state period - between 20 and 22.5 ms.

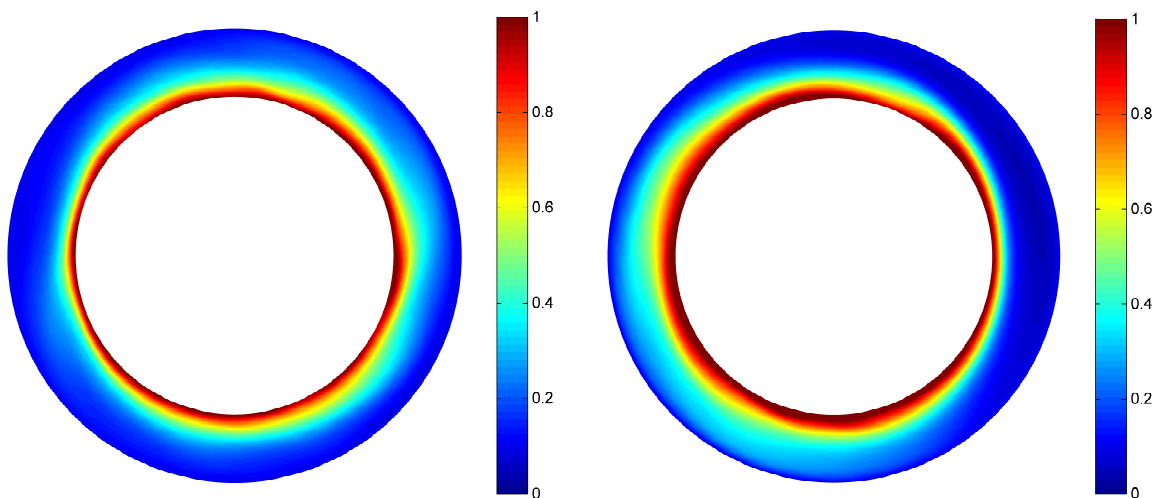


Figure 4.4: Snapshot of GBS simulations with no DW (left) and no BM (right) coupling at a poloidal plane halfway between the limiter. Plots show contours of density averaged over the steady-state period - between 20 and 22.5 ms.

4.2 Typical Pressure Gradient Length

In order to test the dependence

$$p(x) = p_0 e^{-x/L_p}, \quad (4.1)$$

we average the total pressure over y and z and plot the resulting profile in Fig. 4.5. We identify the exponential decay character right after the source at $x = 15$ until approximately $x = 50$. This will be the domain where the L_p test will be performed (red dashed lines). After that region the decay possesses a different decay parameter, which is more closely related with the radial boundary conditions than with the turbulence itself.

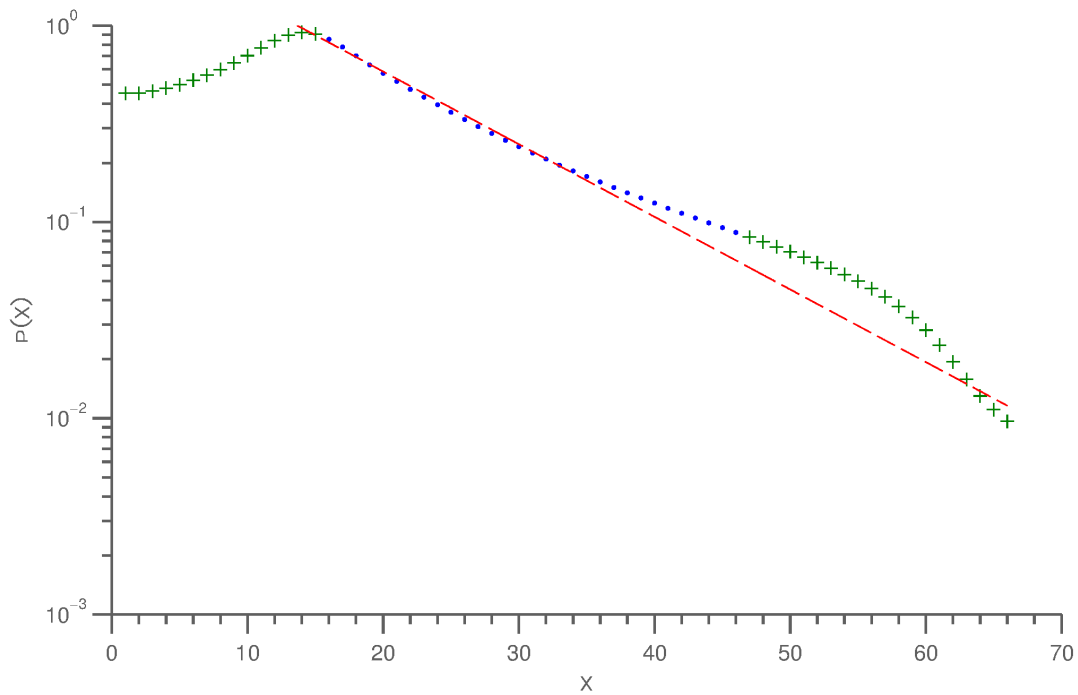


Figure 4.5: Fit to the expression (4.1) for the resulting pressure profile toroidally and poloidally averaged. The logarithmic vertical axes allows the visual separation of the characteristic exponential decays right after the source at $x = 15$ and before the wall. The fit results in a $L_p = 1.1$ cm with a SOL width of 4.6 cm. The green crosses indicate values excluded from the fit.

The fit on Fig. 4.5 provides an $L_p = 1.1$ cm, less than a fourth of the whole domain, with a value of the coefficient of determination $R^2 = 0.9937$ $\left(R^2 = 1 - \frac{\sum_i (y_i - f_i)^2}{\sum_i (y_i - \bar{y})^2} \right)$. The starting and end position where chosen so that R^2 would be the maximum and L_p would not deviate too much. With this result, we can look at the value of L_p for a specific toroidal and poloidal region. In order to describe the fit at a 95 % confidence value we include the error bars that characterize this region.

Performing solely a poloidal average, we look at $L_p(z)$ in Fig. 4.6 including the the error bars provided from the fit. A variation of less than 5 % through the whole torus is obtained. As expected the values of $z = 0$ and $z = 2\pi$ are disconnected by the presence of the limiter at this region.

Finally, we look at the variation of $L_p(y)$ with the poloidal angle in Fig. 4.7. The situation is quite

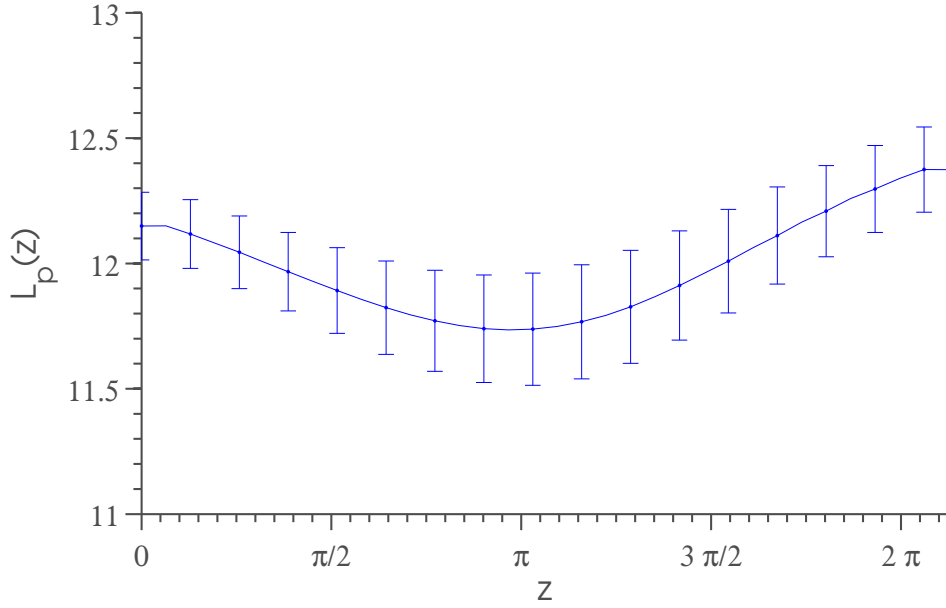


Figure 4.6: Toroidal variation of L_p from the fit to non-linear simulations. The vertical axes shows L_p in GBS units, where 1 GBS unit = 0.91 mm.

different, with a periodic domain that provides a variation of over 50 %. As we saw in the previous chapter, one of the addressed instabilities (BM) has a different character at the LFS (center of the plot) and at the HFS (starting and ending region of the plot) while DW remain with the same characteristics through y .

There is an asymmetry present in the figure for $L_p(y)$, which is thought to be caused by the presence of finite k_x within the non-linear simulations (recall that in the linear code we assumed $k_y \gg k_x$). At the LFS the interchange instability is dominant, arising mainly from curvature terms. Linearizing the curvature operator, retaining k_x terms and Taylor expanding the sin and cos terms to second order we obtain for $\hat{s} = 0$

$$C \sim -\frac{k_y}{2} \left(\theta - \frac{k_x}{k_y} \right)^2 + \frac{2k_y^2 + k_x^2}{2k_y}. \quad (4.2)$$

This expression contains the term k_x/k_y that can cause the observed asymmetry (relevant at values of θ near 0) and shows a shift to the right as seen on Fig. 4.7.

The SOL width in the non-linear simulations is of 4.6 cm (50 GBS units) which is 3 cm larger than ISTTOK but, based on simulations with a SOL realistic width of 1.5 cm, L_p scales with the SOL width within the non-linear simulations. These simulations with smaller domain require a much greater value of the diffusion coefficient, which alters significantly the results of the non-linear tests.

We can estimate L_p through the gradient removal theory and compare this prediction with the non-linear simulations. First we note that all the non-linear simulations satisfy the inequality $\sqrt{k_y L_p} < 3$, since we obtain (with minor fluctuations) a value of $k_y = 0.2$ and even for the maximum $L_p = 16$ at the LFS one has $\sqrt{k_y L_p} \sim 1.8$ and therefore they belong to the regime where the gradient removal mechanism is responsible for the turbulence saturation.

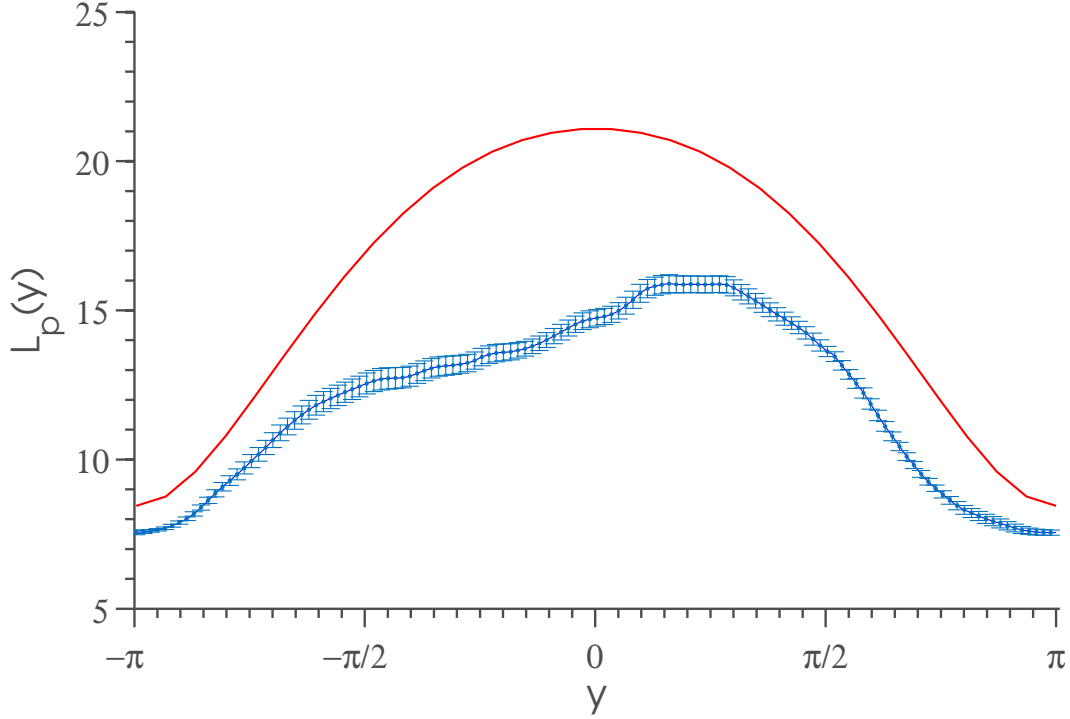


Figure 4.7: Poloidal variation of L_p from the fit to non-linear simulations (blue) and from the gradient removal hypothesis (red). The vertical axes shows L_p in GBS units, where 1 GBS unit = 0.91 mm.

In Fig. 4.7 we show the resulting poloidal variation of L_p provided by the gradient removal hypothesis (together with the linear code). We see a periodic and symmetric figure, with the same behavior as in the non-linear simulations (increasing at the LFS and decreasing at the HFS). As we have seen, the ballooning instability could be the one responsible for this variation at the LFS due to its different character along y .

The quantitative value of L_p is also relevant for the analysis and it shows good agreement with a minimum of $L_p = 7$ instead of 7.5 and a maximum of $L_p = 21$ instead of 16. The disagreement at the LFS has two main reasons: the quality of the fit to the non-linear simulations, where we dropped the points near to the wall therefore decreasing L_p ; the boundary conditions applied on the linear code, where a mix of Neumann and Dirichlet conditions were implemented. To assess this, we looked at the value of $\nu_s = \left| \frac{1}{\phi} \frac{\partial \phi}{\partial z} \right|_{\text{wall}}$ on the non-linear simulations obtaining $\nu_s \sim 400$, which is the value used within the linear code. If solely Dirichlet or Neumann boundary conditions were present we would expect a value of $\nu_s = 0$ or $\nu_s \rightarrow \infty$ respectively. The fact that ν_s is finite and does not approach infinity shows that the boundary conditions on the linear code should include the sheath conditions implemented in GBS when a poloidal limiter is present.

It is also useful to look at the adimensionalized parameter η_e since it allows the comparison to the experimental results where the actual SOL width scale is not relevant since $\eta = \frac{L_n}{L_T}$ and the common factors of dimensions and units cancel out. In Fig. 4.8 we show the resulting η_e value through a radial fit of the density and temperature toroidally and poloidally averaged profiles to an exponential behavior like before. Dividing L_n by L_T a value of $\eta_e = 0.80$ is obtained. This value is the one used to compare the experimental results with the non-linear simulations. The value of η_i could also be used, but experimentally only T_e is known with precision at the SOL and through the introduction of a finite τ in

GBS we obtain $\eta_i \simeq \eta_e$.

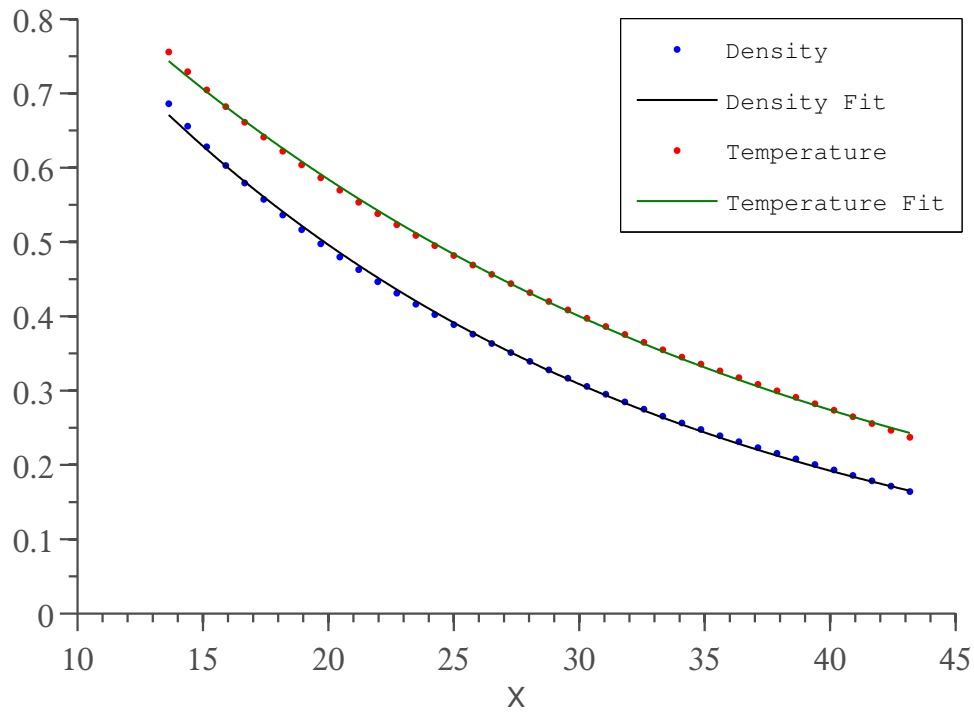


Figure 4.8: Poloidally and toroidally averaged density and electron temperature profiles fitted to an exponential behavior. The obtained value of $\eta_e = \frac{L_n}{L_{T_e}}$ is $\eta_e = 0.80$.

Looking at the poloidal variation of η_e in Fig. 4.9 we see the expected periodic behavior but not the same characteristic LFS vs HFS. A value of $\eta_e < 1$ shows that $L_T > L_n$ and at the LFS this difference becomes steeper.

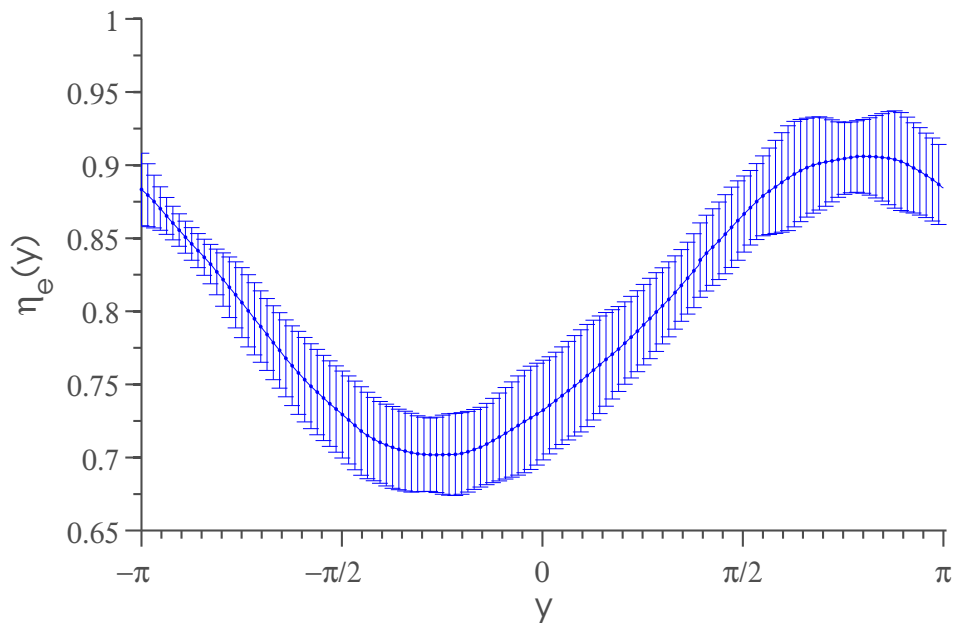


Figure 4.9: Poloidal variation of η_e from the fit to non-linear simulations.

4.3 Non-linear Analysis

We have seen through linear studies that the predicted instabilities are BM at the LFS and DW at the HFS. This has been confirmed by the gradient removal hypothesis, which has already been shown that provides similar typical gradient length for various GBS quantities. The confirmation of the predicted instabilities through non-linear simulations not only validates the aforementioned hypothesis (leading to a conclusive simple model) but supports our methodology to identify non-linear turbulent regimes, even for more complicated SOL configurations.

In Fig. 4.10 we look at a scatter plot between potential and density fluctuations (normalized by their respective standard deviation) for the cold ion simulation (top) and for the simulation with no BM coupling (bottom), which shows a higher correlated plot at the HFS than at the LFS. As we have seen in Chap. 3, it is an evidence of the DW character of turbulence at the HFS, where the interchange drive is not as relevant. This points to the same results that we have seen through the linear solver (Fig. 3.4). It is interesting to note the differences with the simulations with no interchange drive (also shown in Fig. 4.10). As we have seen before in Fig. 4.4, when the ballooning character is lost, the typical gradient lengths decrease here and increase at the HFS.

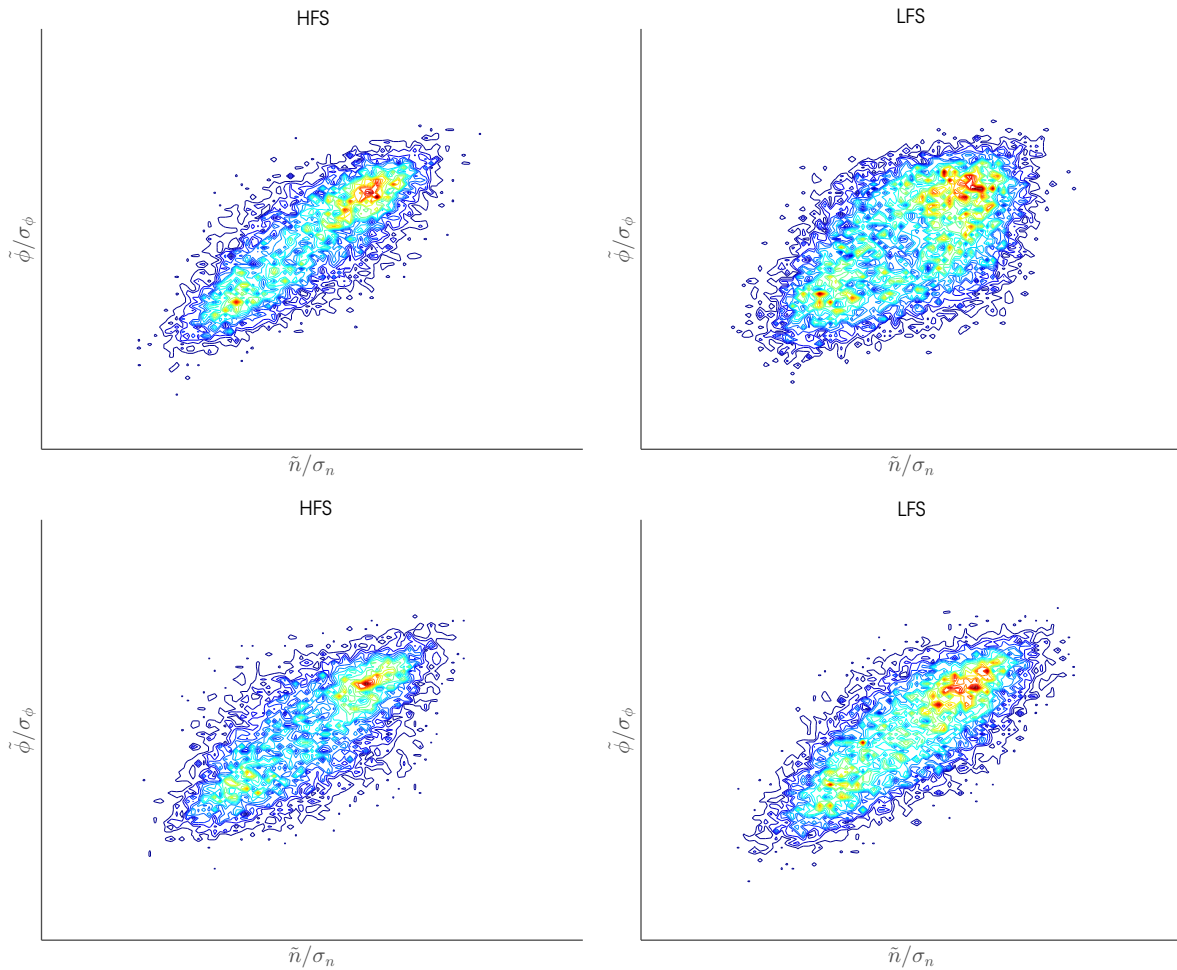


Figure 4.10: Cross-coherence test at the HFS and LFS respectively (electric potential vs density). At the top is an ISTTOK-like simulation and at the bottom the BM coupling terms are turned off.

Moving to the phase-shift test, we can see in Fig. 4.11 that the test shows a negligible phase-shift of ϕ with n at the HFS indicating a non-ballooning character at this location but it remains inconclusive at the LFS. Despite the greatest variation of the phase-shift that can point to a finite value, there is no indication that $\pi/2$ is a preferred value.

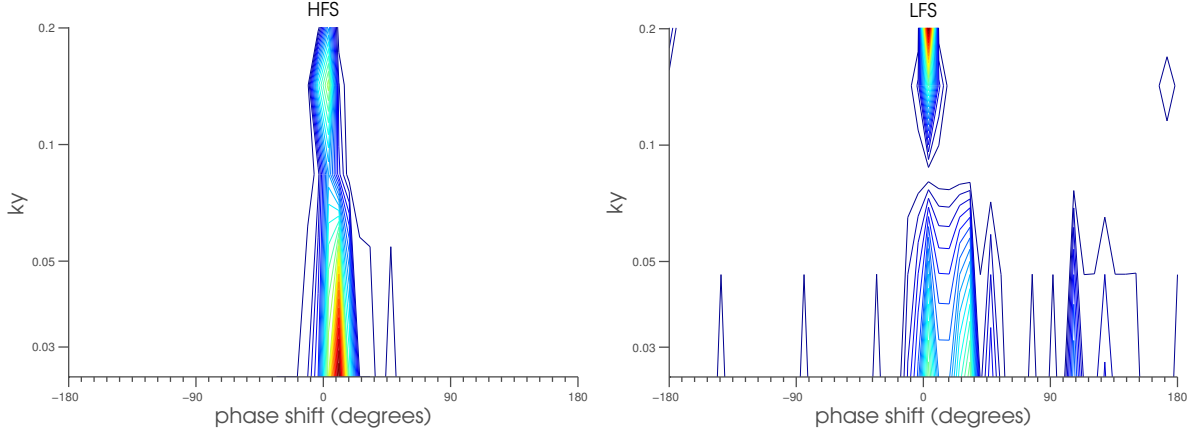


Figure 4.11: Phase-shift between ϕ and N_e at the HFS and LFS respectively.

Lastly, the power-spectrum test is shown in Fig. 4.12. The non-dependence of the $\text{FFT}(V_f)$ (and also for the $\text{FFT}(N_e)$) with the frequency is clearly observed for $f < 80$ KHz and the power indices for LFS are greater than at the HFS. In ISTTOK [1] the non-dependence for low frequencies has been observed as well as a small difference in the power indices (see Fig. 3.5). The most interesting fact is the major difference in the slope of the power spectrum in the no DW coupling case (Fig. 4.13). It doubles its value, which becomes close to the experimental value of -2.

We have seen through the power-spectrum that different locations provide different slopes, which does not coincide with the experimental observations. This can be due to the different instabilities present at the LFS and HFS that may have different impact on the simulations (and therefore provide different slopes) but it requires further study.

In order to verify which are characteristic frequencies present we first note that the characteristic time used as a normalization to model the SOL parameters in the GBS code is $\frac{c_s}{R} \simeq 95$ kHz. Looking at the value of $\frac{c_s}{2\pi R}$, which can be thought as the characteristic *angular velocity* of the particles around the torus in the SOL, we obtain $\frac{c_s}{2\pi R} \simeq 15$ kHz. Other characteristic frequency is $V_{E \times B} / L_p$ which we represent in Fig. 4.14 as a function of y which reveals itself to poloidally vary between 30 and 90 kHz. As the transition region is harder to find in the power-spectrum figure, we perform the fit at the startup position from 100 kHz (the characteristic frequency and the experimental position of the knee) to the last frequency data (300 kHz).

4.4 Comparison Against Experimental Results

In Fig. 4.15 we provide ISTTOK experimental results at the SOL for electron density, floating potential and electron temperature at the LFS. We can see the exponential character of the profiles on the T_e plot

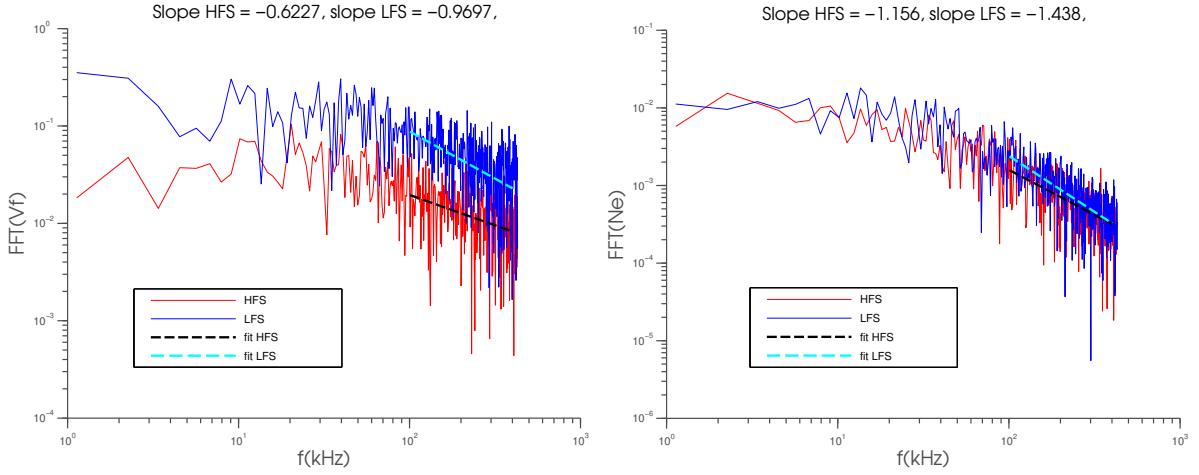


Figure 4.12: Power-spectrum at the HFS and LFS respectively (floating potential V_f and density Ne).

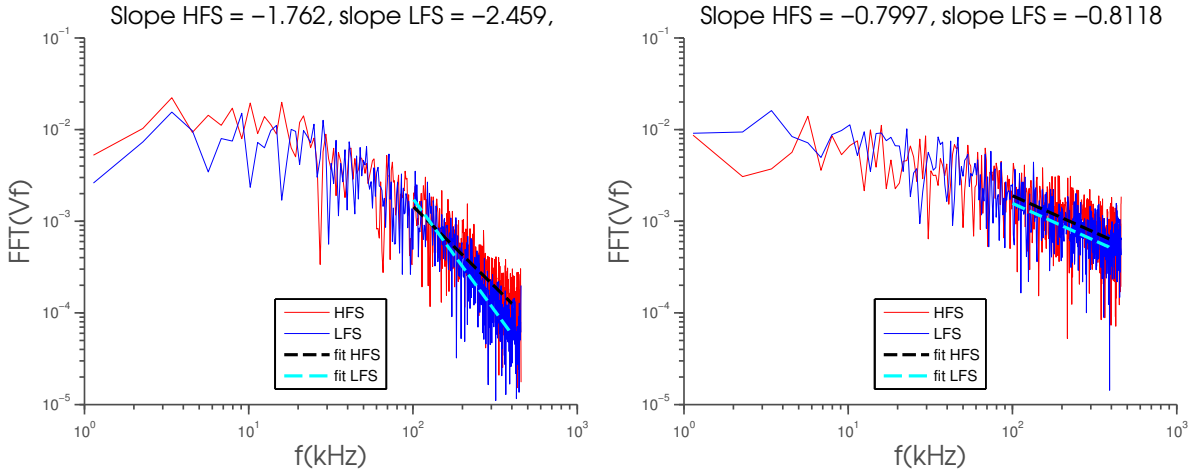


Figure 4.13: Power-spectrum at the HFS and LFS for no DW and interchange coupling respectively for the electric potential.

and for some I_p values on the density plot. With this we can compute L_n, L_{T_e}, η_e and L_p and compare with the linear and non-linear results. For this we use $p = nT$ which leads to

$$\frac{1}{L_p} = \frac{1}{L_n} + \frac{1}{L_T} = \frac{1}{L_n}(1 + \eta). \quad (4.3)$$

From Eqs. (1.11) and (1.10) together with ISTTOK parameters (table 1.1) we get the formula

$$q = \frac{39.27}{I_p} \text{ kA}^{-1}, \quad (4.4)$$

which for $I_p = 4.0$ and $I_p = 5.5$ kA provides $q = 9.82$ and $q = 7.14$. These will be the values used to compare with the simulations with $q = 8$. From Fig. 4.15 we get the average of these quantities for the two values of I_p . The last point closer to the wall was removed, as done with the GBS data in order to perform the same analysis on both results. The estimates are presented in table 4.1 and the fits in Fig. 4.16 and Fig. 4.17.

As before, the adimensionalized parameter that does not take into account the SOL width difference

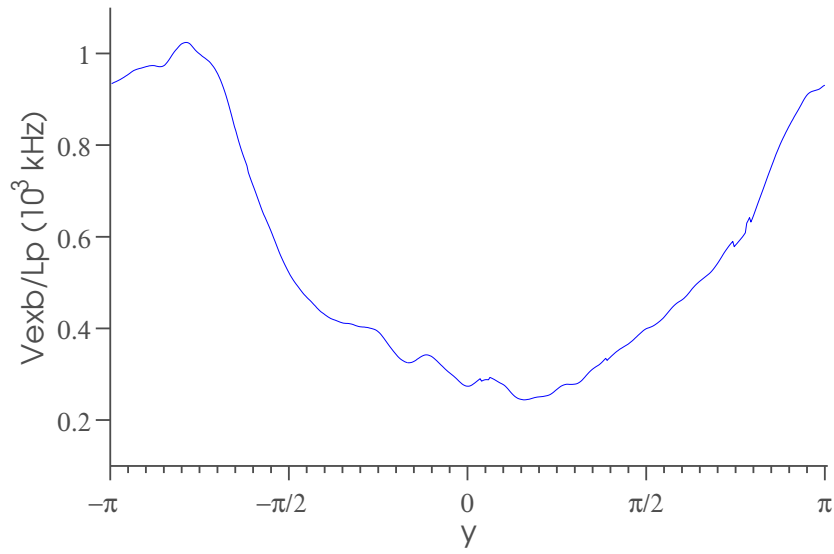


Figure 4.14: $V_{\mathbf{E} \times \mathbf{B}}/L_p$ as a function of γ .

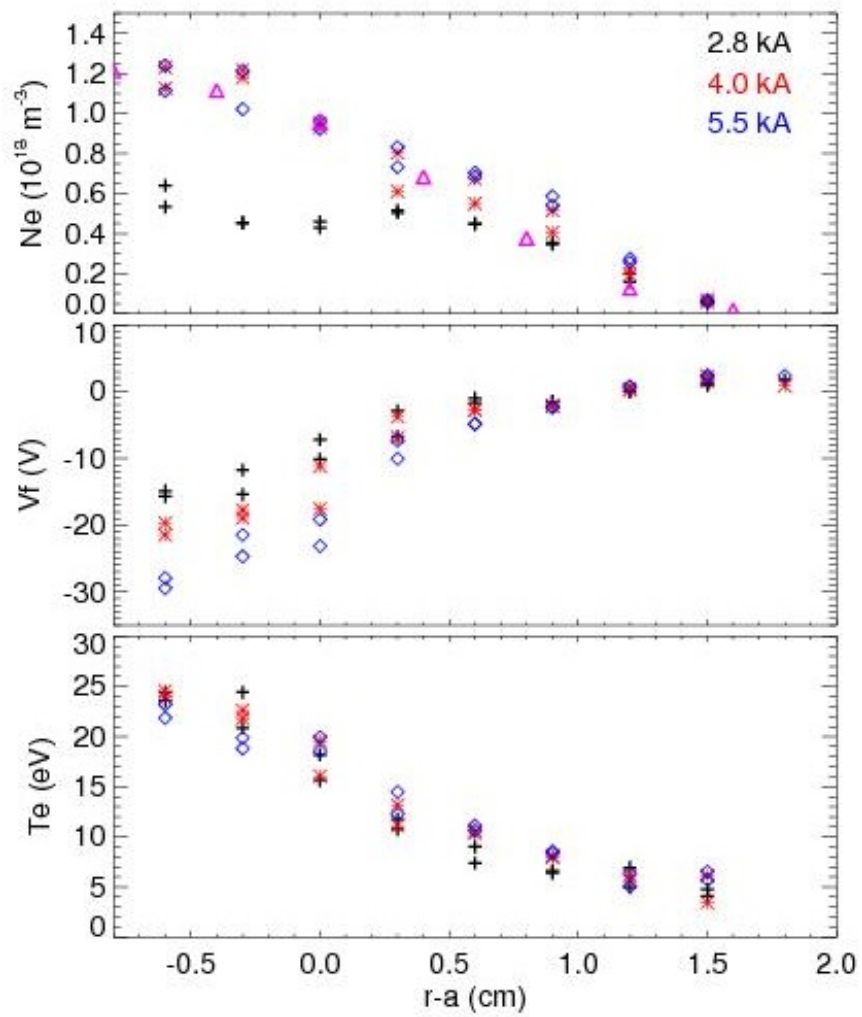


Figure 4.15: I_p scan at ISTTOK with different values of $r - a$ for T_e , V_f and density.

L_n	12.11
L_{T_e}	12.10
η_e	1.001
L_p	6.05

Table 4.1: Experimental results for L_n , L_T , η and L_p for ISTTOK from Fig. 4.15 in GBS units (1 GBS unit = 0.91 mm in SI units).

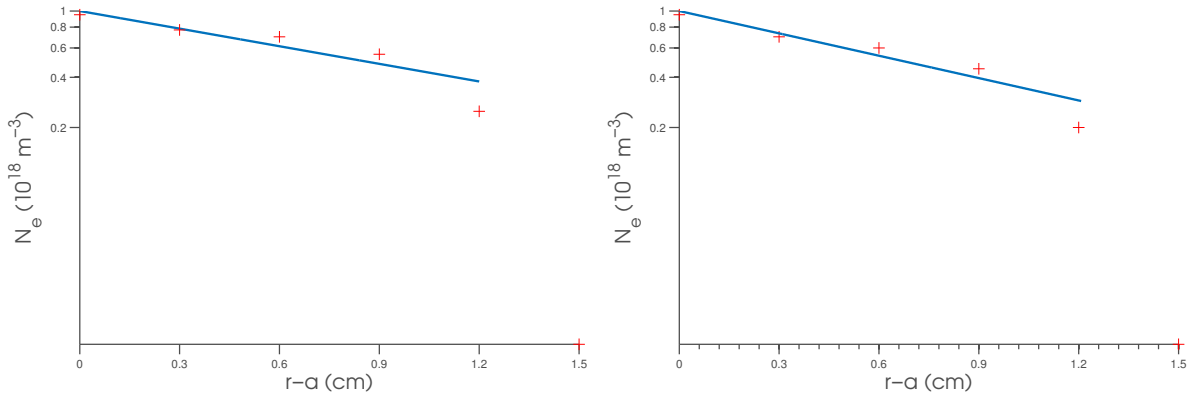


Figure 4.16: Exponential fit to ISTTOK experimental N_e results. The fit to $I_p = 4.0$ kA provides $L_n = 1.232$ cm with an $R^2 = 0.89$ and the fit to $I_p = 5.5$ kA provides $L_n = 0.971$ cm with an $R^2 = 0.941$.

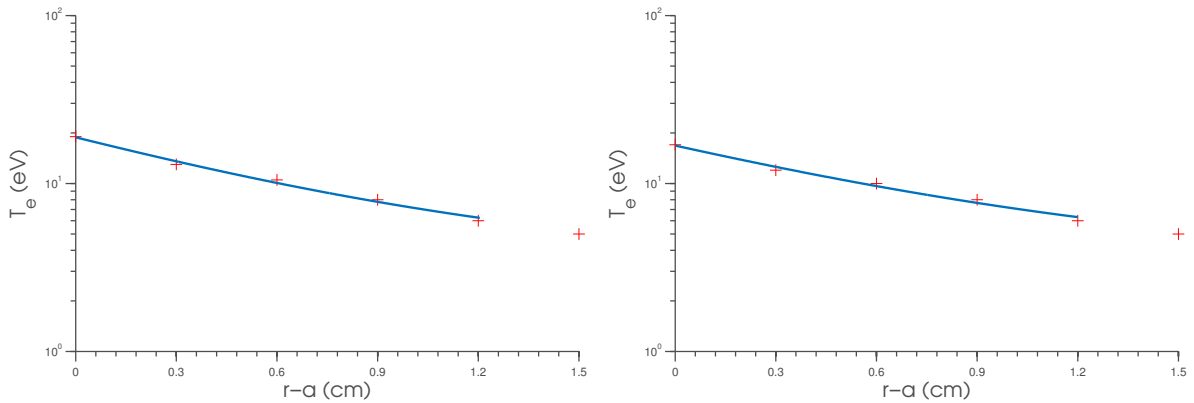


Figure 4.17: Exponential fit to ISTTOK experimental N_e results. The fit to $I_p = 4.0$ kA provides $L_T = 1.033$ cm with an $R^2 = 0.99$ and the fit to $I_p = 5.5$ kA provides $L_T = 1.168$ cm with an $R^2 = 0.98$.

between GBS simulations and experiment is η_e , where this difference is canceled out by the ratio L_n/L_T . From the simulations (Fig. 4.9) we obtain a poloidal variation of η_e from 0.7 to 0.9, with an average value of $\bar{\eta}_e = 0.8$. Since the error bars from the fit provide an error of ± 0.05 , at the LFS $\eta_{e\text{GBS}} = 0.8 \pm 0.05$. The experimental measurements were performed at the LFS, where it was found $\eta_{e\text{exp}} = 1.001$.

The experimental value lies outside the fit confidence interval for η_e . Since GBS simulations are performed with a larger SOL width, there could be some differences in the values of L_n and L_T for a smaller domain. A simulation with the ISTTOK's SOL width value points to an increase of $\eta_{e\text{GBS}}$ but the results are not conclusive due to the destabilization provoked by such a small radial domain, mainly the major turbulence drive to the walls.

Conclusions

One of the main challenges today's fusion program is to accurately predict the SOL dynamics and understand the physics behind it. It is a very rich domain, from the study of the plasma boundary conditions (where the plasma is lost to the divertor or limiter in this region) to the study of turbulence driven transport. SOL physics is what determines the boundary conditions for the plasma in the whole machine, regulating the power exhaust. This is why we need to identify the turbulent regimes present in this region, their main features and their dependence on SOL operational parameters. In this thesis, we focus on the analysis of scrape-off layer dynamics on ISTTOK geometry, which has a single poloidal limiter and a large aspect ratio with a circular cross-section, and study the results provided from linear and non-linear simulations which are then compared to the existing experimental results.

In chapter 2 we have detailedly described the model used, which is based on the drift-reduced Braginskii equations. We also describe ISTTOK's geometry and parameters, together with the numerical implementation of the non-linear code, its boundary and initial conditions.

In chapter 3 we introduce the linear solver, from the linear set of GBS equations to the numerical implementation, together with an estimate of L_p (plasma pressure typical gradient length) through the gradient removal mechanism. The main instabilities included in the model are described and their respective branches. In the final section we describe the different diagnostics used in the non-linear simulation results.

In chapter 4 the simulation results are described and analyzed. GBS simulations allowed a discussion of the different modes present in the LFS and HFS through the non-linear tests described in section ???. It was observed a greater correlation between the electric potential and density at the HFS compared with the LFS, assessing the drift-wave character of the turbulence there. Performing the power-spectrum of the floating potential, we have identified different slopes at the HFS and LFS, which does not match the experimental results. This may be due to the different impact of the instabilities at those locations. The gradient removal hypothesis provided an L_p with the same behavior as seen on the non-linear simulations. It also pointed that at the LFS the inertial ballooning mode instability is responsible for the greatest linear growth rate, while at the HFS it is the inertial drift wave instability. Through a scan in \hat{s} we see that the value of magnetic shear is negligible when it comes to assert the instabilities present on ISTTOK. The introduction of ionic temperature (through the introduction of a finite $\tau = \frac{T_i}{T_e}$) results on a

small broadening of the poloidal range of the InDW branch. Looking at the experimental results, we have estimated a value of $L_p = 4.94$ at the LFS (in GBS units) while the non-linear show a value of $L_p = 14$. This was mainly due to the SOL width used in GBS simulations of $L_x = 50$, while at ISTTOK $L_x = 16$. Due to this fact, we look to the adimensionalized parameter η_e , where $\eta_{e_{GBS}} = 0.8$ and $\eta_{e_{ISTTOK}} = 1.0$, a relative error of 20 %.

Future extensions of this work include the study of non-linear simulations with different values of resistivity and magnetic shear in order to analyze the different instability branch (RBM) shown within the linear code and perform a study on the presence of plasma blobs in ISTTOK's SOL. Furthermore, in order to completely model ISTTOK's geometry, the parallel diffusion routine has to be ported to a poloidally symmetric configuration and the boundary conditions should include a real limiter with 12 graphite plates instead of a continuous poloidal plate. In order to address the analysis of future reactor relevant configurations, GBS simulations can be performed in a more complicated magnetic geometry (such as X-point geometry). Under study with this code is the simulation of plasma blobs [28], aspect ratio effects [54] and intrinsic toroidal rotation in the SOL [55] which is relevant not only for ISTTOK (see for example [56]) but also for future tokamaks such as International Thermonuclear Experimental Reactor (ITER).

Bibliography

- [1] C. Silva, H. Figueiredo, P. Duarte, and H. Fernandes. Characterization of the poloidal asymmetries in the ISTTOK edge plasma. *Plasma Physics and Controlled Fusion*, **53**(8), 2011.
- [2] D. Simmons. Hard facts, an energy primer. Technical report, Institute for Energy Research, 2012.
- [3] Max Planck Institute for Plasma Physics. Schematic Representation of a Tokamak. <http://www.ideen2020.de/en/51/>, 2012. [Online; accessed 8-September-2014].
- [4] P.C. Strangeby. *The plasma boundary of magnetic fusion devices*. Institute of Physics Pub, Bristol Philadelphia, 2000.
- [5] IPFN (Instituto de Plasmas e Fusão Nuclear). ISTTOK figures and general information. <http://www.ipfn.ist.utl.pt/{ISTTOK}/>, 2014. [Online; accessed 8-September-2014].
- [6] A. Zeiler, J. F. Drake, and B. Rogers. Nonlinear reduced Braginskii equations with ion thermal dynamics in toroidal plasma. *Physics of Plasmas*, **2134**(4), 1997.
- [7] The World Bank. Fossil fuel energy consumption (% of total). Technical report, IEA Statistics, 2013.
- [8] J. Skea, P. Ekins, and M. Winskel. *Making the Transition to a Secure Low-Carbon Energy System*. Routledge, 2010.
- [9] David W. Dorn. Predictions of spontaneous fission half-lives for heavy nuclei. *Physical Review*, **121**(6), Mar 1961.
- [10] A. A. Harms, K. F. Schoepf, G. H. Miley, and D. R. Kingdon. *Principles of Fusion Energy: An Introduction to Fusion Energy for Students of Science and Engineering*. World Scientific Publishing, 2000.
- [11] J. Freidberg. *Plasma physics and fusion energy*. Cambridge University Press, Cambridge, 2007.
- [12] E.J. Doyle et al. Chapter 2: Plasma confinement and transport. *Nuclear Fusion*, **47**(6), 2007.
- [13] M. Kikuchi, K. Lackner, and M. Q. Tran. *Fusion Physics*. International Atomic Energy Agency, 2012.
- [14] D. R. Nicholson. *Introduction to Plasma Theory*. John Wiley & Sons, New York, 1983.

- [15] EFDA (European Fusion Development Agreement). Lawson's three criteria. <https://www.efda.org/2013/02/triple-product/>, 2013. [Online; accessed 8-September-2014].
- [16] J. Wesson. *Tokamaks; 4th ed.* International series of monographs on physics. Oxford Univ. Press, Oxford, 2011.
- [17] R.E.H. Clark. *Nuclear fusion research understanding plasma-surface interactions.* Springer, Berlin New York, 2005.
- [18] I. Langmuir and C.G. Suits. *Collected works: with contributions in memoriam, including a complete bibliography of his works.* Number v. 4 in *Collected Works: With Contributions in Memoriam, Including a Complete Bibliography of His Works.* Published with the editorial assistance of the General Electric Co. by Pergamon Press, 1961.
- [19] J. A. C. Cabral, C. A. F. Varandas, A. Malaquias, A. Praxedes, M. P. Alonso, P. Belo, R. Canário, H. Fernandes, J. Ferreira, C. J. Freitas, R. Gomes, J. Pires, C. Silva, A. Soares, J. Sousa, and P. H. M. Vaessen. Analysis of the ISTTOK plasma density profile evolution in sawtooth discharges by heavy-ion beam probing. *Plasma Physics and Controlled Fusion*, **38**(51), September 1995.
- [20] H. Fernandes, C. Silva, R. B. Gomes, A. Neto, P. Duarte, G. Van Oost, M. Gryaznevich, and A. Malaquias. The international joint experiment ISTTOK. *Plasma Physics Reports*, **35**(10), 2009.
- [21] C. Silva, H. Fernandes, C. A. F. Varandas, D. Alves, P. Balan, B. B. Carvalho, I. Carvalho, P. Carvalho, P. A. Carvalho, R. Coelho, J. B. Correia, A. Duarte, P. Duarte, J. Ferreira, H. Figueiredo, J. Figueiredo, J. Fortunato, R. Galvao, R. Gomes, B. Gonçalves, C. Hidalgo, C. Ionita, O. Lielausis, V. Livramento, T. Lunt, A. Klyukin, I. Nedzelskij, A. Neto, T. Pereira, E. Platacis, V. Plyusnin, R. Schrittwieser, A. Sharakovski, I. Tale, and D. Valcárcel. Overview of recent ISTTOK results. *AIP Conference Proceedings*, **996**(1), 2008.
- [22] H. Figueiredo, C. Silva, B. Gonçalves, P. Duarte, and H. Fernandes. Plasma flow and transport on the tokamak ISTTOK boundary plasma. *Journal of Nuclear Materials*, **415**(1, Supplement), 2011. Proceedings of the 19th International Conference on Plasma-Surface Interactions in Controlled Fusion.
- [23] R.B. Gomes, C. Silva, H. Fernandes, P. Duarte, I. Nedzelskiy, O. Lielausis, A. Klyukin, and E. Platacis. ISTTOK tokamak plasmas influence on a liquid gallium jet dynamic behavior. *Journal of Nuclear Materials*, **415**(1, Supplement), 2011. Proceedings of the 19th International Conference on Plasma-Surface Interactions in Controlled Fusion.
- [24] P. Ricci, F. D. Halpern, S. Jolliet, J. Loizu, A. Masetto, A. Fasoli, I. Furno, and C. Theiler. Simulation of plasma turbulence in scrape-off layer conditions: the GBS code, simulation results and code validation. *Plasma Physics and Controlled Fusion*, **52**(124047), 2012.
- [25] P. Ricci, B. N. Rogers, and S. Brunner. High- and low-confinement modes in simple magnetized toroidal plasmas. *Physical Review Letters*, **100**(225002), 2008.

- [26] P. Ricci, C. Theiler, A. Fasoli, I. Furno, B. Labit, S. H. Müller, M. Podestà, and F. M. Poli. Langmuir probe-based observables for plasma-turbulence code validation and application to the TORPEX basic plasma physics experiments. *Physics of Plasmas*, **16**(5), 2009.
- [27] P. Ricci, C. Theiler, A. Fasoli, I. Furno, K. Gustafson, D. Iraj, and J. Loizu. Methodology for turbulence code validation: Quantification of simulation-experiment agreement and application to the TORPEX experiment. *Physics of Plasmas*, **18**(3), 2011.
- [28] F. D. Halpern, A. Cardellini, P. Ricci, S. Jolliet, J. Loizu, and A. Masetto. Three-dimensional simulations of blob dynamics in a simple magnetized torus. *Physics of Plasmas*, **21**(2), 2014.
- [29] D. A. D’Ippolito, J. R. Myra, and S. J. Zweben. Convective transport by intermittent blob-filaments: Comparison of theory and experiment. *Physics of Plasmas*, **18**(060501), 2011.
- [30] J. R. Angus, M. V. Umansky, and S. I. Krasheninnikov. Effect of drift waves on plasma blob dynamics. *Physical Review Letters*, **108**(21), May 2012.
- [31] G. Q. Yu, S. I. Krasheninnikov, and P. N. Guzdar. Two-dimensional modelling of blob dynamics in tokamak edge plasmas. *Physics of Plasmas*, **13**(4), 2006.
- [32] P. Ricci and B. N. Rogers. Plasma turbulence in the scrape-off layer of tokamak devices. *Physics of Plasmas*, **20**(010702), November 2013.
- [33] S. I. Braginskii. Transport processes in a plasma. *Reviews of Plasma Physics*, **1**(6), 1965.
- [34] R. Fitzpatrick. *Plasma Physics*. University of Texas, 2012.
- [35] A. Masetto. *Turbulent Regimes in the Tokamak Scrape-off Layer*. PhD thesis, EPFL, Lausanne, Switzerland, 2014.
- [36] X. Lapillonne, S. Brunner, T. Dannert, S. Jolliet, A. Marinoni, L. Villard, T. Goerler, F. Jenko, and F. Merz. Clarifications to the limitations of the s-alpha equilibrium model for gyrokinetic computations of turbulence. *Physics of Plasmas*, **16**(3), 2009.
- [37] A. Arakawa. Computational design for long-term numerical integration of the equations of fluid motion. two-dimensional incompressible flow. *Journal of Computational Physics*, **1**, 1966.
- [38] F. D. Halpern, J. Loizu, P. Ricci and S. Jolliet. Boundary conditions for plasma fluid models at the magnetic presheath entrance. *Physics of Plasmas*, **19**(122307), 2012.
- [39] A. Masetto, F. D. Halpern, S. Jolliet, J. Loizu, and P. Ricci. Turbulent regimes in the tokamak scrape-off layer. *Physics of Plasmas*, **20**(9), 2013.
- [40] A. J. Webster. Magnetohydrodynamic tokamak plasma edge stability. *Nuclear Fusion*, **52**(11), 2012.
- [41] J. R. Myra, D. A. D’Ippolito, X. Q. Xu, and R. H. Cohen. Resistive modes in the edge and scrape-off layer of diverted tokamaks. *Physics of Plasmas*, **7**(11), 2000.

- [42] A. Zeiler, D. Biskamp, J. F. Drake, and P. N. Guzdar. Three-dimensional fluid simulations of tokamak edge turbulence. *Physics of Plasmas*, **3**(8), 1996.
- [43] J. F. Drake, A. Zeiler, and D. Biskamp. Nonlinear self-sustained drift-wave turbulence. *Physical Review Letters*, **75**(23), Dec 1995.
- [44] B. LaBombard, J. W. Hughes, N. Smick, A. Graf, K. Marr, R. McDermott, M. Reinke, M. Greenwald, B. Lipschultz, J. L. Terry, D. G. Whyte, S. J. Zweben, and Alcator C-Mod Team. Critical gradients and plasma flows in the edge plasma of Alcator C-Mod. *Physics of Plasmas*, **15**(5), 2008.
- [45] B. N. Rogers and W. Dorland. Noncurvature-driven modes in a transport barrier. *Physics of Plasmas*, **12**(6), 2005.
- [46] B. Scott. Three-dimensional computation of drift Alfvén turbulence. *Plasma Physics and Controlled Fusion*, **39**(10), 1997.
- [47] J. R. Myra, D. A. Russell and D. A. D'Ippolito. Saturation mechanisms for edge turbulence. *Physics of Plasmas*, **16**(12), 2009.
- [48] B. D. Scott. Drift wave versus interchange turbulence in tokamak geometry: Linear versus nonlinear mode structure. *Physics of Plasmas*, **12**(62314), 2005.
- [49] J. F. Drake, A. Zeiler, and D. Biskamp. Nonlinear self-sustained drift-wave turbulence. *Physical Review Letters*, **75**(4), 1995.
- [50] P. Ricci and B. N. Rogers. Three-dimensional fluid simulations of a simple magnetized toroidal plasma. *Physics of Plasmas*, **16**(9), 2009.
- [51] F.D. Halpern, P. Ricci, S. Jolliet, J. Loizu, and A. Masetto. Theory of the scrape-off layer width in inner-wall limited tokamak plasmas. *Nuclear Fusion*, **54**(4), 2014.
- [52] D. E. Muller. A method for solving algebraic equations using an automatic computer. *Mathematical Tables and Other Aids to Computation*, **10**, 1956.
- [53] B. A. Carreras, R. Balbin, B. van Milligen, M. A. Pedrosa, I. Garcia-Cortes, E. Sanchez, C. Hidalgo, J. Bleuel, M. Endler, H. Thomsen, A. Chankin, S. Davies, K. Erents, and G. F. Matthews. Characterization of the frequency ranges of the plasma edge fluctuation spectra. *Physics of Plasmas*, **6**(12), 1999.
- [54] S. Jolliet, F. D. Halpern, J. Loizu, A. Masetto, and P. Ricci. Aspect ratio effects on limited scrape-off layer plasma turbulence. *Physics of Plasmas*, **21**(2), 2014.
- [55] J. Loizu, P. Ricci, F. D. Halpern, S. Jolliet, and A. Masetto. Intrinsic toroidal rotation in the scrape-off layer of tokamaks. *Physics of Plasmas*, **21**(6), 2014.
- [56] C. Silva, P. Duarte, H. Fernandes, H. Figueiredo, I. Nedzelskij, C. Hidalgo, and M. A. Pedrosa. Characterization of geodesic acoustic modes in the ISTTOK edge plasma. *Plasma Physics and Controlled Fusion*, **51**(8), 2009.

- [57] S. Tsai, F. W. Perkins, and T. H. Stix. Thermal conductivity and low frequency waves in collisional plasmas. *Physics of Fluids (1958-1988)*, **13**(8), 1970.
- [58] S. Chapman and T. G. Cowling. *The Mathematical Theory of Non-Uniform Gases*. Cambridge University Press, 1953.

Derivation of the Braginskii equations

The GBS code evolves the drift-reduced Braginskii equations [6]. The drift-reduced approximation has been used by several authors (e. g. [57]). We shall derive the Braginskii equations [33] here and the drift-reduced model in Chap. 2.

Starting with a kinetic description, namely the microscopic distribution function \bar{f}_s for each one of the plasma species s , we define the microscopic density and current as (with e_s the charge of the species s)

$$\rho = \sum_s e_s \int \bar{f}_s(\mathbf{r}, \mathbf{v}, t) d^3v, \quad (\text{A.1})$$

$$\mathbf{j} = \sum_s e_s \int \mathbf{v} \bar{f}_s(\mathbf{r}, \mathbf{v}, t) d^3v, \quad (\text{A.2})$$

with the normalization $\int \bar{f}_s(\mathbf{r}, \mathbf{v}, t) d^3v = n_s(\mathbf{r}, t)$, where n_s is the density of the species s . Through phase-space conservation we conclude [33]

$$\frac{\partial \bar{f}}{\partial t} + \mathbf{v} \cdot \nabla_{\mathbf{r}} \bar{f}_s + \mathbf{a}_s \cdot \nabla_{\mathbf{v}} \bar{f}_s = 0. \quad (\text{A.3})$$

The acceleration of the species s is due to the electric and magnetic field coupling provided by the Lorentz force $\mathbf{a}_s = \frac{e_s}{m} (\mathbf{E} + \mathbf{v} \times \mathbf{B})$. Further applying an ensemble average (integrating over the phase space of the system) with the notation $\langle \rangle$, we define the collision operator $C_s(f)$ and the (ensemble averaged) distribution function f_s as

$$\langle a_s \cdot \nabla_{\mathbf{v}} \bar{f}_s \rangle \equiv \langle \mathbf{a}_s \rangle \cdot \nabla_{\mathbf{v}} f_s - C_s(f), \quad (\text{A.4})$$

$$\langle \bar{f}_s \rangle \equiv f_s,$$

arriving at the Boltzmann's equation

$$\frac{\partial f_s}{\partial t} + \mathbf{v} \cdot \nabla f_s + \langle \mathbf{a}_s \rangle \cdot \nabla_{\mathbf{v}} f_s = C_s(f). \quad (\text{A.5})$$

This ‘‘averaged’’ description is the basis for the fluid model. This description is appealing, since one can understand the significance of each fluid quantities such as density and temperature with comparison to the more abstract definition of distribution functions. In the fluid model, one defines the moments of the distribution function - density, fluid velocity, stress tensor and energy flux density respectively as

$$n_s(\mathbf{r}, t) \equiv \int f_s(\mathbf{r}, \mathbf{v}, t) d^3v, \quad (\text{A.6})$$

$$n_s \mathbf{V}_s(\mathbf{r}, t) \equiv \int \mathbf{v} f_s(\mathbf{r}, \mathbf{v}, t) d^3v, \quad (\text{A.7})$$

$$P_{s_{ij}}(\mathbf{r}, t) \equiv \int m_s v_i v_j f_s(\mathbf{r}, \mathbf{v}, t) d^3v, \quad (\text{A.8})$$

$$\mathbf{Q}_s(\mathbf{r}, t) \equiv \int \frac{m_s}{s} v^2 \mathbf{v} f_s(\mathbf{r}, \mathbf{v}, t) d^3v. \quad (\text{A.9})$$

Further introducing the relative velocity $\mathbf{w}_s \equiv \mathbf{v} - \mathbf{V}_s$ in order to position ourselves in the rest-frame of the system, we can define the press tensor $\mathbf{p}_s(\mathbf{r}, t) = \int m_s \mathbf{w}_s \mathbf{w}_s f_s(\mathbf{r}, \mathbf{v}, t) d^3v$ and the heat flux density $\mathbf{q}_s(\mathbf{r}, t) = \int \frac{m_s w_s^2}{2} \mathbf{w}_s f_s(\mathbf{r}, \mathbf{v}, t) d^3v$, obtaining the (scalar) pressure $p_s \equiv \frac{\text{Tr}(\mathbf{p}_s)}{3}$ and, by direct substitution the relations

$$\mathbf{P}_s = \mathbf{p}_s + m_s n_s \mathbf{V}_s \mathbf{V}_s, \quad (\text{A.10})$$

$$\mathbf{Q}_s = \mathbf{q}_s + \mathbf{p}_s \cdot \mathbf{V}_s + \frac{3}{2} p_s \mathbf{V}_s + \frac{m_s V_s^2}{2} n_s \mathbf{V}_s. \quad (\text{A.11})$$

Considering only binary collisions and the fact that in a strongly magnetized plasma the Debye length is much smaller than the typical length of system, we can consider the collision operator $C_s(f)$ as bilinear in the distribution functions of the two colliding species [34]

$$C_s(f) = \sum_{s'} C_{ss'}(f_s, f_{s'}). \quad (\text{A.12})$$

Through the collision operator one can also define its moments and obtain kth order moments of the Boltzmann’s equation, arriving to the fluid equations (with the Einstein summation convention)

$$\frac{dn_s}{dt} + n_s \nabla \cdot \mathbf{V}_s = 0, \quad (\text{A.13})$$

$$m_s n_s \frac{d\mathbf{V}_s}{dt} + \nabla p_s + \nabla \cdot \boldsymbol{\pi}_s - e_s n_s \left(\mathbf{E} + \frac{\mathbf{V}_s}{c} \times \mathbf{B} \right) = \mathbf{R}_s, \quad (\text{A.14})$$

$$\frac{3}{2} \frac{dp_s}{dt} + p_s \nabla \cdot \mathbf{V}_s + \pi_{s_{ij}} \nabla_i V_{s_j} + \nabla \cdot \mathbf{q}_s = Q_s, \quad (\text{A.15})$$

with the definitions

$$\mathbf{p}_s \equiv p_s \mathbf{I} + \boldsymbol{\pi}_s, \quad \frac{d}{dt} \equiv \frac{\partial}{\partial t} + \mathbf{V}_s \cdot \nabla, \quad (\text{A.16})$$

$$\mathbf{R}_s \equiv \sum_{s'} \int \mathbf{v} m_s C_{ss'} d^3v, \quad Q_s \equiv \sum_{s'} \int \frac{m_s w_s^2}{2} C_{ss'} d^3v. \quad (\text{A.17})$$

After all this manipulation, the well-known closure problem still persists. There is no amount of rearrangement that can provide a solution to this defect. In order to arrive to the Braginskii equations we apply an asymptotic closure scheme, namely the Chapman-Enskog theory of a neutral gas dominated by collisions [58]. Here, the small exploited parameter that provides the estimation of the error involved in the closure is the ratio of the mean-free-path between collisions λ to the macroscopic variation length scale L , expanding the distribution function in the small parameter

$$\delta = \frac{\lambda}{L} \ll 1 \quad (\text{A.18})$$

where to zeroth order in δ , f_0 is a Maxwellian

$$f_0(\mathbf{r}, t) = n(\mathbf{r}) \left(\frac{m}{2\pi T(\mathbf{r})} \right)^{3/2} \exp \left(-\frac{m(\mathbf{v} - \mathbf{V})^2}{2T(\mathbf{r})} \right), \quad (\text{A.19})$$

with $p = nT$.

The Chapman-Enskog scheme is appropriate in our description because we are dealing with *collisional* plasmas. If we further assume that the plasma is *magnetized*, we can expand each quantity in terms of the parameter

$$\epsilon = \frac{\rho}{L} \ll 1 \quad (\text{A.20})$$

where ρ is the Larmor radius and L is the macroscopic length-scale.

Muller's Method Algorithm

Muller's method is used as a generalization of the secant method (which uses 2 initial approximations) in order to find the roots of an equation through 3 initial approximations and then joining them with a second degree polynomial. In this work, we use them in order to find the root of $L_p - \frac{R}{c_s} \frac{\gamma}{k_y}$ (derived in section 3.4). The quadratic formula is used to find the next approximation.

Defining $x_n = (L_p)_n$ and the function $P(x_n) = \max(\frac{R}{c_s} \frac{\gamma}{k_y}) - (L_p)_n$ at iteration n , we have the algorithm [52]

$$q \equiv \frac{x_n - x_{n-1}}{x_{n-1} - x_{n-2}}, \quad (\text{B.1})$$

$$A \equiv qP(x_n) - q(1+q)P(x_{n-1}) + q^2P(x_{n-2}), \quad (\text{B.2})$$

$$B \equiv (2q+1)P(x_n) - (1+q)^2P(x_{n-1}) + q^2P(x_{n-2}), \quad (\text{B.3})$$

$$C \equiv (1+q)P(x_n) \quad (\text{B.4})$$

$$x_{n+1} \equiv x_n - \frac{2C(x_n - x_{n-1})}{\max(B^2 \pm \sqrt{B^2 - 4AC})}. \quad (\text{B.5})$$